Design and Development of an Electrochemical Direct Air Capture Process

Qingdian Shu

Propositions

1. The benefits of a high recirculation in each compartment are underestimated in electrochemical carbon capture processes.
   (this thesis)
2. The large-scale deployment of direct air capture technologies requires more than reporting low energy consumption in research.
   (this thesis)
3. Mathematical modelling always confuses people before new insights are gained.
4. The role of planting trees is overrated for the mitigation of climate change.
5. Flying carbon-free is only an advertisement trap.
6. In modern societies, introverts are forced to be extroverted.

Propositions belonging to the thesis, entitled
“Design and development of an electrochemical direct air capture process"

Qingdian Shu

Leeuwarden, 2 June 2023

Design and development of an electrochemical direct air capture process

Qingdian Shu

Thesis committee

Promotor
Prof. Dr H.V.M (Bert) Hamelers
Special Professor, Electrochemical Resource Recovery
Wageningen University & Research

Co-promotors
Dr P. Kuntke
Lecturer, Environmental Technology
Wageningen University & Research

Dr M.Tedesco
Scientific advisor
Wetsus, European centre of excellence for sustainable water technology, Leeuwarden

Other members
Prof. Dr J.H. Bitter, Wageningen University & Research
Prof. Dr D.W.F. Brilman, University of Twente, Enschede
Prof. Dr J. Keller, The University of Queensland, Australia
Dr S.D. Molenaar, Pure Water Group, Sprundel

This research was conducted under the auspices of the Graduate School for Socio-Economic and Natural Sciences of the Environment (SENSE)

Design and development of an electrochemical direct air capture process

Qingdian Shu

Thesis

submitted in fulfilment of the requirements for the degree of doctor
at Wageningen University
by the authority of the Rector Magnificus,
Prof. Dr A.P.J. Mol,
in the presence of the
Thesis Committee appointed by the Academic Board
to be defended in public
on Friday 02 June 2023
at 11 a.m. in De Harmonie, Leeuwarden

Qingdian Shu
Design and development of an electrochemical direct air capture process,
168 pages.

PhD thesis, Wageningen University, Wageningen, the Netherlands (2023)
With references, with summary in English

ISBN 978-94-6447-605-7
DOI https://doi.org/10.18174/588445

To my beloved parents

献给我的爸爸妈妈

Table of Contents

Chapter 1

Introduction

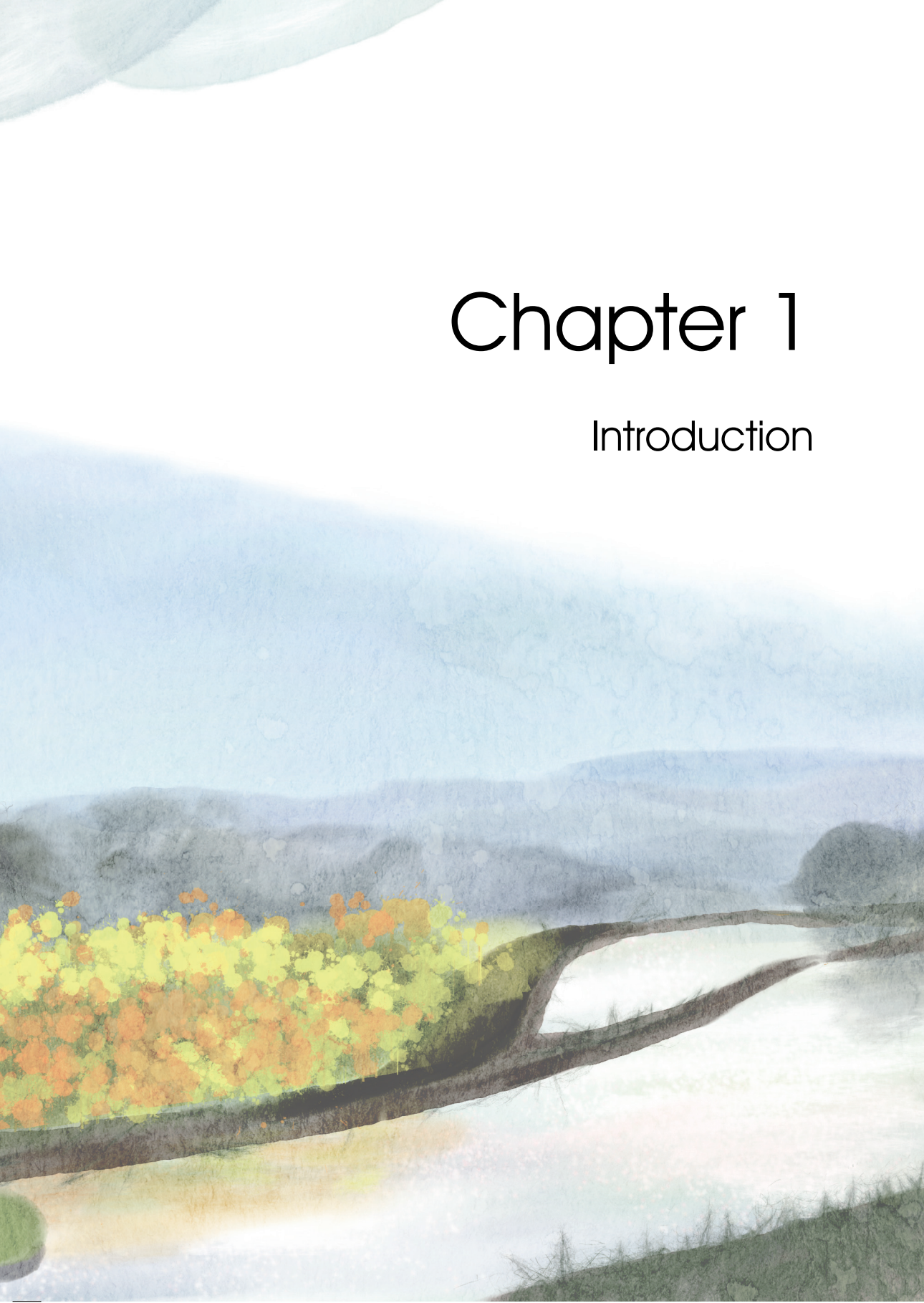

1.1. Urgency for mitigation of climate change

The *Elfstedentocht*, the biggest ice-skating tour in the world, has been a tradition in Friesland, the Netherlands since 1909.[1] The tour takes place when the natural ice along its 200 km course is at least 15 cm thick. Unfortunately, the last time the event occurred was in 1997, and now there is possibly an irreversible loss of this event due to the impact of climate change.

The primary contributor to climate change is the greenhouse gas (GHG) emissions from human activities.[2,3] The GHGs, including carbon dioxide (CO_2), nitrous oxide (N_2O), methane (CH_4), chlorofluorocarbons (CFCs), trap heat in the atmosphere and prevent it from escaping into space, keeping the earth warm. Human activities, such as burning of fossil fuels and deforestation, have increased the concentration of greenhouse gases in the atmosphere.[4,5] Prior to industrial times, the highest atmospheric CO_2 concentration was 300 ppm, but since industrial revolution, it has increased to over 420 ppm.[6] As a result, the global average surface temperature has increased by approximately 1.1°C since the late 19th century, with the 10 warmest years all recorded in the 21st century.[7] Moreover, the oceans are also getting warmer, which leads to the shrinking of ice sheets and rising of sea levels.[8] The rapid climate change is causing more extreme weather conditions, e.g., stronger hurricanes and more intense heat waves.[9–11]

Aiming to mitigate the impacts of climate change and reduce associated risks, 196 Parties of the 2015 United Nations Climate Change Conference near Paris adopted an international treaty on climate change, Paris Agreement. The objective of the Agreement is to limit global warming in this century to well below 2°C (compared to pre-industrial levels), and preferably to limit it to 1.5°C. The 1.5°C goal requires 50% reduction of global CO_2 emissions by 2030, and carbon neutral by mid-century.[12] However, we are not on track to reach these reduction goals. During the period of 2010 – 2019, the average annual greenhouse gas emissions were higher than any previous decades (**Figure 1.1**).[13] Although the growth rate of the emissions is slowing down, current climate actions are not enough to reach the 1.5°C target unless immediate and deep emissions reductions across all sectors are taking place.[14]

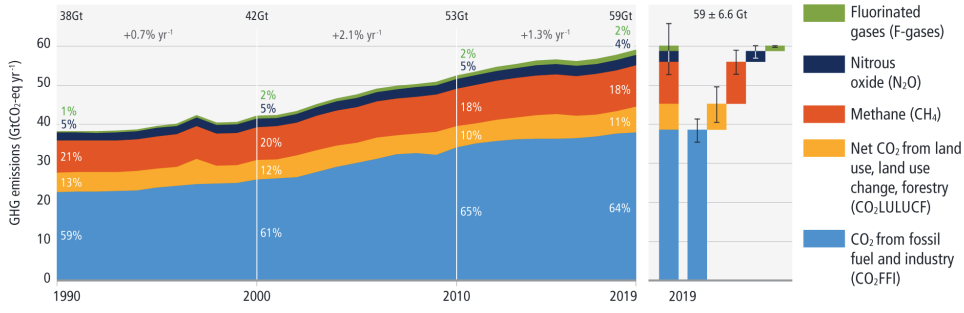

Figure 1.1. Global net anthropogenic greenhouse gas (GHG) emissions 1990 – 2019.[13]

1.2. Approaches for reducing CO_2 emissions

Carbon dioxide, among all the greenhouse gases, is the main driver of climate change. To mitigate the effects of climate change, it is crucial to reduce CO_2 emissions. The Intergovernmental Panel on Climate Change (IPCC) has identified various mitigation options across different sectors, including electrification and carbon capture and storage (CCS) as the key solutions in the energy and industry sectors.[12,13,15]

1.2.1. Electrification

Electrification is the process of replacing the original energy source (normally fossil fuel based) by electricity, employing electricity both energy supply and the end uses. According to the International Energy Agency (IEA), electrification has the potential to significantly reduce final energy demand due to the comparatively higher efficiency of electric technologies compared to fossil fuel-based alternatives that provide similar energy services.[16] This increased efficiency results in a reduction in energy consumption, which leads to reduced CO_2 emissions and improved energy security.

Moreover, the integration of renewable energy sources, such as solar, wind, and hydroelectric power, with the process of electrification has the potential to further reduce CO_2 emissions by reducing the carbon intensity of the electricity system.[17–19] According to the Net Zero Scenario of IEA, electrification has the potential to reduce 1 Gt of CO_2 emissions in 2030 compared to 2020, accounting for approximately 7% of all mitigated emissions in these 10 years.[16] By 2021, the global total renewable energy capacity has reached 3.1 TW accounting for 38.3% of the total energy generation capacity.[20] Since the costs for some renewables (e.g., photovoltaic and onshore wind) have become lower than those of fossil fuels,[21,22] the widespread adoption of these renewable energy sources becomes more viable. Furthermore, the increase in the number of electricity end uses can also provide more flexible capacity to the electricity system, which mitigates the challenges associated with integrating variable renewable sources.[23]

Finally, hydrogen (H_2) production based on water electrolysis is another indirect form of electrification. The produced H_2 can be the alternative fuel for various applications, including long-haul transport, chemical productions, and iron and steel industries.[24,25] However, only about 1% of the current global H_2 production is from renewable energy, with more than 95% of the production still relies on fossil fuels.[26] To establish a role in the reduction of CO_2 emissions, the future of development of the H_2 economy should increase the share of H_2 production from renewable electricity.

1.2.2. Decarbonization technologies

Carbon capture and storage

During the energy transition, the CO_2 emissions from fossil fuel powered facilities remain substantial. In 2022, the global CO_2 emissions from fossil fuels were estimated to be 37.5 Gt.[27] To offset these emissions and reach net-zero goals, it is imperative to implement additional technologies. Carbon capture and storage (CCS) is such a technology that aims to capture CO_2 emissions from point sources, such as power plants and industrial facilities, and store them underground.[28,29] This process can reduce the amount of CO_2 released into the atmosphere, thereby playing a crucial role in reducing the overall greenhouse gas emissions. The IPCC has identified CCS as a key mitigation option for achieving significant reductions in CO_2 emissions in both energy and industry sectors.[13]

The deployment of CCS is a critical for achieving long-term climate goals and mitigating risks through decarbonizing hard-to-abate industries, producing low-carbon power, and facilitating the mass H_2 production with CCS.[30] As of September 2022, a total 30 CCS facilities are in operation with the capacity to capture 42.5 $MtCO_2$ per annum, while additional 164 CCS facilities with a total capacity of 199.0 $MtCO_2$ per annum are under construction or in development.[31] Together with other mitigation options, such as electrification, the potential contribution of CCS to the net emission is expected be approximately 990 $MtCO_2$ per annum by 2030, with 840 $MtCO_2$ per annum in energy sector and 150 $MtCO_2$ per annum in industry sector.[13] Obviously, there is a significant disparity between the current level of CCS deployment and the requirement of the net-zero emissions by 2050 scenario. Thus, immediate and more intensive actions are required for the policy support and adoption of CCS. Moreover, the development of further CO_2 emission reduction technologies is necessary to support the mitigation process.

Carbon dioxide removal

While CCS is targeting point source emissions, carbon dioxide removal (CDR) is aiming to remove CO_2 directly from the atmosphere, which complements CCS in reducing atmospheric CO_2 concentration. The deployment of CDR is crucial to counterbalance CO_2 emissions from non-point sources, such as transportation and residential sources.[32] CDR has been recognized by IPCC as unavoidable to reach net-zero emissions.[13] A range of methods have been developed for CDR, including afforestation and reforestation, bioenergy with carbon capture and storage (BECCS), and direct air carbon capture and storage (DACCS).[13,33–35]

Afforestation and reforestation involve planting trees and other vegetation to absorb CO_2 from the air through photosynthesis and store it in the form of biomass. According to the latest IPCC report, the potential for CO_2 sequestration through this process is estimated to be between 0.5 and 1.0 $GtCO_2$ per annum.[13] In addition to the mitigation of climate change, afforestation and reforestation can offer numerous benefits, such as increased employment

opportunities and improved livelihoods for local communities, enhanced biodiversity, a greater availability of renewable wood products, and improved soil carbon and nutrient cycles. However, the effective implementation of afforestation and reforestation requires proper management to mitigate potential risks, including lower groundwater levels and competition with food production for land use.[36,37]

BECCS is a technology that combines the generation of bioenergy with the capture and permanent CO_2 storage. The process begins with the cultivation of energy crops such as miscanthus, switchgrass, short rotation coppice willow, which are then burned to produce steam to drive turbines and generate electricity.[38] The CO_2 emitted during the combustion process is captured and compressed for transport and storage. The entire process results in a net removal of CO_2 from the atmosphere, effectively making the produced electricity carbon negative. BECCS is the only CDR process that can provide a "sustainable" source of energy, and it has the advantages of afforestation as the bioenergy step requires cultivation of energy crops. Nevertheless, the land and water required for energy crops cultivation are significant, and the cost and feasibility of the process largely depend on the development of CCS technologies. While IPCC expected BECCS to have a mitigation potential between 0.5 and 11 $GtCO_2$ per annum, current deployed facilities can only capture around 2 $MtCO_2$ per annum.[39] Further research on the BECCS value chain, development on BECCS technologies, and policy support for BECCS investments are necessary to promote the large-scale deployment of the technology.[38,40]

DACCS includes capturing CO_2 from the air and the sequestration of the captured CO_2. The capturing process, called direct air capture (DAC), typically uses a scrubber that can capture CO_2 directly from the atmosphere through chemical reactions, then the sorbents in the scrubber are regenerated via various methods,[41] and high purity CO_2 is produced during the regeneration. In general, the technology is still in the prototyping stage (technology readiness level ~ 6) and has an estimated cost between 100 and 300 USD tCO_2^{-1}.[13] However, the recent advancements have demonstrated its long-term mitigation potential, with estimates ranging from 5 to 40 $GtCO_2$ per annum.[13] Two of the leading companies working on DAC are Climeworks and Carbon Engineering.

Climeworks uses an adsorption/desorption process based on alkaline-functionalized solid adsorbents (**Figure 1.2**).[42,43] The adsorption and desorption phases are performed in the same modular designed devices called CO_2 collectors. During the adsorption phase, ambient air is ventilated along the adsorbents in the collectors due to chemical binding. When the adsorbents are saturated with CO_2, the process moves to the desorption phase. The desorption phase involves a temperature-vacuum-swing (TVS) process,[44] where the CO_2 collectors are heated to around 100°C so that CO_2 can be desorbed from the adsorbents and collected via an applied vacuum. After the desorption phase, the system is cooled to ambient temperature for the starting of the adsorption phase again. Climeworks deployed its first demonstration prototype in 2012 and world's first commercial DAC plant in 2017. In 2021, world's first

large-scale DACCS plant "Orca" was launched in Iceland with a full capture capacity of 4 $ktCO_2$ per annum. Currently, Climeworks is building the latest DACCS plant "Mammoth" with a full capacity of 36 $ktCO_2$ per annum, continuing its plan of multi-megaton capacity by 2030 and being on track to gigaton capacity by 2050.

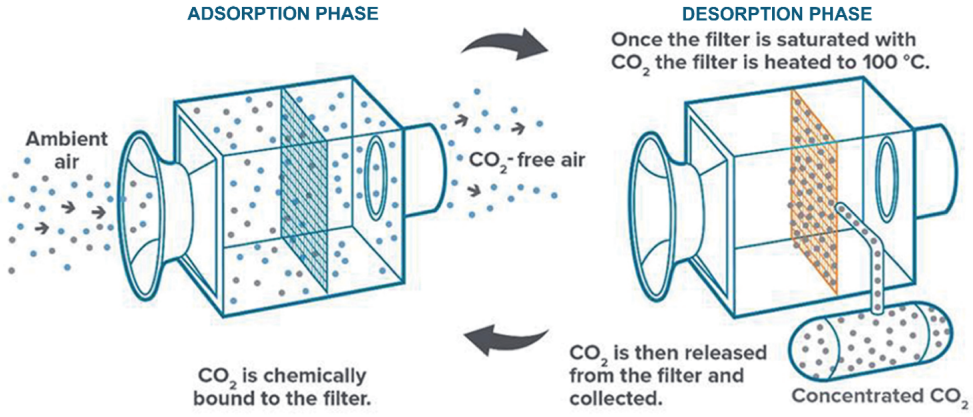

Figure 1.2. Schematic illustration of Climeworks direct air capture process. (Adapted from ref [42])

The DAC technology from Carbon Engineering has four steps based on a liquid alkaline absorbent (KOH) (**Figure 1.3**). The absorption of CO_2 occurs in an air contactor, where CO_2 from the air reacts with KOH solution and forms K_2CO_3 solution. The carbonate solution flows into the pellet reactor and reacts with $Ca(OH)_2$ to form $CaCO_3$ pellets. The pellets are heated up to 900°C in the calciner to desorb high purity CO_2 gas. The other product in the calciner, CaO, is hydrated in a slaker to produce $Ca(OH)_2$ to be recycled in the process. Based on the pilot data from Carbon Engineering and model simulations, the levelized cost of the process is estimated to be 94 – 232 USD tCO_2^{-1}. In partnership with another company 1Point-Five, now Carbon Engineering is constructing its first large-scale commercial DAC plant, aiming for 100 $MtCO_2$ per annum with multiple DAC plants.

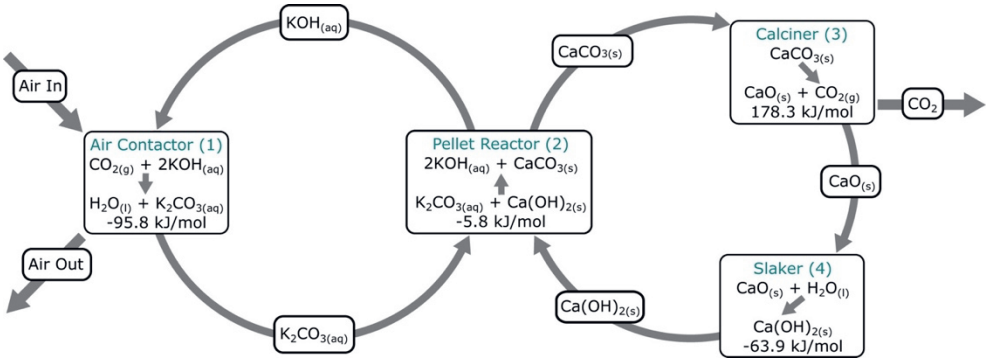

Figure 1.3. Process scheme of Carbon Engineering DAC process.[45]

1.3. Electrochemical carbon capture

A conventional carbon capture technologies typically use amine scrubbing to capture CO_2 and temperature swing to regenerate the amine-based organic solvents.[28] However, the availability of thermal energy and the degradation of solvents under high temperature limited the application of the technologies. On the other hand, electrochemical carbon capture technologies,[46–48] that can operate at room temperature without heating, have recently drawn a lot of attention (**Figure 1.4**). They have several advantages including easy integration into existing power plants and industrial processes, high scalability due to modular cell design, and being environmentally friendly with no harmful byproducts. Furthermore, as the process is powered by electricity, the whole process can be carbon neutral or even carbon negative when integrated with renewable energy.

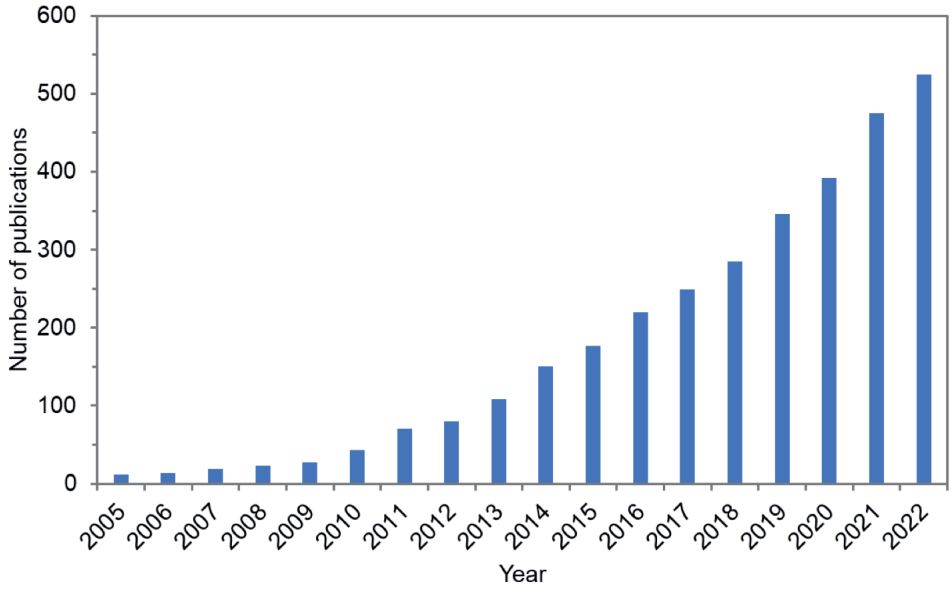

Figure 1.4. Number of publications per year on "electrochemical carbon capture". (Data fetched by Web of Science on 14th of February 2023)

The CO_2 equilibria (eqs. 1.1 & 1.2) in a liquid solution are largely dependent on the pH of the solution (**Figure 1.5**). Due to the displacement of the equilibria, CO_2 could be desorbed into the gas phase from the solution under a low pH when the dissolved CO_2 ($H_2CO_3^*$) is over-saturated. While CO_2 is reactive with OH^-, a high pH solution is capable to capture CO_2 from gas mixtures. Therefore, some electrochemical carbon capture technologies (e.g., technologies based on bipolar membrane electrodialysis (BPMED)[49–51] and proton-coupled electron transfer molecules[52,53]) have been developed to produce a pH swing of a liquid sorbent, and CO_2 is absorbed by the sorbent at a high pH and desorbed from the sorbent at a low pH. Furthermore, some other electrochemical processes that are based on the capacitive or redox

properties of the electrodes have also been demonstrated for carbon capture (e.g., technologies based on membrane capacitive deionization (MCDI)[54,55] and electrochemically mediated amine regeneration (EMAR)[56–58]).

$$H_2CO_3^* \rightleftharpoons HCO_3^- + H^+ \quad (1.1)$$

$$HCO_3^- \rightleftharpoons CO_3^{2-} + H^+ \quad (1.2)$$

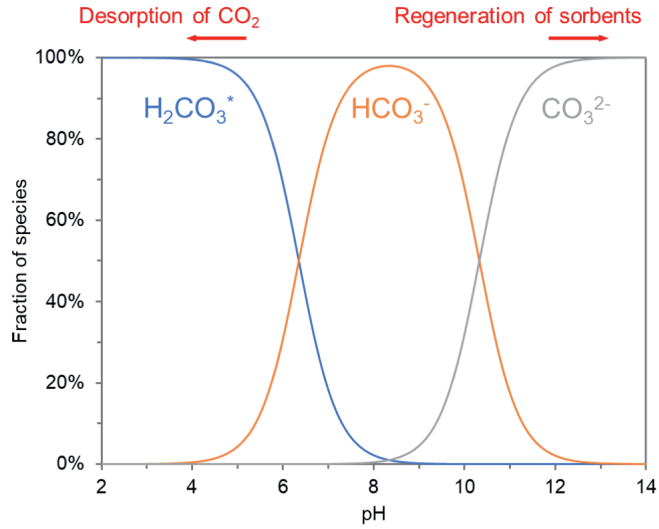

Figure 1.5. Distribution of carbon species in solutions under different pH.

1.3.1. pH-swing-based technologies

BPMED is typically combined with wet scrubbing to achieve carbon capture.[59] The wet scrubbing process involves CO_2 absorption using liquid alkaline solution, and the product of the process is carbonate/bicarbonate solution.[60] The BPMED cell is used for regenerating the alkaline absorbent and producing high-purity CO_2 gas. This technique is relying on the water splitting capability of the bipolar membrane to create a pH swing to displace the carbonate equilibria in the liquid solution. When stacked with anion exchange membranes (AEMs) (as shown in **Figure 1.6**), a pH swing is established in two adjacent compartments, acid compartment and base compartment. The acidic environment in the acid compartment facilitates the desorption of CO_2 gas, while the alkaline environment in the base compartment regenerates the alkaline absorbent. A techno-economic analysis of the BPMED regeneration step showed that the energy consumption of the process can be as low as 236 kJ mol^{-1} CO_2 for DAC application.[59] Various improvement strategies of BPMED have been proposed to further reduce the energy consumption, including high pressure operation, cation exchange membrane (CEM) design, and acid production.[50,51,61] However, the current high cost of the bipolar membranes and ion exchange membranes limits the large-scale application of the technology.

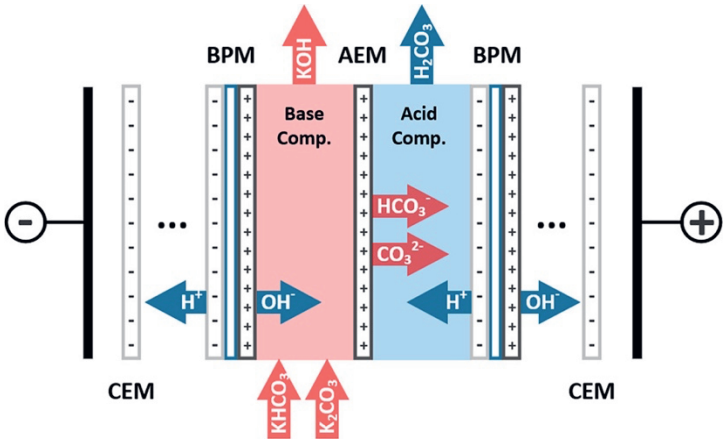

Figure 1.6. Scheme of the repeated units in a BPMED cell. BPM: bipolar membrane, AEM: anion exchange membrane, CEM: cation exchange membrane.[59]

Other than pH swing generated by bipolar membranes, redox reactions with proton-coupled electron transfer molecules can also provide a pH swing (**Figure 1.7**).[52,53] The reduction of sodium (3,3'-(phenazine-2,3-diylbis(oxy))bis(propane-1-sulfonate)) (DSPZ) molecules increases the alkalinity of the solution, which favors the absorption of CO_2 from flue gas. When the polarities of the electrodes are reversed, the oxidation of DSPZ increases the acidity of the solution, which facilitates the desorption of pure CO_2 gas. The energy consumption of the system is 61 – 145 kJ mol^{-1} CO_2 for flue gas carbon capture and 121 – 237 kJ mol^{-1} CO_2 for DAC. Due to the fast kinetics of DSPZ redox reactions, this process can be operated under a relatively high current density (up to 1500A m^{-2}). However, the reduced form of DSPZ can be oxidized by oxygen (O_2) from flue gas or air, which leads to the loss of coulombic efficiency. Although Jin et al. have proposed an electrochemical rebalancing method to mitigate the negative effects of O_2, due to the high energy intensity of the method, the development of O_2-insensitive redox molecules would be the focus for future research. [53]

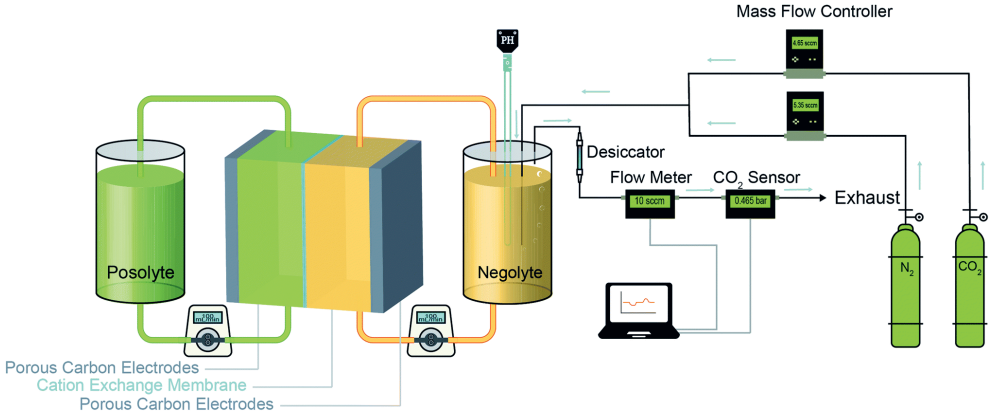

Figure 1.7. Scheme of the electrochemical pH swing process with proton-coupled electron transfer molecules, posolyte: $Fe(CN)_6$, negolyte: DSPZ.[52]

1.3.2. Capacitive or redox-based technologies

MCDI cell consists of two capacitive electrodes with a CEM and an AEM on either electrode, respectively (**Figure 1.8**).[54,55] Deionized water works as a medium for the absorption and desorption of CO_2. During the absorption step, CO_2 from flue gas dissolves in the deionized water and forms carbonic acid (H_2CO_3) that further dissociates to bicarbonate (HCO_3^-) and carbonate (CO_3^{2-}). The charged anode adsorbs anions (HCO_3^- and CO_3^{2-}), while the charged cathode adsorbs cations (H^+). The reduction of HCO_3^-/CO_3^{2-} concentration in the liquid facilitates the dissolution of more CO_2 from gas to liquid. Hence, CO_2 is captured in the capacitive electrodes in the form of HCO_3^- and CO_3^{2-}. The desorption step is performed by reversing the polarity of the electrodes, where HCO_3^- and CO_3^{2-} are desorbed back into the deionized water medium. The oversaturation of HCO_3^- and CO_3^{2-} favors the desorption of CO_2 into the gas phase. Overall, the energy consumption of the MCDI system can be as low as 40 kJ mol^{-1} CO_2 for carbon capture from flue gas.[55] Nevertheless, the use of deionized water as the medium provides a huge internal resistance to the cell, the low energy consumption can only be achieved under an extremely low current density (0.2 A m^{-2}). Moreover, the electrodes do not have selectivity towards HCO_3^- and CO_3^{2-}, so the introduction of any other anions would decrease the current efficiency of the system.[54] Therefore, the future research focus should be on reducing the internal resistance and increasing the ion selectivity of the electrodes.

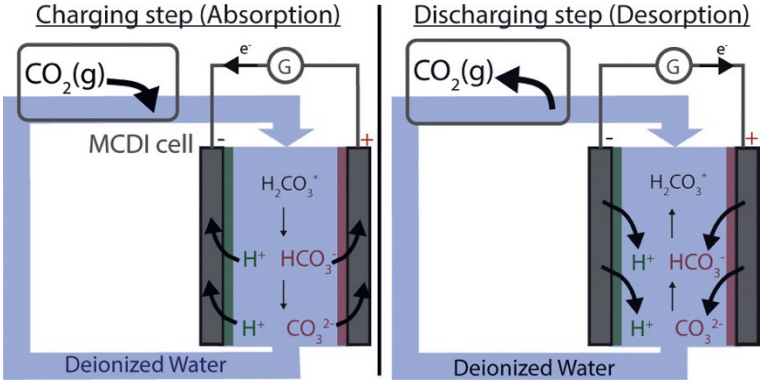

Figure 1.8. Scheme of an MCDI system in absorption and desorption steps.[62]

EMAR is an electrochemical regeneration process for liquid amine absorbents (**Figure 1.9**).[57,63,64] CO_2 from flue gas is captured by ethylenediamine (EDA) solution during the amine-scrubbing absorption step. The CO_2-rich spent absorbent is directed into the anode compartment of the EMAR cell, where the copper electrode is oxidized and releases Cu^{2+} into the solution. The Cu^{2+} ions displace the CO_2 to be bound by EDA due to the stronger affinity. As a result, CO_2 is desorbed from the solution. The amine-Cu complex is regenerated back to EDA at the cathode, as Cu^{2+} is reduced to Cu that deposits onto cathode surface. The energy consumption of this system is in the range of 30 – 113 kJ mol^{-1} CO_2 under current densities of 27 – 118 A m^{-2} for flue gas carbon capture.[57] The internal resistance of the cell needs to be further reduced so that higher current density could be applied. Moreover, the long-term stability of the copper electrodes requires more research investigation before large-scale application of the technology.

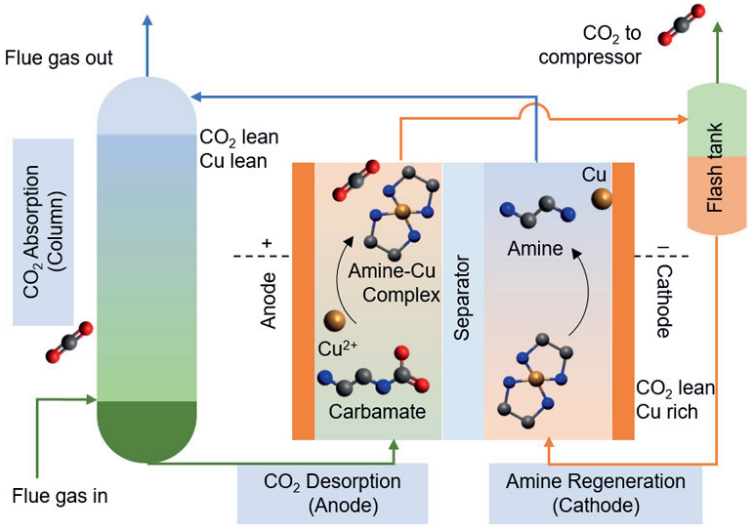

Figure 1.9. Scheme of the EMAR process in combination with a CO2 absorption column.[57]

1.4. Scope and thesis outline

With the deployment of electrification and development of renewable energy, the access to renewable electricity will become easier and cheaper. Moreover, while carbon capture from point sources is important to reduce the CO_2 emissions from power plants and industries, direct air capture is essential to achieve the net-zero emission goals. Therefore, this thesis aims to develop a novel electrochemical DAC technology to help mitigate climate change caused by increasing atmospheric CO_2 concentration.

The developed DAC technology is depicted in **Figure 1.10**. The key process of this technology is the H_2-recycling electrochemical system (HRES) that can generate a pH swing for the influent solution. The electrochemical cell consists of three compartments: the anode, acidifying, and cathode compartments. The oxidation of H_2 at the anode and the reduction of H_2O at the cathode generates a pH gradient between the acidifying and cathode compartments. When the HRES is integrated with CO_2 capture using an alkaline solution (NaOH or KOH), the low pH in the acidifying compartment of the electrochemical cell facilitates the desorption of high-purity CO_2 gas from the spent solution, while the high pH in the cathode compartment regenerates the alkalinity of the solution. This technology is based on the pH swing of an inorganic solution, which avoids the limitations of using organic substances that tends to react with O_2 (e.g., DSPZ) and can possibly degrade over time[52]. Moreover, the large-scale application of a DAC technology requires a high current density to reduce the capital expenditure (CAPEX) of the system. The developed technology in this thesis relies on the H_2 oxidation and H_2 evolution reactions (HOR and HER) to generate the pH swing, while the materials and methods for these two reactions have been matured in fuel cells[65–67] and electrolyzer[68–70] technologies at high current density (>> 1000A m^{-2}). Furthermore, the electrochemical cell has been combined with the adsorption of CO_2 from air using amine-functionalized ion exchange resins. The solid amine sorbent has a high CO_2 capture capacity, and the regeneration process using the electrochemical cell prevents the thermal degradation of the sorbent.

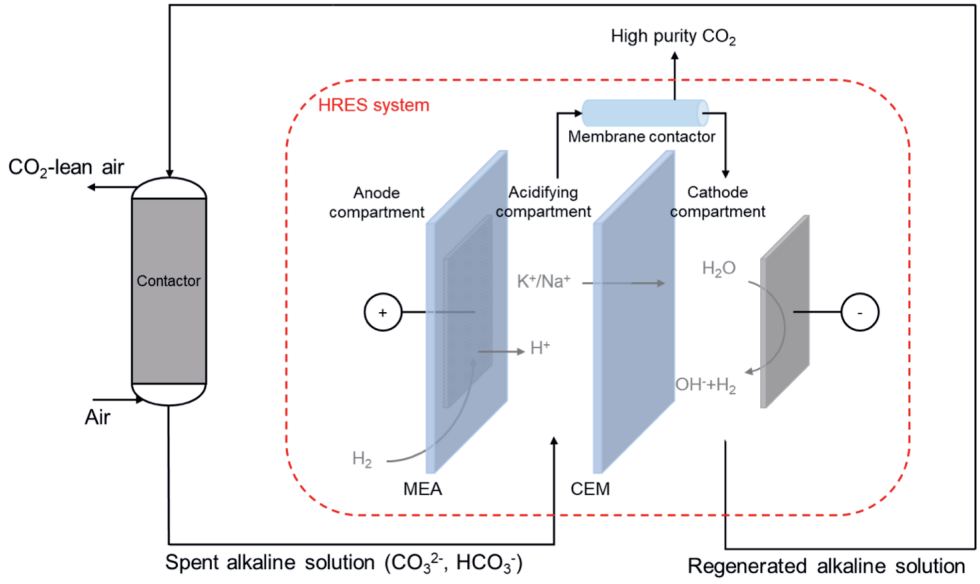

Figure 1.10. Schematic illustration of the developed electrochemical DAC process. MEA: membrane electrode assembly, CEM: cation exchange membrane.

Chapter 2 shows the proof of concept of a hydrogen recycling electrochemical system for regeneration of spent alkaline DAC absorbents. The system utilizes the pH swing created from H_2 oxidation and H_2 evolution reactions to facilitate the desorption of high purity CO_2 gas and regeneration of the alkaline absorbents.

Chapter 3 demonstrates the integration of the electrochemical regeneration system with an adsorption process using amine-functionalized anion exchange resins. The resins adsorb CO_2 from ambient air, and the electrochemical cell produces the alkaline solution to regenerate the resins and desorbs high purity CO_2 gas. The stability of the resins and the impact of air humidity are investigated.

Chapter 4 explores several optimization strategies for the electrochemical system to reduce the energy consumption. Decreased CO_2 desorption pressure increases the driving force for transport of CO_2 from liquid to gas, and the addition of background electrolyte increases electrical conductivity of the solutions in the cell.

Chapter 5 further extends the optimization of the system to process designs and operating parameters. With a mathematical model, different process layouts are theoretically investigated to minimize the negative effects of CO_2 gas bubbles. The impacts of circulation of solution, current density, and concentration of background electrolyte are also studied.

Chapter 6 compares the developed technology with other existing carbon capture technologies. The challenges in the studies of this thesis are discussed, and the perspectives on future research are presented. Finally, the vision towards a sustainable carbon cycle is shared.

Chapter 2

Electrochemical regeneration of spent alkaline absorbent from direct air capture

This chapter has been published as:
Shu, Q., Legrand, L., Kuntke, P., Tedesco, M., & Hamelers, H. V. M. (2020).
Electrochemical Regeneration of Spent Alkaline Absorbent from Direct Air Capture.
Environmental Science and Technology, 54(14). https://doi.org/10.1021/acs.est.0c01977

Abstract

CO_2 capture from the atmosphere (or direct air capture) is widely recognized as a promising solution to reach negative emissions, and technologies using alkaline solutions as absorbent have already been demonstrated on a full scale. In the conventional temperature swing process, the subsequent regeneration of the alkaline solution is highly energy-demanding. In this study, we experimentally demonstrate simultaneous solvent regeneration and CO_2 desorption in a continuous system using a H_2-recycling electrochemical cell. A pH gradient is created in the electrochemical cell so that CO_2 is desorbed at a low pH, while an alkaline capture solution (NaOH) is regenerated at a high pH. By testing the cell under different working conditions, we experimentally achieved CO_2 desorption with an energy consumption of 374 kJ mol^{-1} CO_2 and a CO_2 purity higher than 95%. Moreover, our theoretical calculations show that a minimum energy consumption of 164 kJ mol^{-1} CO_2 could be achieved. Overall, the H_2-recycling electrochemical cell allowed us to accomplish the simultaneous desorption of high-purity CO_2 stream and regeneration of up to 59% of the CO_2 capture capacity of the absorbent. These results are promising toward the upscaling of an energy-effective process for direct air capture.

2.1. Introduction

Climate change is one of the most critical global challenges nowadays. Increasing atmospheric CO_2 concentration brought by anthropogenic emissions has been recognized as the primary driver of global warming.[71–75] The global average surface temperature has risen by 0.85°C in the period from 1880 to 2012, and over 85% of this temperature rise occurred in the past century can be attributed to industrialization.[76] Besides, most of the CO_2 in the atmosphere will ultimately be absorbed by the oceans causing ocean acidification, which has been proved harmful to marine organisms.[77] The ocean pH has been already reduced by 0.1 units compared to the preindustrial level,[78] and it could eventually be 0.7 units lower with continuous emission of CO_2 from the combustion of fossil fuels.[78,79]

In this context, it has been widely recognized that capturing CO_2 from emission points and even directly from the air provides a potential solution to mitigate CO_2 emissions and ultimately reduce the atmospheric CO_2 concentration.[80,81] In particular, direct air capture (DAC) technologies, aim to extract CO_2 directly from ambient air, and hence offer the possibility to achieve CO_2 capture from distributed sources.[41,82,83] Therefore, DAC is not restricted by location as conventional carbon capture technologies that are designed to be coupled with large CO_2 emission points. The thermodynamic minimum energy requirement for DAC is relatively higher compared to carbon capture from flue gas, due to the low CO_2 concentration in air.[83] Nonetheless, further studies on DAC are essential for reducing climate risks.

Various technologies have been proposed for DAC,[41,45,84] and one of the most extensively studied approaches is wet scrubbing with alkaline hydroxide solutions (typically NaOH or KOH).[45,60,85] When air is in contact with an alkaline solution (e.g., NaOH), CO_2 is absorbed, and a sodium carbonate solution is produced according to the reaction:[41]

$$2NaOH + CO_2 \rightarrow Na_2CO_3 + H_2O \; \Delta H^0 = -109.4 \; kJ \; mol^{-1} \tag{2.1}$$

Conventionally, the sorbent (NaOH) is regenerated by exchanging sodium and calcium ions by dosing calcium hydroxide. Subsequently, the resulting calcite ($CaCO_3$) precipitate is thermally treated at 700 °C to produce CO_2 and calcium oxide. Finally, calcium hydroxide can be regenerated by rehydration of calcium oxide.

Since the chemical reaction between NaOH and CO_2 is spontaneous, the regeneration of the alkaline sorbent (coupled with desorption of CO_2 gas) consumes the largest fraction of energy in the conventional wet scrubbing process (i.e., a minimum of 179 kJ mol^{-1} CO_2 at standard temperature and pressure[85,86]). Alternative regeneration processes have been developed to reduce energy consumption. For instance, Mahmoudkhani and Keith proposed a titanate cycle that halved the energy requirements compared to the conventional regeneration process,[85] while Kim et al. suggested an electrochemical method for the regeneration of LiOH from used CO_2 adsorbents. [87] The use of electrochemical systems as the CO_2 desorption step

includes a number of advantages, such as (i) potentially low energy consumption (since the process occurs at room temperature), (ii) better operational control (by exploiting the electric field), and (iii) easy integration with renewable energy sources (since the process requires only electricity as energy input).[49,54,55,59,61,88–90]

In this work, we developed an electrochemical process for regenerating the alkaline solution in the wet scrubbing process for DAC application; meanwhile, high purity CO_2 gas stream could be produced that is suitable for storage or utilization. The process is based on a H_2-recycling electrochemical system (HRES) coupled to a membrane contactor that was originally developed for nitrogen recovery from wastewater.[91,92] In HRES, alkaline and acidic conditions are created in two adjacent compartments respectively. Additionally, CO_2 equilibria are highly dependent on the pH of the solution (eqs. 2.2 – 2.4, values taken from refs [93,94]). Accordingly, we adapted the system operation for DAC application. The electrochemical cell consisted of three compartments, i.e., an anode compartment, an "acidifying" compartment, and a cathode compartment. During the operation, protons (H^+) produced from the H_2 oxidation at the anode are transported to the acidifying compartment where the spent solution coming from the air contactor is fed. The decreasing pH of the acidifying solution leads to the conversion of (bi)carbonate ions to carbonic acid (eqs. 2.2 and 2.3). When the solution is saturated in carbonic acid ($H_2CO_3^*$, including dissolved CO_2), a further pH decrease leads to the desorption of CO_2 gas (eq. 2.4). The oversaturation point is determined by the CO_2 partial pressure in the membrane contactor. Meanwhile, NaOH is regenerated in the cathode due to the production of hydroxides (OH^-) and can be reused as a DAC absorbent.

$$HCO_3^- \rightleftharpoons CO_3^{2-} + H^+ \; pK_{a2} = 10.33 \tag{2.2}$$

$$H_2CO_3^* \rightleftharpoons HCO_3^- + H^+ \; pK_{a1} = 6.35 \tag{2.3}$$

$$CO_2 + H_2O \rightleftharpoons H_2CO_3^* \; K_H = 0.0339 \; mol \; L^{-1} \; atm^{-1} \tag{2.4}$$

In this work, we show a proof of principle of such electrochemical method for NaOH regeneration and CO_2 desorption using an HRES. Different operational conditions were studied to identify suitable conditions to regenerate the absorbent at low energy consumption.

2.2. Materials and methods

2.2.1. Experimental methodology

Experimental setup

A schematic representation of the experimental setup is shown in **Figure 2.1**. The main process streams are the influent flowing into the acidifying compartment and then the membrane contactor, the overflow of excess acidifying solution flowing into the catholyte tank, and the effluent from the cathode compartment. To increase the flow speed inside the cell, two recirculation loops were added for the acidifying and cathode compartment, respectively. The

anode was a membrane electrode assembly (MEA) consisting of a 15 cm × 15 cm Nafion N117 cation exchange membrane (CEM) integrated with a 10 cm × 10 cm gas diffusion layer (GDL) coated by a Platinum – Vulcan (carbon) catalyst (0.5 mg Pt cm^{-2}) (FuelCellsEtc, USA). The GDL side of the MEA was facing the anode compartment while the CEM side was facing the acidifying compartment. The flow channel of the acidifying compartment was created by using a polymeric (nitril) spacer (500 µm, Sefar, Switzerland). The acidifying compartment and the cathode compartment were separated by a CEM (Nafion N117, 15 cm × 15 cm, FuelCellsEtc, USA). Two Ru/Ir coated titanium mesh electrodes (9.8 cm × 9.8 cm, Magneto Special Anodes BV, the Netherlands) were used in the cell, one as cathode, and the other one as current collector for the anode. The whole cell was closed between two poly(methyl methacrylate) (PMMA) endplates (21 cm × 21 cm × 2.5 cm). The HRES produces and consumes H_2 at the electrodes, thus the system can operate without any net H_2 consumption by recirculating the H_2 from the cathode to the anode. However, to simplify the operation of the system, the H_2 feed to the anode compartment was produced by a custom-made electrolyzer. The electrolyzer was operated under constant current conditions and fed with a 25 mM H_2SO_4 aqueous solution.

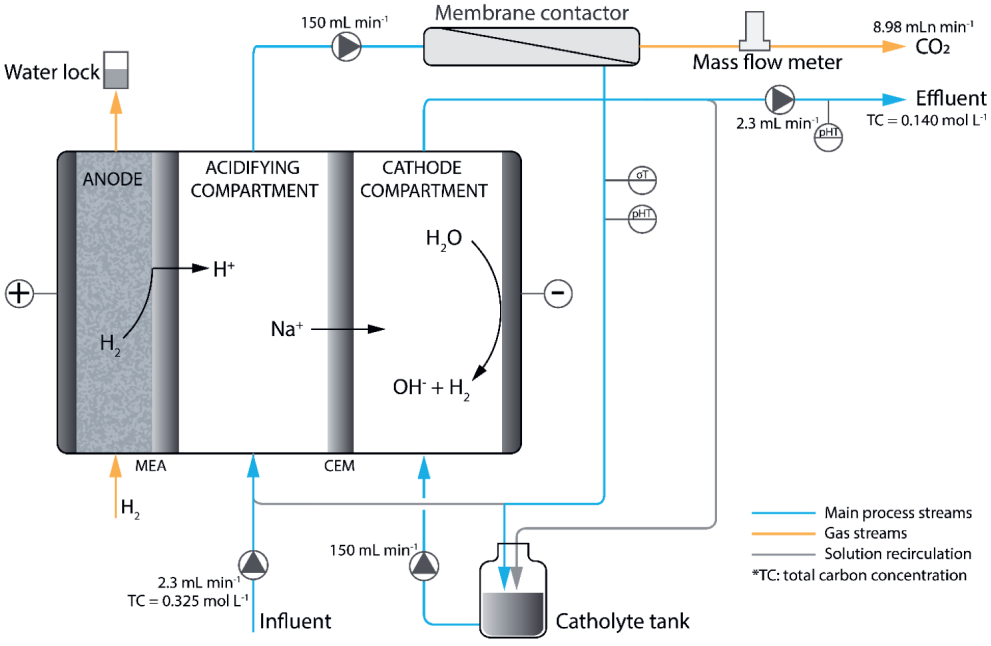

Figure 2.1. Schematic drawing of the experimental setup. The values indicated in the figure are from one of the experiments performed in this work.

The gas-liquid separation was conducted by a membrane contactor (type MM 1.7 × 8.75, 3M, USA) whose microporous hollow fiber membrane provided a large surface area for contact between gas and liquid phases. The produced gas first passed through a Nafion Tubing (TUB-0003, CO2Meter.com, USA) to remove water vapor. Next, the amount of gas

produced was measured by a mass flow meter (EL-FLOW Prestige FG-111B, Bronkhorst, the Netherlands). Finally, the gas composition was checked by micro gas chromatograph (CP-4900, Varian, USA).

Three peristaltic pumps (Masterflex L/S, Metrohm Applikon BV, the Netherlands) were used in the system, one for the influent, one for the effluent, and one for the recirculation of solution in acidifying and cathode compartment (150 mL min^{-1}). The total volume of the acidifying compartment recirculation was 180 mL, including the flow channels of the acidifying compartment (~5 mL), membrane contactor (~70 mL), and tubing (~105 mL). The cathode compartment recirculation had a total volume of 120 mL.

The anode (MEA) potential and cathode potential were measured by two Ag/AgCl reference electrodes (+0.2 V vs NHE, QM711X, QiS-Prosence BV, the Netherlands) placed at the inlets of the acidifying and cathode compartments, respectively. Two high impedance preamplifiers (Ext-Ins Technologies, the Netherlands) were connected to the reference electrodes to avoid current leakage. The conductivities of the solutions in the acidifying and cathode compartment were measured using a conductivity sensor (Memosens CLS82D, Endress+Hauser BV, the Netherlands). The pH of the solution in the acidifying compartment was measured using a pH sensor (Orbisint CPS11D, Endress+Hauser BV, the Netherlands). Constant current was applied to the electrochemical cell by a power supply (ES 030-5, Delta Elektronika BV, the Netherlands). The Na^+ concentration in the solution was measured by ion chromatography (761 Compact IC, Metrohm, Switzerland).

Transport of Na^+ and definition of Na^+ load ratio

The Na^+ in the system has mainly two roles: (i) supporting the electrical conductivity in the acidifying compartment, and (ii) being transported through the membrane to sustain the ionic current in the cell. The net transport of Na^+ through the CEM is influenced by several operating conditions, such as the loading rate of Na^+ in the system (i.e., the molar concentration and flow rate of the influent), as well as the applied current. Here, we define the "Na^+ load ratio" (L_{Na^+}) as the ratio between the current density and the Na^+ loading rate :[95]

$$L_{Na^+} = \frac{j_c A}{c_{Na^+,0} Q F} \tag{2.5}$$

Where j_c is the applied current density (A m^{-2}), A the active membrane area (0.01 m^2), $c_{Na^+,0}$ the molar concentration in the influent solution (500 mol m^{-3}), Q the flow rate of the influent (m^3 s^{-1}), and F the Faraday constant (96485 C mol^{-1}). The Na^+ load ratio (L_{Na^+}) is a dimensionless parameter that describes the ratio between the potential transport of Na^+ at given current density and the amount of Na^+ fed into the system. In principle, when L_{Na^+} = 1, the current in the cell is sufficient to transport all the sodium towards the cathode. Thus, all the (bi)carbonate ions react with protons leading to the maximum desorption of CO_2 and regeneration of absorbent.

Besides, L_{Na^+} can also be expressed as following:

$$L_{Na^+} = \frac{j_c \tau}{c_{Na^+,0} F d} \quad (2.6)$$

Where τ is the residence time of the solution in the acidifying compartment (s), d the thickness of the acidifying compartment (5×10^{-4} m). The L_{Na^+} is proportional to the τ when the current density applied is fixed. Therefore, in the scope of this work, a higher L_{Na^+} implies a longer residence time of the solution in the cell.

Experimental procedure

All the experiments were performed in continuous mode, according to the scheme in **Figure 2.1**. The composition of the influent was chosen in order to mimic a spent capture solution from a DAC process. Specifically, we considered a 0.5 M NaOH aqueous solution as absorbent, and we assumed that the capture step is completed when CO_2 in the gas phase and in the liquid phase reaches equilibrium. As a result, the spent absorbent solution consists of 0.175 M Na_2CO_3 and 0.150 M $NaHCO_3$, based on Henry's law and the CO_2 equilibria shown in eqs. 2.2 – 2.4. The spent absorbent solution has pH of 9.7, and conductivity of 30.6 mS cm^{-1}.

Firstly, experiments at different L_{Na^+} values were performed while keeping the current density constant. Then the effect of current density was investigated at constant L_{Na^+} values. The experiments were performed until the system reached steady-state (i.e., by monitoring the outlet conductivity). **Table S2.1** shows an overview of all the experiments that were performed.

Figures of merit

Here, we define the figures of merit associated with energy consumption and the regeneration of the alkaline absorbent. The specific energy consumption of the system (EC, J mol^{-1}) is defined as

$$EC = \frac{V_{cell} I + P_{H_2}}{jco_2} \quad (2.7)$$

Where V_{cell} is the cell voltage (V), I the applied current (A), P_{H_2} the power for production of 10% excess H_2 in the electrolyzer (W), and j_{CO_2} the measured CO_2 production rate (mol s^{-1}). P_{H_2} is included in the calculations to compensate for possible small H_2 gas leakage in practice. Note that we assumed the H_2 production at the cathode fully compensates the H_2 requirement at the anode in optimized cell designs (i.e., gas-tight).

The primary purpose of the system is to regenerate the alkaline absorbent. As the maximum total carbon concentration in the spent absorbent is determined by the CO_2 partial pressure in the air, the regenerated CO_2 capture capacity of the absorbent equals the amount of

total carbon been removed during the regeneration. The total carbon removed during the regeneration is in the form of desorption of CO_2(g). Therefore, we define a "carbon removal efficiency" ($\xi_{removal}$) to quantify the efficiency of the absorbent regeneration step, and it is expressed as

$$\xi_{removal} = 1 - \frac{c_{t,2}}{c_{t,0}} \tag{2.8}$$

Where $c_{t,2}$ and $c_{t,0}$ are the total carbon concentration in the cathode outlet and influent, respectively (mol m^{-3}).

Finally, we describe the potential drop over the cell as a sum of equilibrium potential (V_{eq}), anode overpotential (η_{anode}), cathode overpotential ($\eta_{cathode}$), ionic losses (V_{ionic}), and transport losses ($V_{transport}$). Further details on the calculations can be found in the Supporting Information.

2.2.2. Equilibrium model

An equilibrium model was developed for the acidifying and cathode compartments, based on mass balance and transport equations of Na^+ and H^+. The model considers steady-state conditions, well-mixed compartments, and ideal CEM behavior (i.e., a complete rejection of co-ions). The anode was excluded from this framework to simplify the system. Hence, we also assume that protons are produced in the acidifying compartment and consumed at the cathode (i.e., assuming hydrogen evolution from protons instead of from water). Furthermore, the recirculation of each compartment is not considered in the model, and the outlet from the acidifying compartment flows directly to the cathode.

Neglecting any net transport of water through the membrane, the mass balance for sodium in the acidifying compartment can be written as

$$J_{Na^+} = \frac{Q}{A} (c_{Na^+,0} - c_{Na^+,1}) \tag{2.9}$$

Where J_{Na^+} is the molar flux of Na^+ through the CEM, and $c_{Na^+,0}$ and $c_{Na^+,1}$ the Na^+ concentration at the inlet and outlet of acidifying compartment.

The mass balance of total carbon species is related to the CO_2 production in the acidifying compartment. The total carbon concentration in the anode outflow ($c_{t,1}$) in equilibrium with the gas phase in the membrane contactor (1 atm pure CO_2), so it is a function of sodium concentration ($c_{Na^+,1}$) and CO_2 partial pressure. If $c_{t,1}$ is lower than the total carbon concentration in the anode inflow ($c_{t,0}$), the reduction of total carbon in the liquid phase is desorbed into the gas phase as CO_2 gas. Therefore, the specific CO_2 production rate (J_{CO_2}) can be defined as

$$J_{CO_2} = \frac{Q}{A} (c_{t,0} - c_{t,1}) \tag{2.10}$$

Note that the J_{CO_2} is normalized for the active area of the cell. If $c_{t,1}$ is calculated to be higher than $c_{t,0}$, we consider the acidifying compartment as a closed system which has no gas production and $c_{t,1} = c_{t,0}$.

In the cathode compartment, since ideally no carbon species can pass through the membrane, the total concentration of carbon species remains constant, i.e., $c_{t,2} = c_{t,1}$ and $c_{Na^+,2} = c_{Na^+,0}$, where subscript '2' indicates the cathode outlet.

The total ionic current through the CEM is given by

$$j_c = J_{Na^+} + J_{H^+} \tag{2.11}$$

Where J_{H^+} is the molar flux of H^+ through the membrane. Both cation fluxes can be calculated by considering the Nernst-Planck equation. The electroneutrality condition inside the CEM gives

$$c_{Na^+} + c_{H^+} = c_X \tag{2.12}$$

Where c_X is the fixed charge density of the cation exchange membrane. Therefore, the Nernst-Planck equation for J_{Na^+} and J_{H^+} can be rewritten as

$$J_{Na^+} = -D\ c_X \left(\frac{df_{Na^+}}{dx} + f_{Na^+}\frac{d\phi}{dx}\right) \tag{2.13}$$

$$J_{H^+} = -a\ D\ c_X \left(\frac{df_{H^+}}{dx} + f_{H^+}\frac{d\phi}{dx}\right) \tag{2.14}$$

Where D is the diffusion coefficient of Na^+ inside the membrane, a the ratio between the diffusion coefficient of H^+ and Na^+, ϕ the electric potential, x the position inside the membrane, and f_{Na^+} and f_{H^+} are the concentration fraction of Na^+ and H^+ respectively ($f_{Na^+} = c_{Na^+}/c_X$, $f_{H^+} = c_{H^+}/c_X$).

The ion concentration in the bulk solution is the same as the ion concentration on the membrane surface since we assumed perfectly stirred compartments (i.e., no concentration polarization phenomena). By combining eqs. 2.13 and 2.14 into eq. 2.11, the total ionic current is equal to

$$j_c = -D\ \frac{c_X}{\delta}\left\{(a-1)\left(f_{H^+,c} - f_{H^+,a}\right) + \left[1 + (a-1)\ \frac{f_{H^+,c}+f_{H^+,a}}{2}\right] d\phi\right\} \tag{2.15}$$

Where δ is the CEM thickness and subscripts a and c indicate the acidifying and cathode sides of the membrane respectively. Furthermore, the transport number of Na^+ (t_{Na^+}) is defined as

$$t_{Na^+} = \frac{J_{Na^+}}{j_c} \tag{2.16}$$

Finally, the specific energy consumption (EC^0) is calculated by

$$EC^0 = \frac{V_{total}\, j_c}{J_{CO_2}} \tag{2.17}$$

Where V_{total} is the total cell voltage, which is calculated as the sum of ohmic losses (V_{ohmic}), potential drop due to the pH difference in the cell (V_{pH}), and membrane potential ($V_{membrane}$).

$$V_{total} = V_{ohmic} + V_{pH} + V_{membrane} \tag{2.18}$$

The V_{ohmic} is the potential loss related to the ohmic resistance of the acidifying and cathode compartments and can be expressed as

$$V_{ohmic} = j_c \left(\frac{d_a}{\sigma_a} + \frac{d_c}{\sigma_c}\right) \tag{2.19}$$

Where d_a and d_c are the thickness of acidifying and cathode compartments respectively, σ_a and σ_c are the conductivity of acidifying solution and catholyte (calculated by OLIStudio version 9.5 (OLI Systems, Inc., NJ, USA) based on the solution composition).

The V_{pH} is determined by the pH difference between anode and cathode considering a potential drop of 59.2 mV per pH unit, and pH_{anode} = 1 due to the high proton concentration in the MEA:

$$V_{pH} = 0.0592\ (pH_{cathode} - 1) \tag{2.20}$$

The $V_{membrane}$ is the Donnan potential across the CEM and is determined by the sodium concentration on each side of the membrane:

$$V_{membrane} = \frac{R\,T}{F}\ ln\frac{c_{Na^+,2}}{c_{Na^+,1}} \tag{2.21}$$

The model requires as input the properties of the influent (i.e., $c_{Na^+,0}$, $c_{t,0}$, and Q), and the Na^+ concentration of the outlet acidifying solution ($c_{Na^+,1}$), and then calculates the current density, Na^+ load ratio, CO_2 production rate, and outlet concentration as output.

2.3. Results and discussion

2.3.1. Effect of Na^+ load ratio

We first tested the cell under constant current operations and investigated the effect of the Na^+ load ratio (L_{Na^+}) by varying the influent flow rate. **Figure 2.2** shows both the experimental and theoretical results obtained with L_{Na^+} ranging from 0.2 to 1.2 at a constant current density (150 A m^{-2}).

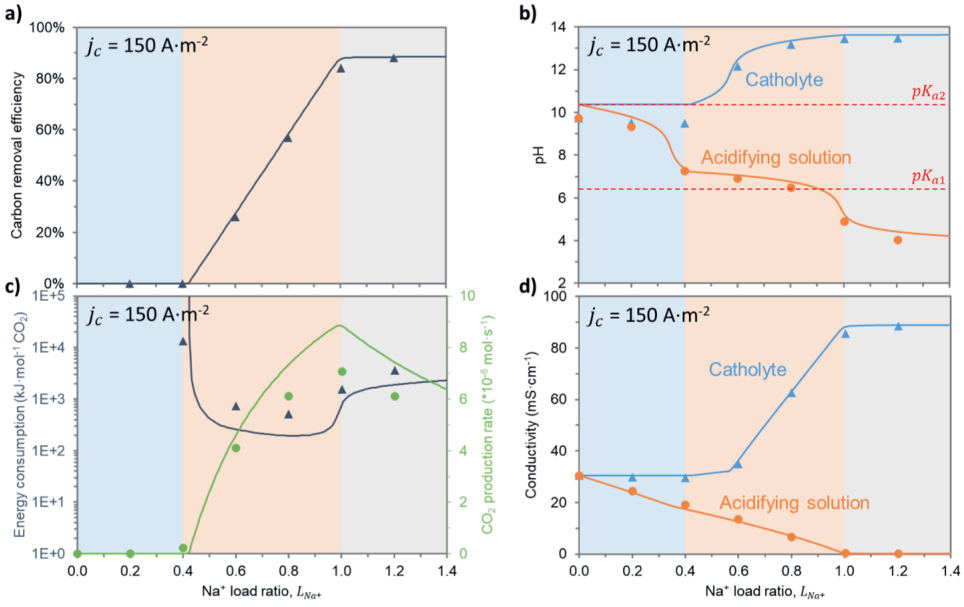

Figure 2.2. Effect of Na$^+$ load ratio on the cell performance at a constant current density (150 A m^{-2}). a) carbon removal efficiency, b) pH, c) specific energy consumption and CO_2 production rate, d) electrical conductivity. Symbols (●▲): experimental data; lines: model results.

The carbon removal efficiency as a function of the load ratio clearly shows three different regimes (**Figure 2.2**a), i.e., (i) $L_{Na^+} < 0.4$; (ii) $L_{Na^+} = 0.4$-1, and (iii) $L_{Na^+} > 1$. For $L_{Na^+} < 0.4$, no carbon removal is observed. Based on the CO_2 equilibria shown in eqs. 2.2 – 2.4, we calculated that CO_2 can only be desorbed into the gas phase when the pH is lower than 7.3 (i.e., assuming that the acidifying solution is in equilibrium with 1 atm pure CO_2 in the gas phase of the membrane contactor). In fact, in this regime at $L_{Na^+} < 0.4$, the pH of the acidifying solution is higher than 7.3 (**Figure 2.2**b). Consequently, the CO_2 production rate is zero (**Figure 2.2**c). The invested energy is, however, essential for achieving the suitable pH conditions to desorb CO_2 at higher L_{Na^+}. The reason is that the H^+ produced in this first regime is used to convert CO_3^{2-} to HCO_3^- and a small amount of $H_2CO_3^*$ so that the further accumulation of $H_2CO_3^*$ can lead to CO_2 desorption. Lastly, **Figure 2.2**d shows a linear decrease of the electrical conductivity of the acidifying solution, since Na^+ is transported to the cathode and CO_3^{2-}/HCO_3^- are neutralized by H^+. Meanwhile, the electrical conductivity of catholyte is constant corresponding to the constant pH shown in **Figure 2.2**b because the solution reverts to the composition of the influent of the cell (i.e., the change caused by H^+ produced at the anode is neutralized by the OH^- produced at the cathode).

In the second regime at L_{Na^+} between 0.4 and 1.0, the carbon removal efficiency and CO_2 production rate increase with L_{Na^+} due to the lower pH in the acidifying compartment, showing that the carbon species in the spent solution are removed as desorbed CO_2. Besides, the conductivity of the acidifying solution keeps decreasing as a higher amount of Na^+ is

transported to the cathode and CO_3^{2-}/HCO_3^- are neutralized by H^+. Due to the decrease of ionic conductivity of the acidifying solution, the ohmic resistance of the cell increases with the load ratio. As a result of the tradeoff between the increasing CO_2 production rate and the increasing ohmic resistance, we experimentally reached a minimum specific energy consumption of 520 kJ mol^{-1} CO_2 at $L_{Na^+} = 0.8$ and $j_c = 150$ A m^{-2}.

In the third regime at $L_{Na^+} > 1.0$, the carbon removal efficiency reaches a plateau, and the CO_2 production rate starts to decrease after it reaches a maximum at $L_{Na^+} = 1.0$. By definition, $L_{Na^+} > 1.0$ implies that the applied current is sufficient to transport all the Na^+ from the acidifying compartment to the cathode compartment. As a result, the pH of the acidifying solution is so low that most of the carbon species in the aqueous solution are in the form of $H_2CO_3^*$. Therefore, the carbon removal efficiency is mostly limited by the CO_2 partial pressure in the gas phase of the membrane contactor which is constant at 1 atm. Moreover, the CO_2 production is limited by the amount of total carbon feeding into the system and not by the pH of the acidifying solution. The CO_2 production rate decreases at $L_{Na^+} > 1.0$, since less influent and hence less total carbon is supplied than at $L_{Na^+} < 1.0$. Furthermore, the transport number of Na^+ decreases at $L_{Na^+} > 1.0$ (**Figure S2.1**), some H^+ ions in the acidifying solution are transported through the CEM rather than contributing to the CO_2 desorption, as shown by the decreasing CO_2 production rate in the last regime. Lastly, the conductivity in the acidifying compartment is as low as 0.43 mS cm^{-1} ($L_{Na^+} = 1.0$) and 0.08 mS cm^{-1} ($L_{Na^+} = 1.2$). As a result, the ohmic resistance in the compartment significantly increases in this regime leading to high energy consumption.

The carbon removal efficiency shown in **Figure 2.2**a also indicates the regeneration efficiency of the CO_2 capture capacity of the absorbent. At $L_{Na^+} = 0.8$, $\xi_{removal} = 57\%$ implies 57% of the CO_2 capture capacity of the absorbent is regenerated. The outlet catholyte reaches a pH = 13.19 and a conductivity of 62.58 mS cm^{-1}, which leads to a final composition of 0.22 M NaOH and 0.14 M Na_2CO_3 (calculated by OLIStudio based on measured conductivity). Given this OH^-/CO_3^{2-} molar ratio, we believe that such a solution can be directly reused as an absorbent for DAC. In comparison, Keith et al. used an aqueous solution of 1.0 M KOH, 0.5 M K_2CO_3 as an absorbent in their DAC pilot plant that has a very close OH^-/CO_3^{2-} molar ratio as our regenerated absorbent.[45]

Furthermore, **Figure 2.2** also shows a good agreement between the model simulations and experimental data. In particular, the model predicts the same trend for carbon removal efficiency, pH, and conductivity (**Figure 2.2**a, b, d), thus proving the validity of the mass balance calculations in the system. Regarding the CO_2 production rate (**Figure 2.2**c), the model overestimates by 12% to 20% the experimental results, likely due to some CO_2 leakage occurring in the experimental setup. The residence time of the solution in the system increases at higher load ratio due to lower influent flow rate, so the risk of gas leakage also increases. Despite the overestimation by the model, the simulation results correctly predict a

maximum for CO_2 production rate at $L_{Na^+} = 1.0$, where the limiting factor for CO_2 desorption shifts from the solution pH to the amount of carbon available in the bulk solution.

Regarding the energy consumption, the model correctly predicts the experimental trend, but it gives lower values compared to experimental data (**Figure 2.2**c). Such difference can be due to some of the simplifying assumptions, i.e., the absence of gas leakage (CO_2 and H_2), and of electrode overpotentials. In particular, the model predicts a minimum energy consumption of 195 kJ mol^{-1} CO_2 and carbon removal efficiency of 59% at $L_{Na^+} = 0.8$. We believe that these predicted values by the model can be experimentally achieved by further optimization of the system (i.e., minimizing the gas leakage and electrode overpotentials).

2.3.2. Effect of current density at a constant load ratio

The tests at different Na^+ load ratio showed the lowest energy consumption for the system is achieved at $L_{Na^+} = 0.8$. To further study the effect of current density on the energy consumption, we performed experiments with current density ranging from 25 A m^{-2} to 150 A m^{-2} at a fixed load ratio. During the tests, the influent flow rate was modified in line with the current density to maintain a constant L_{Na^+} of 0.8. Experimental and theoretical results are shown in **Figure 2.3**.

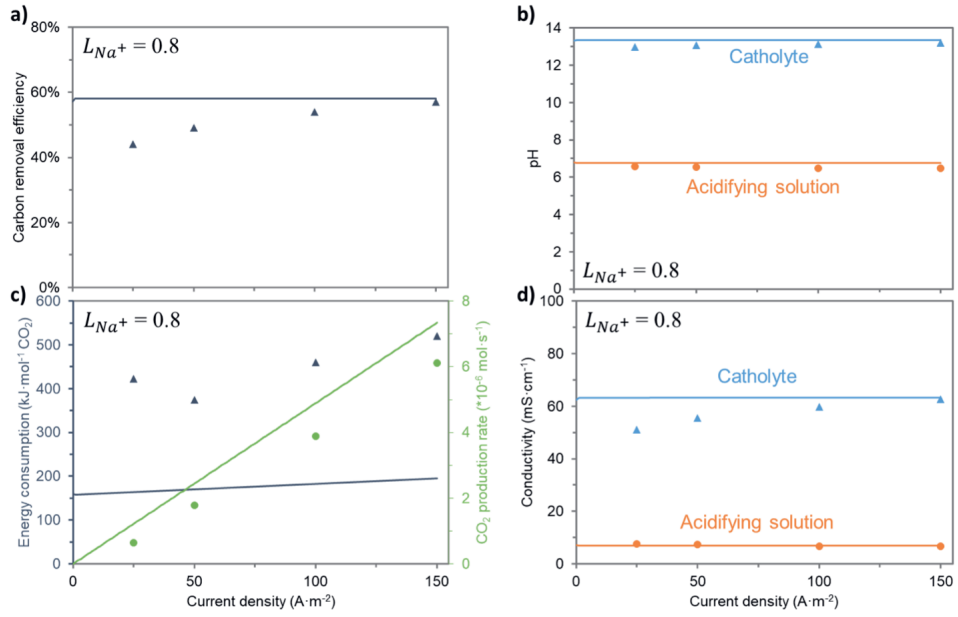

Figure 2.3. Effect of current density and flow rate at constant Na^+ load ratio. a) pH, b) CO_2 production rate, c) specific energy consumption and CO_2 production rate, d) electrical conductivity. Symbols (●▲): experimental data; lines: model results.

As the model has been validated in previous section for prediction of carbon removal efficiency, pH, and conductivity, we believe the simulations also predict the behavior of these parameters at different current densities correctly. **Figure 2.3**a shows the carbon removal efficiency remains constant with the change of current density due to an identical steady-state obtained at the same value of L_{Na^+}. This identical steady-state is also demonstrated by the constant pH and conductivity (**Figure 2.3**b, d). The CO_2 production rate increases linearly with the current density due to the higher flux of H^+ from the anode and higher total carbon loading, as a result of the increasing influent flow rate (**Figure 2.3**c).

Nevertheless, we also noticed differences between the simulation and experimental results. In particular, the difference in carbon removal efficiency, conductivity of catholyte, and CO_2 production rate which can be explained by the leakage of carbon species from the system and inside the system. The tests at lower current density have a lower influent flow rate, which leads to longer residence time and larger gas leakage. Furthermore, the neutral carbon species ($H_2CO_3^*$), instead of being desorbed as CO_2(g), can be transported from the acidifying compartment to the cathode compartment under a concentration gradient.[96] Once in the cathode compartment, the $H_2CO_3^*$ can react with OH^- in the catholyte to produce CO_3^{2-}, thus decreasing the ionic conductivity (since CO_3^{2-} has a lower ion conductivity than OH^-). Therefore, the longer residence time at low current density tests increases the leakage of carbon species.

Such leakage is also visible in the increased energy consumption in the test at j_c = 25 A m^{-2} (**Figure 2.3**c). With lower current density, we expected lower energy consumption due to minor energy losses from the internal resistance and overpotential, which is in agreement with the tests at 50-150 A m^{-2}. However, we observed a higher energy consumption at j_c = 25 A m^{-2} compared to the test at j_c = 50 A m^{-2}. As shown by the similar difference between simulation and experimental results of the CO_2 production rate, the leakage of CO_2 is at a constant rate. Thus, the leakage has a greater impact on the energy consumption at lower current density since the fraction of CO_2 leaked from the system is larger. The modeling results identify the importance of minimizing the leakage and thus directly point to the need of improving the gas-tightness of the setup in future studies.

We achieved the lowest energy consumption of 374 kJ mol^{-1} CO_2 at a current density of 50 A m^{-2}. In that case, the outlet solution from the cathode compartment reached a pH = 13.07, and final composition of 0.167 M NaOH and 0.1665M Na_2CO_3, corresponding to a 49% carbon removal efficiency. In addition, the gas desorbed from the membrane contactor contains more than 95% of CO_2 in the test at j_c = 50 A m^{-2}. This high purity CO_2 gas is suitable for subsequent storage or utilization.[29] Without the leakage of CO_2, as predicted by the model, the specific energy consumption increases gradually with the current density (**Figure 2.3**c). At j_c = 25 A m^{-2}, a specific energy consumption of 164 kJ mol^{-1} CO_2 is predicted, which represents the lowest value of energy consumption for our system in the investigated

operational range. Such an operating condition results in a 58% carbon removal efficiency and with a final solution composition suitable for use as a DAC absorbent.

The energy consumption experimentally measured is higher than the theoretical values (**Figure 2.3**d). To investigate this difference, we analyzed the potential losses in the cell at different current densities. **Figure 2.4** shows the contribution of the potential drops to the cell voltage during the tests shown in **Figure 2.3**. At low current density, the cell voltage is clearly dominated by the equilibrium potential (V_{eq}) (75% of V_{cell} at 25 A m^{-2}), while its contribution to the cell voltage decreases at higher current density (38% of V_{cell} at 150 A m^{-2}). The value of V_{eq} is independent of the applied current density due to the constant pH difference between anode and cathode (at constant Na^+ load ratio). However, all other potential losses increase by increasing the current density. The overpotential of the anode (η_{anode}) and the cathode ($\eta_{cathode}$) reach their highest contribution at j_c = 150 A m^{-2}, 28% and 13% of the cell voltage, respectively. The Donnan potential given by the CEM of the MEA was included as part of the anode overpotential, thus the current density has a larger effect on η_{anode}. Moreover, the transport losses ($V_{transport}$) increase with current density until reaching 20% of the cell voltage at 150 A m^{-2}. In this context, the $V_{transport}$ refers to the remaining losses in the system, such as the losses caused by the formation of gas bubbles both in the acidifying compartment (CO_2) and in the cathode (H_2). Finally, the ionic losses due to the ohmic resistance of the solution (V_{ionic}) are negligible, due to the high ionic conductivity at L_{Na^+} = 0.8.

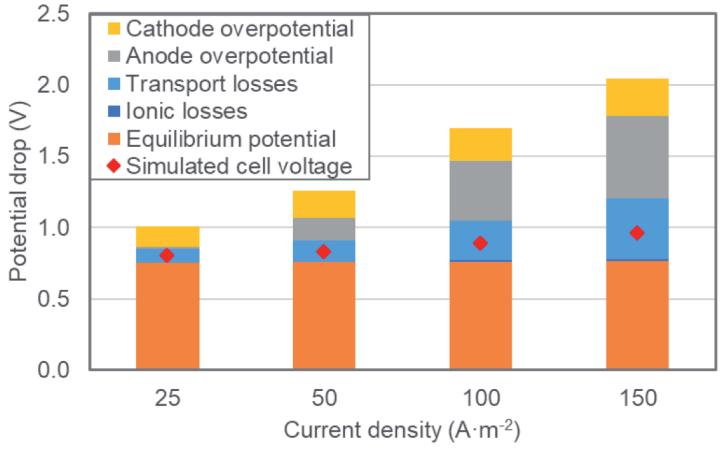

Figure 2.4. Relative contributions of potential drops in the system at different current densities and constant Na^+ load ratio (L_{Na^+} = 0.8). Symbol (♦) represents the cell voltage predicted by the model.

The model captures the equilibrium potential, the ionic losses, and the membrane potential (as a part of the transport losses). This part of potential losses remains stable with the increase of current density, while the remaining losses increase dramatically. Therefore,

although the model predicted 80% of the total potential drop at 25 A m^{-2}, only 48% is predicted when the current density rises to 150 A m^{-2}. The difference is mainly due to the overpotential of the electrodes and other nonideal losses, which could be contributed by reaction kinetics, boundary layers, and bubble formation.[55,61] The deviation between the modeling results and experimental data indicates that further refinement of the model and measurements is needed to identify the contribution of each of these processes and propose improved designs. On a cell design level, future research efforts should be focused on reducing gas leakage. Moreover, different electrode materials could be tested to reduce the electrode overpotential, for instance, by using different membrane-electrode assemblies or highly electroactive materials for hydrogen evolution. Finally, further studies should be focused on optimizing the electrolyte compositions, aiming to decrease the transport losses in the system and provide more insights on the reaction kinetics.

The proposed H_2-recycling electrochemical system shows capable of regenerating the spent alkaline absorbent from DAC and producing a high-purity CO_2 gas stream. We experimentally achieved a minimum energy consumption of 374 kJ mol^{-1} CO_2, while the model simulation has shown the energy consumption of the system can be as low as 164 kJ mol^{-1} CO_2 by further optimization. Such low energy consumption values are in line with other regeneration strategies proposed for DAC, thus showing that this electrochemical process can be a competitive alternative among all DAC technologies. For instance, Keith et al. showed energy consumption of 338 kJ mol^{-1} CO_2 for their thermodynamic cycle,[45] while Sabatino et al, estimated an energy consumption of 236 kJ mol^{-1} CO_2 for bipolar membrane electrodialysis.[59] Besides, up to 59% of the CO_2 capture capacity of the absorbent could be regenerated during the process, which made the effluent from the system suitable for DAC systems. Furthermore, another advantage of such an electrochemical system for CO_2 desorption is that it does not require any heat for the absorbent regeneration (unlike most of the proposed DAC technologies[45,97]). Instead, it requires only electricity as energy input, so it can be easily coupled to renewable energy sources for a sustainable DAC process. Finally, the desorption of CO_2 and regeneration of alkaline absorbent occurring in one step represents a clear advantage for the reduction of the overall operational costs, since it simplifies the process operation compared to energy-intensive processes such as causticization.[85]

Supporting information

List of experiments

Table S2.1 lists all the experiments been performed.

Table S2.1. List of investigated experimental conditions.

Test condition	Current density (A m^{-2})	Influent flow rate (mL min^{-1})	L_{Na^+}
Constant current	150	9.3	0.2
	150	4.7	0.4
	150	3.1	0.6
	150	2.3	0.8
	150	1.9	1.0
	150	1.6	1.2
Constant L_{Na^+}	100	1.6	0.8
	50	0.8	0.8
	25	0.4	0.8

Potential drops calculations

The cell voltage (V_{cell}) of the electrochemical system consists of equilibrium potential (V_{eq}), anode overpotential (η_{anode}), cathode overpotential ($\eta_{cathode}$), ionic losses (V_{ionic}), transport losses ($V_{transport}$):

$$V_{cell} = V_{eq} + \eta_{anode} + \eta_{cathode} + V_{ionic} + V_{transport} \quad \text{(S2.1)}$$

V_{eq} was determined by the pH difference between anode and cathode considering a potential drop of 59.2 mV per pH unit:

$$V_{eq} = 0.0592\ (pH_{cathode} - pH_{anode}) \quad \text{(S2.2)}$$

Where $pH_{cathode}$ is the measured pH of catholyte, and pH_{anode} is the pH in the anode which we assumed to be 0.27 based on $[H^+]$ = 0.54 M for fully saturated Nafion membrane.[98] The pH_{anode} is different from the value we used in the model, where pH_{anode} = 1. These different assumptions give a potential difference of 0.04 V, which is only 5% of the equilibrium potential, we believe it is negligible.

η_{anode} was determined by the difference between measured anode potential ($V_{anode,measured}$) and the calculated anode potential (V_{anode}) based on actual conditions:

$$\eta_{anode} = V_{anode,measured} - V_{anode} \quad \text{(S2.3)}$$

$$V_{anode} = V^0_{anode} - \frac{R\,T}{z\,F} \ln\left(\frac{pH_2}{[H^+]^2}\right) \quad \text{(S2.4)}$$

Where V^0_{anode} is the standard anode potential (-0.21 V vs Ag/AgCl), pH_2 is the hydrogen partial pressure at anode (0.95 atm, considering 5% CO_2 leaked from acidifying compartment), and $[H^+]$ equals to 0.54 M as stated before.

$\eta_{cathode}$ was determined by the difference between the calculated cathode potential ($V_{cathode}$) based on actual conditions and measured cathode potential ($V_{cathode,measured}$):

$$\eta_{cathode} = V_{cathode} - V_{cathode,measured} \quad \text{(S2.5)}$$

$$V_{cathode} = V^0_{cathode} - \frac{R\,T}{z\,F} \ln\left(pH_2\,[OH^-]^2\right) \quad \text{(S2.6)}$$

Where $V^0_{cathode}$is the standard cathode potential (-1.028 V vs Ag/AgCl), pH_2 is the hydrogen partial pressure at cathode (1 atm), and $[OH^-]$ is the concentration of OH^- in catholyte calculated from measured pH (M).

V_{ionic} was determined by the measured conductivity in the acidifying and cathode compartments:

$$V_{ionic} = i\,A\left(\frac{d_a}{A\,\sigma_a} + \frac{d_c}{A\,\sigma_c}\right) \quad \text{(S2.7)}$$

Where d_a and d_c are the thickness of the acidifying and cathode compartment respectively (0.05 cm), σ_a and σ_c are the conductivity in these two compartments (mS cm^{-1}).

$V_{transport}$ was calculated based on eq. S2.1 and the measured cell voltage.

Transport number of Na^+

The transport number of Na^+ in the CEM is calculated as following:

$$t_{Na^+} = \frac{\Delta C_{Na^+}\, z_{Na^+}\, F\, Q\, HRT}{M_{Na^+}\, j_c\, HRT\, A} \quad \text{(S2.8)}$$

Where ΔC_{Na^+} is the concentration difference of Na^+ in the acidifying and cathode compartments (g L^{-1}), z_{Na^+} is the net charge of Na^+ which is 1, F is the Faraday constant (96485 C mol^{-1}), Q is the influent flow rate (L s^{-1}), HRT is the hydraulic retention time (s), M_{Na^+} is the molar mass of Na^+ (g mol^{-1}), j_c is the applied current density (A m^{-2}), and A is the surface of area of the CEM (0.01 m^2).

The t_{Na^+} indicates the fraction of current been carried by Na^+ transport over the CEM. The maximum value of t_{Na^+} is 1.0 which implies that all the current applied is carried by Na^+. As discussed in the main text, the CO_2 production was highly corelated to Na^+ transport.

Thus, in order to achieve a higher CO_2 production rate, t_{Na+} requires to be maintained at high value. As shown in **Figure S2.1**, t_{Na+} constantly remains around 1.0 at L_{Na+} = 0.4-1.0, while t_{Na+} drops to 0.8 at L_{Na+} = 1.2. The only cations in the system were Na^+ and H^+, so the ionic transport over CEM was in form of these two cation species. When L_{Na+} was lower than 1.0, the concentration of Na^+ was much higher than the concentration of H^+ in the acidifying compartment. Although H^+ has a higher transport coefficient, almost all the cations been transported are Na^+ due to the large concentration difference. At L_{Na+} of 1.2, the pH in the acidifying compartment was 4.04 which results in a H^+ concentration of 0.1 mM, while the concentration of Na^+ was 0.7 mM. Therefore, also H^+ was transported through the CEM, and t_{Na+} decreases. The calculation framework predicted the same trend of t_{Na+} change with different L_{Na+}. In the experiment with L_{Na+} of 0.2, we obtained a t_{Na+} of 1.1 which we believe that it was caused by a measurement error from the Na^+ concentration in acidifying compartment.

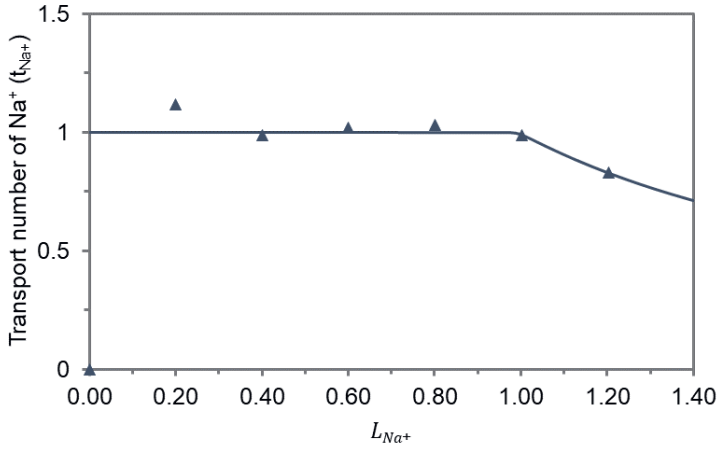

Figure S2.1. Na^+ transport number at L_{Na+} = 0 – 1.4. Symbols (▲): experimental results; lines: model results.

Additional indicators

Yield of CO_2 (Y_{CO_2}) is defined as the ratio between the CO_2 gas production and the total carbon entering the system

$$Y_{CO_2} = \frac{J_{CO_2}}{c_{t,0}\, Q} \tag{S2.9}$$

Where J_{CO_2} is the CO_2 production rate (mol s^{-1}), $c_{t,0}$ the total carbon concentration in the influent (mol m^{-3}), and Q the influent flow rate (m^3 s^{-1}).

Extraction efficiency ($Eff_{extraction}$) describes the part of carbon been removed that is desorbed to gas phase

$$Eff_{extraction} = \frac{J_{CO_2}}{(c_{t,0} - c_{t,2})\, Q} \quad \text{(S2.10)}$$

Coulombic efficiency ($Eff_{coulombic}$) is defined as the fraction of applied charge that is used to desorb CO_2 gas

$$Eff_{coulombic} = \frac{J_{CO_2}}{I/F} \quad \text{(S2.11)}$$

Where I is the applied current (A) and F is the Faraday constant (96485 C mol^{-1}).

The results of these indicators calculated from experimental data are shown in **Table S2.2**.

Table S2.2. Experimental results of yield of CO_2, carbon extraction efficiency, and coulombic efficiency.

L_{Na^+}	Current density (A m^{-2})	Yield of CO_2	Carbon extraction efficiency	Coulombic efficiency
0.2	150	0	0	0
0.4		1%	0	1%
0.6		24%	95%	26%
0.8		48%	85%	39%
1.0		70%	83%	46%
1.2		73%	83%	39%
0.8	25	31%	70%	25%
	50	42%	87%	35%
	100	46%	86%	38%
	150	48%	85%	39%

Chapter 3

Direct air capture using electrochemically regenerated anion exchange resins

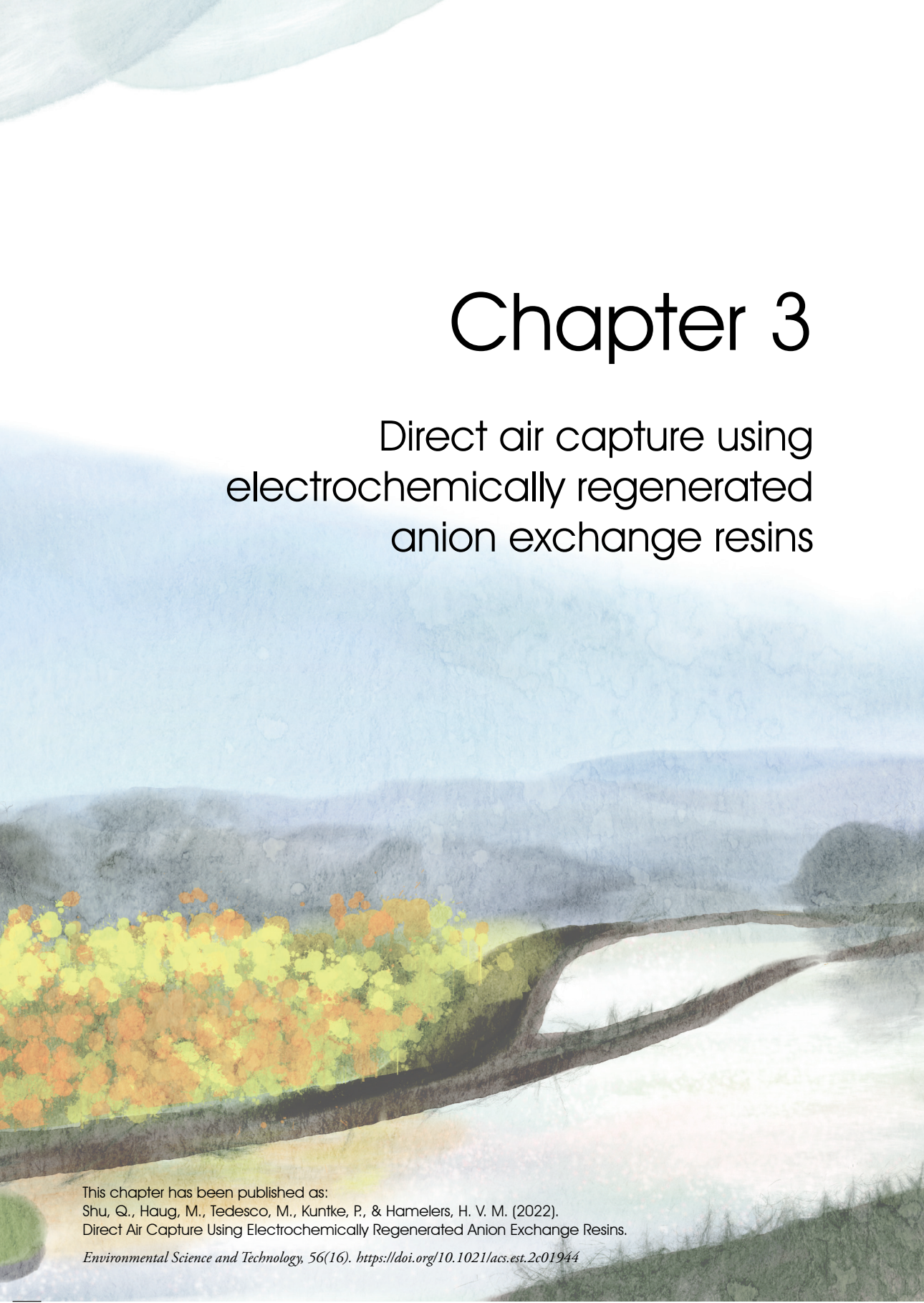

This chapter has been published as:
Shu, Q., Haug, M., Tedesco, M., Kuntke, P., & Hamelers, H. V. M. (2022).
Direct Air Capture Using Electrochemically Regenerated Anion Exchange Resins.
Environmental Science and Technology, 56(16). https://doi.org/10.1021/acs.est.2c01944

Abstract

Direct air capture (DAC) aims to remove CO_2 directly from the atmosphere. In this study, we have demonstrated proof of concept of a DAC process combining CO_2 adsorption in a packed bed of amine-functionalized anion exchange resins (AERs) with a pH swing regeneration using an electrochemical cell (EC). The resin bed was regenerated using the alkaline solution produced in the cathodic compartment of the EC, while high purity CO_2 (>95%) was desorbed in the acidifying compartment. After regenerating the AERs, some alkaline solution remained on the surface of the resins and provided additional CO_2 capture capacity during adsorption. The highest CO_2 capture capacity measured was 1.76 mmol g^{-1} dry resins. Moreover, as the whole process was operated at room temperature, the resins did not show any apparent degradation after 150 cycles of adsorption-desorption. Furthermore, when the relative humidity of the air source increased from 33% to 84%, the water loss of the process decreased by 63% while CO_2 capture capacity fell 22%. Finally, although the pressure drop of the adsorption column (5±1 kPa) and the energy consumption of the EC (537 ± 33 kJ mol^{-1} at 20 mA cm^{-2}) are high, we have discussed the potential improvements towards a successful upscaling.

3.1. Introduction

The atmospheric carbon dioxide (CO_2) concentration has increased by nearly 50% compared to preindustrial levels.[99] This increase is primarily ascribed to anthropogenic activities and has caused rapid climate change in recent years.[72,73,100,101] Several carbon capture and storage (CCS) technologies have been proposed and implemented to reduce CO_2 emissions from point sources.[28,29,102] Moreover, carbon dioxide removal (CDR), aiming to remove CO_2 already in the atmosphere, is an indispensable complement to CCS so that the 1.5°C targets from Paris Agreement can be achieved.[12,103–105] Among the proposed CDR technologies, direct air capture (DAC) has the advantages of capturing CO_2 from distributed sources and has high flexibility in its deployment location.[35,41] Despite the relatively high energy costs and materials requirement of current technologies, the development and deployment of DAC technologies are crucial for realizing the Paris Agreement climate goals.[106]

DAC with amine-based sorbents has been extensively studied.[107–110] Among these studies, amine-functionalized anion exchange resins (AERs), polymeric materials commonly used in desalination and water treatment, have been demonstrated to be eligible candidates with a high CO_2 capture capacity and low heat capacity.[111–114] Several methods have been proposed to regenerate the resins after adsorption. For instance, in a temperature swing process with (primary) amine-functionalized AERs, CO_2 from the air is adsorbed by forming carbamate species, and CO_2 is then desorbed by heating the resins during regeneration.[111] Alternatively, in a moisture swing process with (quaternary) amine-functionalized AERs, CO_2 can be adsorbed by dry resins and desorbed when the resins are wet.[114] In this case, the dry resins have hydroxide (OH^-) or carbonate (CO_3^{2-}) as counter-ions of the amine groups that combine with CO_2 to form bicarbonate (HCO_3^-). The amine groups in HCO_3^- form shift to CO_3^{2-} form and release CO_2 gas when moisture is added during the desorption step.[114] Both temperature swing and moisture swing have limitations. The resins are likely to degrade under the high temperature of desorption during temperature swing, and the process requires heat as the energy input, limiting the selection of sustainable energy sources.[115] Moisture swing is limited by the low CO_2 capture capacity with high humidity air.[116] Therefore, although amine-functionalized AERs are competent sorbents for DAC, there is room for a novel regeneration strategy that is benign for the resins and has a low energy input and CO_2 production at higher pressure.

In desalination and water treatment applications, AERs are commonly regenerated using alkaline solutions. For DAC with quaternary amine-functionalized AERs in OH^- form, HCO_3^- and CO_3^{2-} are formed during the adsorption step according to eqs. 3.1 and 3.2.[114]

$$R_4N^+OH^- + CO_2 \rightleftharpoons R_4N^+HCO_3^- \tag{3.1}$$

$$R_4N^+OH^- + R_4N^+HCO_3^- \rightleftharpoons (R_4N^+)_2CO_3^{2-} + H_2O \tag{3.2}$$

In principle, when an alkaline solution is in contact with the resins, the adsorbed HCO_3^- and CO_3^{2-} are exchanged with OH^- in solution, and the resins are regenerated. After regeneration, the resins are in OH^- form and the spent regeneration solution has a high concentration of HCO_3^- and CO_3^{2-}. Finally, a desorption process is required to desorb CO_2 from the spent regeneration solution and reproduce the alkaline solution.

Recently, we developed an electrochemical system that can regenerate spent alkaline absorbents from DAC and desorb high-purity CO_2 gas under atmospheric pressure.[117] The electrochemical system uses a pH swing to regenerate the solution in two adjacent compartments separated by a cation exchange membrane (CEM). At low pH, the CO_2 equilibria displace towards the formation of carbonic acid ($H_2CO_3^*$) due to the H^+ production at the anode. When the chemical potential of oversaturated $H_2CO_3^*$ is higher than the partial pressure of CO_2 in the gas phase, CO_2 can be desorbed. At high pH, the alkaline solution used for regenerating the resins is regenerated due to the OH^- production at the cathode.

In this work, we propose a novel process for DAC by combining the adsorption step with AERs and the regeneration step with the electrochemical system. The process operates at room temperature and only uses electricity as energy input. Moreover, the captured CO_2 is desorbed as high purity CO_2 gas at atmospheric pressure. The repeatability of the process and stability of the resins were tested by using ambient air as feed. Moreover, air with different humidity values has been investigated to show the impact of humidity on the performance of the process. Finally, we have discussed the application of the technology in terms of energy consumption and the perspectives regarding further developments.

3.2. Materials and methods

3.2.1. Experimental setup

The adsorption experiments were performed using a polyvinyl chloride (PVC) column (inner diameter of 6 cm) with a packed bed of anion exchange resins (AmberLite HPR4800 OH, Dupont, USA). The resins were first rinsed with deionized (DI) water and then immersed in 0.5 M NaOH solution for at least 3 hours to ensure that all the fixed groups were in the hydroxide form. Finally, the resins were rinsed with DI water before being air-dried at room temperature. Exactly 500 grams of dry resins were placed inside the adsorber that gives the packed bed a height of 35 cm. During the experiment, as the resins were swelling while wetted, the height of the packed bed could reach up to 55 cm.

Air was supplied into the adsorber by a vacuum pump (LABOPORT N840.1.2FT.18, KNF, Germany). The flow rate of the pump varied between 650 and 750 mL s^{-1} and was quantified by a mass flow meter (MASS-VIEW MV-306, Bronkhorst, the Netherlands). A heat exchanger/water-cooling unit was installed between the vacuum pump and the column to ensure a constant (room) temperature for inlet air into the column. Two CO_2/H_2O analyzers

(LI-850, LI-COR, USA) were used to monitor the CO_2 and H_2O concentrations in the inlet and outlet air of the column.

The regeneration of the resins was achieved via an electrochemical cell directly connected with the adsorber (**Figure 3.1**). The regeneration solution was recirculated between the column and the cell with two pumps (SIMDOS 10, KNF, Germany) at a flow rate of 0.052 mL s^{-1}. The design and materials of the electrochemical cell have been described in detail in our previous work.[117] The anode is a membrane electrode assembly (MEA) (FuelCellsEtc, TX) that comprises a platinum-coated (0.5 mg Pt cm^{-1}) gas diffusion layer (GDL) (10 cm × 10 cm) and a Nafion N117 cation exchange membrane (CEM) (15 cm × 15 cm). During operation, H_2 gas flows into the anode compartment, where it is oxidized to H^+ on the surface of the GDL. The produced H^+ migrates through the CEM towards the acidifying compartment that is separated from the cathode compartment by another CEM (Nafion N117, FuelCellEtc, USA). The flow channels of the acidifying and cathode compartments are created by two polymeric (nitrile) spacers (5×10^{-4} cm, Sefar, Switzerland). A Ru/Ir-coated titanium mesh (9.8 cm × 9.8 cm, Magneto Special Anodes BV, The Netherlands) serves as the current collector for the anode, while a platinum-coated titanium mesh (9.8 cm × 9.8 cm, Magneto Special Anodes BV, The Netherlands) is used as cathode. The H_2 gas produced at the cathode can be recirculated to the anode to compensate for the H_2 consumption, thus operating the cell in an H_2-closed loop. However, in this study, we have used an external electrolysis cell to supply the required H_2 at the anode to simplify the operation of the experimental setup for practical purposes. We do not expect any major change in performance of the system when hydrogen is recycled from cathode to anode as has been demonstrated by Kuntke et al.[91] During the operation, the spent regeneration solution was pumped into the acidifying compartment, while the effluent catholyte was recirculated back into the adsorber as the regeneration solution. The conductivities of the spent regeneration solution, acidifying solution, and catholyte were measured by three inline conductivity sensors (Memosens CLS82D, Endress+Hause, the Netherlands). The pH of the acidifying solution was measured by a pH sensor (Orbisint CPS11D, Endress+Hauser, the Netherlands). Due to the inaccuracy of the pH sensor under a high pH, the pH values of the regeneration solution and the spent regeneration solution were estimated by OLI studio based on the conductivity values of the solutions. A potentiostat (IviumStat, Ivium, the Netherlands) was used to apply the current on the cell and measure the corresponding cell voltage. The gas desorption from the acidifying solution occurred in a membrane contactor (type MM 1.7 × 8.75, 3M, USA) that provided a large surface area with hollow fiber membranes. The amount of desorbed gas was quantified by a mass flow meter (EL-FLOW Prestige FG-111B, Bronkhorst, the Netherlands), while the composition of the gas was analyzed by micro gas chromatography (μ-GC) (Varian CP-4900, Agilent, USA). The surfaces of both pristine and regenerated resins were examined by scanning electron microscope (SEM) (JSM-6480LV, JEOL, Japan) coupled with energy dispersive X-Ray spectroscopy (EDX) (NORAN Systems SIX, Thermo Fisher Scientific, USA).

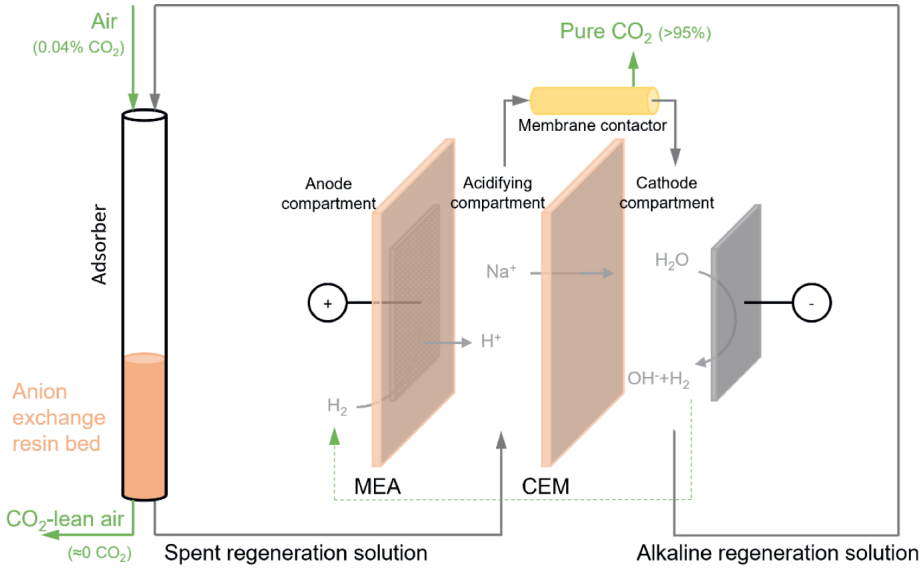

Figure 3.1. Schematic drawing of the experimental setup. Air and regeneration solution flow through the adsorber during the adsorption and desorption steps, respectively. MEA = membrane electrode assembly, CEM = cation exchange membrane.

Moreover, additional experiments were performed with a smaller amount of resins (8 g dry resins) in a smaller column to test the stability of the resins during chemical regeneration using a NaOH/Na_2CO_3 blend. The column had an inner diameter of 2.4 cm. The same vacuum pump and gas analyzers were used for the adsorption step. Each desorption step was done by using a fresh mixture of NaOH and Na_2CO_3 with a total Na^+ concentration of 0.5 M and a conductivity of 58.5 mS cm^{-1}, i.e., mimicking the regeneration solution produced in the electrochemical cell in the experiments with big column (0.192 M NaOH and 0.154 M Na_2CO_3). We have conducted 150 adsorption-desorption cycles, and the switch between adsorption and desorption step was controlled by three pivoted armature valves (one Type 0121 and two Type 0330, Bürkert, Germany) connected to a programmable logic controller (PLC) (LOGO! 230RC, Siemens, Germany). The ion exchange capacity (IEC) was quantified by a titration process (Supporting Information) for pristine and used resins after 68 cycles.

3.2.2. Experimental procedure

As the resins were air-dried before placed inside the column, they needed to be regenerated to OH^- form before the first adsorption experiment. Initially, 1.6 L of 0.5 M NaOH solution was added to the column. The solution was then recirculated between the column and the electrochemical cell. While applying a constant current of 20 mA cm^{-2} in the cell, the captured CO_2 during the air-drying step was desorbed. The pretreatment process for the resins was completed when no more CO_2 could be desorbed. Hence, the recirculation of solution and applied current were stopped. Before the first adsorption step started, the solution in the

column was pumped out to be stored in an external reservoir so that it could be reused in the next desorption step. The first adsorption experiment was performed in our laboratory to quantify the CO_2 capture capacity of the resins. The ambient conditions for this experiment were: CO_2 concentration: 394 ± 11 ppm, H_2O concentration: 13.8 ± 1.8 mmol mol^{-1}, T = 25 ± 1 °C, relative humidity (RH) = (69 ± 9)%. The following adsorption-desorption cycles were performed at two locations with different air source conditions. The first five cycles were performed using the ambient air from our laboratory: CO_2 concentration: 427 ± 7 ppm, H_2O concentration: 6.6 ± 0.9 mmol mol^{-1}, T = 25 ± 1 °C, Relative humidity (RH) = (33 ± 5)%. The last five cycles were performed outdoors with air conditions as: CO_2 concentration: 412 ± 12 ppm, H_2O concentration: 9.6 ± 1.2 mmol mol^{-1}, T = 16 ± 3 °C, RH = (84 ± 9)%. In the discussion section of the effect of humidity, "dry air" and "humid air" refer to laboratory air and outdoor air, respectively. Each adsorption step lasted for 48 hours. Before the desorption step started, the stored regeneration solution in the external reservoir was added to the column. Since the resins had been dried during the adsorption step due to water evaporation, additional deionized water was added to maintain a constant total volume of solution during each desorption experiment. The amount of DI water added varied according to the different amounts of water loss in each adsorption step. Once the stored regeneration solution and the additional DI water were added to the column, the desorption step was started by recirculating the solution and applying a constant current (20 mA cm^{-2}) to the electrochemical cell. The recirculation between the column and the electrochemical cell lasted for ~ 15 hours, and after that, the effluent from the cell was pumped into the external reservoir (instead of the column). The desorption step was accomplished when no more solution could be pumped out of the column.

Each cycle of the experiments with the smaller column consists of 40 min of adsorption, 40 min of desorption, and 5 s of drainage. After each desorption step, the drainage step was applied to remove excess solution from the column. The air source for the adsorption steps had the following conditions: average CO_2 concentration: 413 ± 23 ppm, H_2O concentration: 13.7 ± 1.6 mmol mol^{-1}, T = 25 ± 1 °C, RH = (68 ± 9)%. The change of CO_2 concentration and H_2O concentration in each cycle is reported in **Figure S3.1**.

3.3. Results and discussion

3.3.1. Electrochemical regeneration of AERs

The first adsorption experiment lasted for more than 100 hours, and it could be divided into three stages: fast adsorption, slow adsorption, and saturation (**Figure 3.2**). At the initial stage of the adsorption (first ~ 6 hours), the adsorption rate was at its maximum (0.1 mmol g^{-1} h^{-1}) as all the CO_2 in the influent air could be fully adsorbed by the resins. With the resins becoming saturated with CO_2, the adsorption rate decreased sharply. The adsorption rate was only 0.012 mmol g^{-1} h^{-1} at ~ 20 hours, and the adsorption process remained at this low rate until ~ 95 hours. Finally, after 95 hours, the resins were saturated with CO_2 as the adsorption

rate was 0. Within these three stages, the total amount of CO_2 been adsorbed was 0.88 mol. As the total dry mass of the resins in the column was 500 g, the CO_2 capture capacity of the resins was 1.76 mmol g^{-1} dry resins.

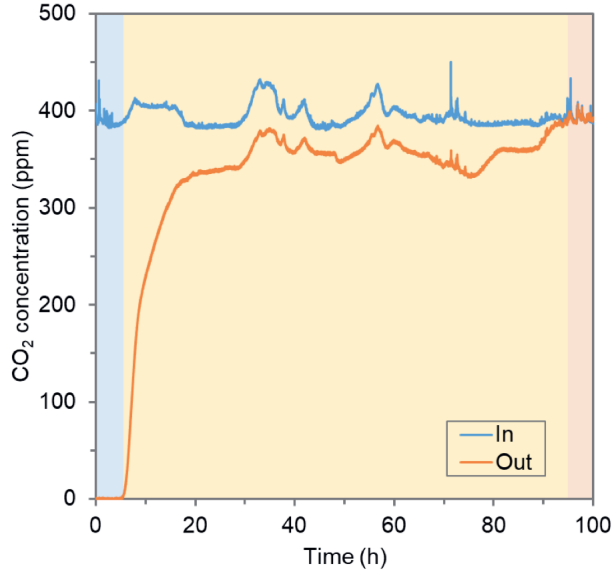

Figure 3.2. CO_2 concentration in the influent and effluent of the adsorber during the first adsorption experiment. The adsorption step can be divided into three stages based on the adsorption rate: fast adsorption (blue), slow adsorption (yellow), and saturation (orange).

Notably, such capacity is around ten times higher than what has been reported for quaternary amine-functionalized AERs.[112] Such a significant difference can be mainly attributed to different pretreatment and regeneration methods. In the work of Parvazinia et al., the AERs were heated up to 120 °C during the pretreatment and to 105 °C during the regeneration.[112] However, quaternary amine-functionalized AERs in hydroxide form are not stable under such high temperatures.[118,119] At temperatures higher than 60 °C, the occurring Hofmann degradation of the quaternary ammonium hydroxide group leads to either the loss of strong basic capacity or the loss of total ion exchange capacity.[120,121] In contrast, both adsorption and desorption steps are at room temperature in this study. Therefore, no thermal degradation of the resins can occur, and the resins maintain a high CO_2 capture capacity. Furthermore, the alkaline regeneration solution provided additional capacity for the subsequent adsorption step. Since the resins are regenerated with an alkaline solution, a thin layer of the solution remains on the surface of the resins after each regeneration step. As shown in **Figure 3.3**, the dry regenerated resins had precipitations on the surface that were identified as mainly Na, C, and O (see EDX results in SI, **Figure S3.4** and **Table S3.1**). Therefore, the residual regeneration solution (i.e., a mixture of NaOH and Na_2CO_3) provided extra capacity for CO_2 capture. We have estimated the amount of CO_2 adsorbed by the retained solution based on the

following assumptions: i) the total solution volume retained equals to the maximum water loss among all the adsorption experiments (i.e., 0.58 L), ii) the retained solution has a composition of 0.20 M NaOH and 0.15 M Na_2CO_3, iii) the alkaline solution equilibrates with 400 ppm in the air forms 0.175 M Na_2CO_3 and 0.150 M $NaHCO_3$. Based on these assumptions, the CO_2 adsorbed by the retained solution counts for 17.5% of the total CO_2 capture capacity of the resin bed. To experimentally prove this estimation, we have performed one adsorption experiment with resins rinsed by de-ionized water. Without the alkaline regeneration solution on the surface, the CO_2 capture capacity of the resins dropped by ~ 17% (**Table S3.2**), which is in line with our estimation from the retained alkaline solution and composition.

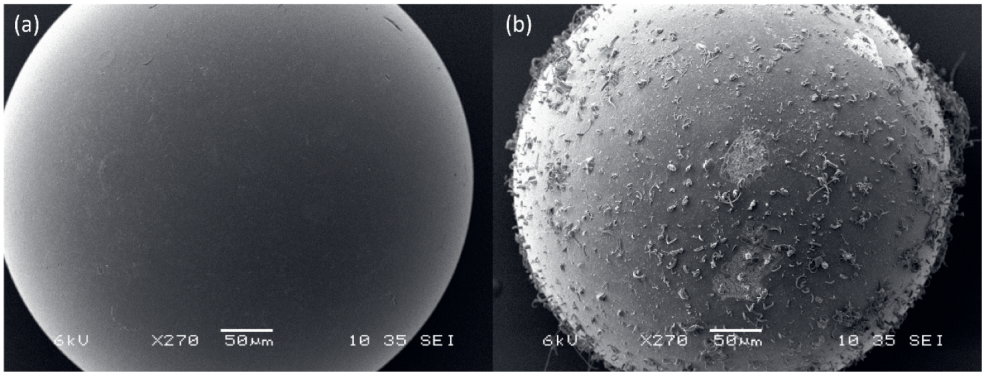

Figure 3.3. SEM images of (a) a pristine resin bead and (b) a used resin bead regenerated by the electrochemical process. The elements of the precipitation on the surface of the used resin were identified by EDX analysis as mainly Na, C, and O.

After the adsorption step, CO_2 is present on the surface of the resins in the form of CO_3^{2-} and HCO_3^-. These ions are exchanged by OH^- during the regeneration step with the alkaline regeneration solution produced in the electrochemical cell. As a result of the ion exchange process, the pH and conductivity of the solution decrease after flowing through the resin column (**Table 3.1**). The spent regeneration solution from the outlet of the column, i.e., an aqueous solution of Na_2CO_3 and $NaHCO_3$, is fed into the electrochemical cell. In the electrochemical cell, the solution is first acidified so that CO_2 can be desorbed into the gas phase. The desorbed gas was under atmospheric pressure and confirmed with μ-GC to contain more than 96% of CO_2 (detailed composition shown in **Table S3.3**). Then the OH^- produced in the hydrogen evolution reaction (HER, cathode compartment) increased the pH of the CO_2 depleted regeneration solution. The regeneration of the resins was considered completed when the conductivities of the regeneration solution at the outlet and inlet of the adsorber were equal. Meanwhile, the gas desorption rate decreased to 0 since a negligible concentration of CO_3^{2-} or HCO_3^- was present in the feed solution of the electrochemical cell (**Figure S3.6**).

Table 3.1. pH and conductivity values of regeneration solution, spent regeneration solution, and acidifying solution. All values represent the average and standard deviation of five desorption steps.

	pH	Conductivity (mS/cm)
Regeneration solution (adsorber inlet)	13.0 [a]	53.4 ± 3.6
Spent regeneration solution (adsorber outlet)	10.0 [a]	31.2 ± 1.1
Acidifying solution	6.5 ± 0.2	12.0 ± 0.7

a. Not measured due to inaccuracy of pH sensors under high pH, but estimated by OLI Studio based on the average conductivity and Na^+ concentration of the solution.

The CO_2 capture capacity of the resins was restored after they were regenerated to OH^- form. We have repeated the adsorption-desorption cycle five times using lab air. The complete DAC system showed a stable performance over five lab cycles regarding the amount of CO_2 adsorbed and desorbed (**Figure 3.4**). Instead of reaching the full CO_2 capture capacity of the resins with ~ 95 hours of adsorption, these adsorption steps were limited to 48 hours, i.e., when more than 75% of the adsorption was accomplished. The normalized amount of CO_2 adsorbed in five cycles was 1.34 ± 0.05 mmol g^{-1}, while 1.17 ± 0.08 mmol g^{-1} was desorbed. The discrepancy between the adsorption and desorption could be attributed to (i) the wetting of the resins during regeneration and/or (ii) CO_2 leakage in the setup during desorption. The resins are wetted by the regeneration solution at the beginning of a desorption step. According to Wang et al., CO_2 could be desorbed from dry quaternary amine-functionalized resins when the resins are wetted.[114] Therefore, part of the adsorbed CO_2 could escape from the adsorber before the ion exchange occurs. Moreover, a small amount of CO_2 could leak from the electrochemical system during desorption as already observed in our previous work.[117] Despite the leakage of CO_2, the resins could be sufficiently regenerated during the desorption steps as a consistent amount of adsorption was observed during consecutive adsorption steps.

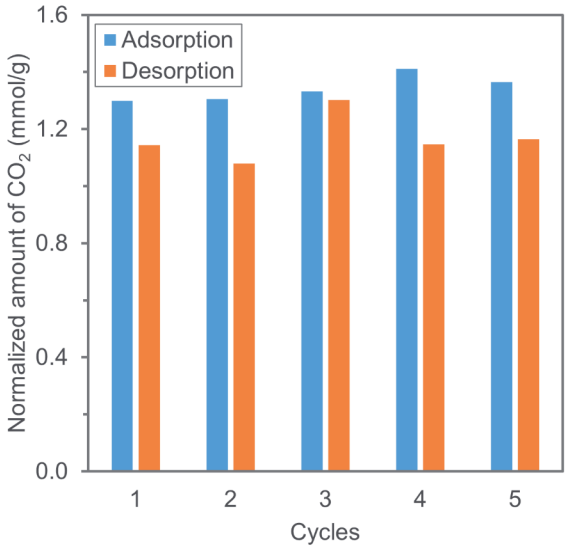

Figure 3.4. Experimental results from 5 repeated adsorption-desorption cycles showing the normalized amount of CO_2 been adsorbed and desorbed per gram of dry resins.

3.3.2. Stability of the AERs

The application of a sorbent for carbon capture requires high performance stability over long-term usage. Previous studies on the degradation of the resins used for carbon capture mainly focused on the thermal stability of the resins.[112,115] Nevertheless, the process proposed in this work is operated under ambient/room temperature, so thermal degradation is not expected. On the other hand, the stability of the resins could be affected by repeated dry-wet cycles. The exposure of AERs under dry-wet cycles can change the smoothness of the resin surface (**Figure S3.5**) and cause the desorption of ions due to the shrinking of the resin beads.[122] However, to the best of our knowledge, no evidence has been found that ion exchange capacity (IEC) of resins would change during dry-wet cycles. Therefore, 150 adsorption (dry) -desorption (wet) cycles were conducted to investigate the stability of the HPR4800 AERs for carbon capture. **Figure 3.5** has depicted the change of CO_2 adsorption amount over these 150 cycles and the according influent CO_2 concentration.

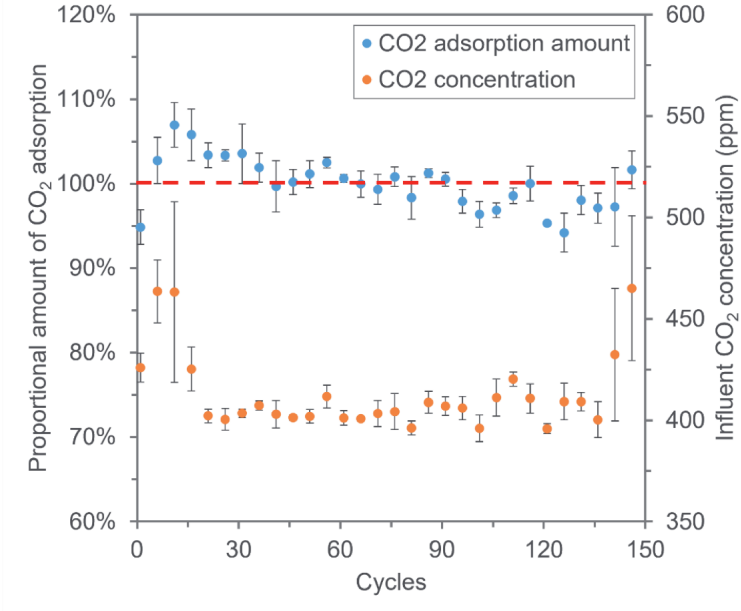

Figure 3.5. Proportional change of CO_2 adsorption amount in 150 adsorption-desorption cycles and the influent CO_2 concentration in these cycles. The average CO_2 adsorption amount of all the 150 cycles was considered as 100%, then the proportional CO_2 adsorption amount of each cycle was calculated accordingly. Symbols: average value of every five consecutive cycles; error bars: standard deviations within the five cycles.

Overall, the proportional change of CO_2 adsorption amount of the last five cycles was about 100%, which indicates no measurable loss of the resin performance. However, there was some fluctuation of the CO_2 adsorption amount over the 150 cycles. In the first 10 and the last 10 cycles, the amount of CO_2 been adsorbed increased. This increase was mainly attributed to the rise in CO_2 concentration in the influent (with a correlation coefficient between the amount of CO_2 adsorbed vs. CO_2 concentration in the influent of 0.98 and 0.84 for the first and last ten cycles, respectively). From cycle 11 to cycle 140, the amount of CO_2 been adsorbed showed a slightly decreasing trend over the cycles. Meanwhile, we have also noticed an 11% decrease in the flow rate of the air supply pump from cycle 1 to cycle 150 (**Figure S3.2**). The flow rate of the influent air can affect the amount of CO_2 adsorption from two perspectives. Firstly, as the adsorption time was kept constant in the experiments, a lower influent flow rate means a lower total amount of CO_2 fed to the resins. Secondly, a lower flow velocity in the column resulted in a higher adsorption efficiency due to less limitation from diffusion and reaction kinetics.[123] Thus, the reduction of the adsorption amount was not caused by the degradation of resins but mainly due to the slightly lower flow rate of the air supply pump over 150 cycles. We corrected the proportional change of CO_2 adsorption assuming a constant flow rate and constant CO_2 concentration in the influent, and the results are plotted in **Figure S3.3**. Finally, the CO_2 adsorption is attributed to the quaternary amine groups on the resins that could be quantified by IEC. The IEC of the pristine resins was 1.85

± 0.01 meq g^{-1}, while the IEC remained constant to be 1.86 ± 0.06 meq g^{-1} after 68 cycles. Therefore, regardless of the impact of influent CO_2 concentration and air flow rate, the resins showed stable adsorption performance.

3.3.3. Effect of air humidity

After the regeneration step, the resins are swelled (water retention capacity: 58% - 74%) and surrounded by alkaline solutions. As stated before, one of the advantages of regenerating the resins with an alkaline solution is that the remaining NaOH and Na_2CO_3 on the surface of the resins provide extra capacity for CO_2 capture. However, the water on the surface of the resins and inside the resins evaporates during adsorption when air flows through the resins. The total amount of water evaporated during the adsorption step is counted as water loss of the process and needs to be compensated by adding the corresponding amount of deionized water before the regeneration step. Since water evaporation is influenced by the humidity of the air, we have performed adsorption tests with influent air under different humidity conditions, calculating the water loss during adsorption based on the concentration difference of H_2O in the inlet/outlet air of the adsorber. The comparison between the performance of the system with dry air and humid air is shown in **Table 3.2**.

Table 3.2. Comparison of the amount of CO_2 adsorption and specific water loss between adsorption experiments using dry air (RH=33%) and humid air (RH=84%). All values represent the average and standard deviation of five adsorption-desorption cycles using different sources of air.

	Dry air	Humid air
CO_2 adsorption (mmol CO_2/g dry resins)	1.34 ± 0.05	1.04 ± 0.04
Water loss (g H_2O/g CO_2)	18.01 ± 1.59	6.65 ± 2.96

A higher relative humidity caused a significant reduction of water loss by evaporation in the experiments. However, using air sources with higher humidity also leads to lower CO_2 capture capacity. According to Wang et al., the adsorption of CO_2 on quaternary amine-functionalized resins involves the equilibrium between bicarbonate state and carbonate state (Eq 3).[114] When the resins are wet, they are mainly in the carbonate state, thus two active sites of the quaternary amine group can capture one CO_2 molecule in the form of carbonate. When the resins dry, the CO_2-H_2O equilibrium shifts to the bicarbonate state where the ratio between quaternary amine and CO_2 becomes 1:1, implying a higher CO_2 capture capacity. As a result, there is a trade-off between the CO_2 capture capacity of resins and water loss in the process.

$$(R_4N^+)_2CO_3^{2-} + H_2O + CO_2(g) \rightleftharpoons 2(R_4N^+HCO_3^-) \quad (3.3)$$

The maximum water retention capacity of the resins is 74%. If all retained water is evaporated during the adsorption experiment and given a CO_2 adsorption amount of 1.34 mmol/g (average from dry air experiments), the maximum specific water loss was 12.50 g

H_2O/g CO_2. The water loss during the experiments with dry air was higher than this maximum value, which indicated the operation of the experiments could be optimized to reduce the water loss. Moreover, one of the state of the art technologies using liquid alkaline absorbent for DAC consumes 4.32 g H_2O/g CO_2 captured at ambient conditions of 20 °C and 64% relative humidity.[45] Therefore, the experiments with humid air in this study already showed an average water loss in the same range as state of the art. Finally, other technologies (e.g., condensation) could be combined with the current adsorption step to retrieve the evaporated water.

3.3.4. Outlook and perspectives

The feasibility of a DAC system requires a low energy consumption, long lifetime of the sorbents, and low negative environmental impacts.[124] The energy consumption of the proposed technology mainly comes from the mechanical energy to overcome the pressure drop in the adsorber during adsorption and the electrical energy consumed by the electrochemical cell during desorption.

The mechanical energy required to supply the air through the adsorber is proportional to the pressure drop of the column. The pressure drop (Δp, Pa) can be estimated by Ergun equation[125]:

$$\frac{\Delta p}{L} = \frac{150\eta\,(1-\varepsilon)^2}{\varepsilon^2\,d_p^2}\,v_G + \frac{1.75\rho_G\,(1-\varepsilon)}{\varepsilon^3\,d_p}\,v_G^2 \tag{3.4}$$

Where L is the height of the packed bed (m), η is the dynamic viscosity of the fluid (Pa s), ε is the void fraction of the packing, d_p is the resin diameter (m), v_G is the channel velocity of the air inside the column (m s^{-1}), and ρ_G is the fluid density of air (kg m^{-3}). The pressure drop over the adsorber in this work was around 5000±1000 Pa at v_G = 20 cm s^{-1} (where the variation was due to changing water content of the resins during adsorption). However, while the design of the adsorber has been out of the scope of the present work, the bed height was not optimized (varying between 35 cm and 55 cm depending on the water content). As shown in eq. 3.4, the pressure drop increases linearly with the height of the packed bed. Thus, a shorter packed bed could be applied in future applications of the technology to achieve lower pressure drops. For instance, Yu and Brilman studied a packed bed of ion exchange resins with a height of 10^{-4} cm.[123] In their work, the mechanical energy for air supply could be as low as 26.4 kJ mol^{-1} CO_2 captured with a pressure drop of 118.4 Pa. Yu and Brilman have also proposed a radial flow contactor that showed a low energy consumption and a short adsorption time.[126] Moreover, further studies should investigate the pressure drop in the adsorber filled with wet resins. The void fraction of the packing ε is expected to decrease as the void would be partly filled with regeneration solution, which would increase the pressure drop. On the other hand, the resin diameter d_p increases when the resins are swelled with liquid, which would lead to a decrease in pressure drop. Therefore, the pressure drop profile

during one complete adsorption experiment needs to be studied in an optimally designed adsorber.

The average electrical energy consumption of the five desorption experiments in the laboratory was 537 ± 33 kJ mol^{-1} under 20 mA cm^{-2}. The electrochemical cell used in this study is not optimized as the electrode overpotentials of the cell count for approximately half of the energy consumption. We have achieved 374 kJ mol^{-1} under 5 mA cm^{-2} in our previous work, and the theoretical minimum energy consumption of the desorption step was 164 kJ mol^{-1}.[117] Higher current density resulted in higher electrode overpotentials. Therefore, future research should focus on developing strategies to reduce electrode overpotentials under high current density. Moreover, the adsorption step with AERs could potentially be combined with other electrochemical processes that can create a pH swing. For instance, Eisaman et al. proposed a bipolar membrane electrodialysis (BPMED) process for carbon capture, where a pH swing was built in two adjacent compartments alongside a bipolar membrane.[49] While combining with CO_2 capture using AERs, the low pH compartment could desorb high purity CO_2 gas, and the high pH compartment could reproduce the regeneration solution for the resins.

Finally, despite that the energy consumption of the system still needs to be optimized, the combined DAC process with AERs and the electrochemical regeneration has shown the potential to be further developed. The resins have a high CO_2 capture capacity of 1.76 mmol g^{-1} dry resins, and they are stable in 150 adsorption-desorption cycles. The sorbents need to last for tens of thousands of cycles to make the DAC process economically feasible,[127] so more studies should be conducted on the stability of the resins. However, due to the room-temperature operation of our combined DAC process, we believe the resins could outlast other thermal-regenerated sorbents. Furthermore, other solid sorbents can be investigated for the feasibility of electrochemical regeneration. Sorbents with high CO_2 capture capacity, high chemical stability, and low carbon footprint are necessary for practical application of the combination with electrochemical system.[128] Lastly, a techno-economic analysis would help find the optimal location for implementing such a process, as the local weather conditions (e.g., relative humidity) have a considerable impact on the capacity of the resins and the water loss of the process.

Supporting Information

Ion exchange capacity measurement methods

The ion exchange capacity (IEC) of the resins was quantified by a titration process. The resins (fresh or used) were rinsed with de-ionized (DI) water and then air-dried. Approximately 2 grams of the dry resins were taken for each titration. The resins were first immersed in 200 mL 1 mol/L NaOH for more than 12 hours (with stirring) so that all the resins should be in OH^- form. Afterwards, the resins were rinsed with DI water. Excess DI water was removed by filtration. The solid resin particles were transported to 50 mL 0.1 mol/L NaCl solution and immersed in the solution for more than 12 hours with stirring. The concentrations of Na^+ and Cl^- were measured by ion chromatography (761 Compact IC, Metrohm, Switzerland). The IEC of the resins is calculated by:

$$IEC = \frac{([Cl^-]_0 - [Cl^-]_1/([Na^+]_1/[Na^+]_0)) \times V}{M} \quad \text{(S3.1)}$$

where $[Cl^-]_0$ and $[Na^+]_0$ are the concentrations of Cl^- and Na^+ in the fresh prepared 0.1 mol/L NaCl solution (in mol L^{-1}), $[Cl^-]_1$ and $[Na^+]_1$ are the concentrations of Cl^- and Na^+ in the NaCl solution where the resins were immersed for more than 12 hours (in mol L^{-1}), V is the volume of the NaCl solution (in L), and M is the weight of dry resins used for the titration (in g).

Influent conditions for the 150 adsorption-desorption cycles

150 adsorption-desorption cycles were performed in a small column. During the adsorption steps, the CO_2 concentration and H_2O concentration in the air influent varies over time. The change of average influent CO_2 concentration and H_2O concentration in each cycle is plotted in **Figure S3.1**.

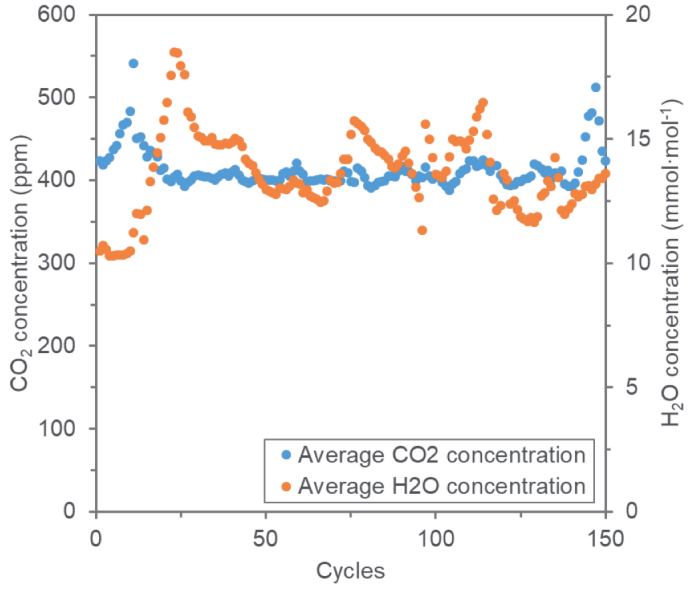

Figure S3.1. Average influent CO_2 concentration and H_2O concentration in the 150 adsorption-desorption cycles.

The flow rate of air influent in the 150 adsorption steps is depicted in **Figure S3.2**. Not all the cycles were measured due to practical limitations (e.g., overnight running of experiments). The flow rates of the cycles not measured were assumed to be the same as the last measured cycle before, for instance, the flow rate of cycle 2 to cycle 18 was assumed the same as the flow rate of cycle 1. Overall, the flow rate of the air influent decreased 11% from cycle 1 to 150.

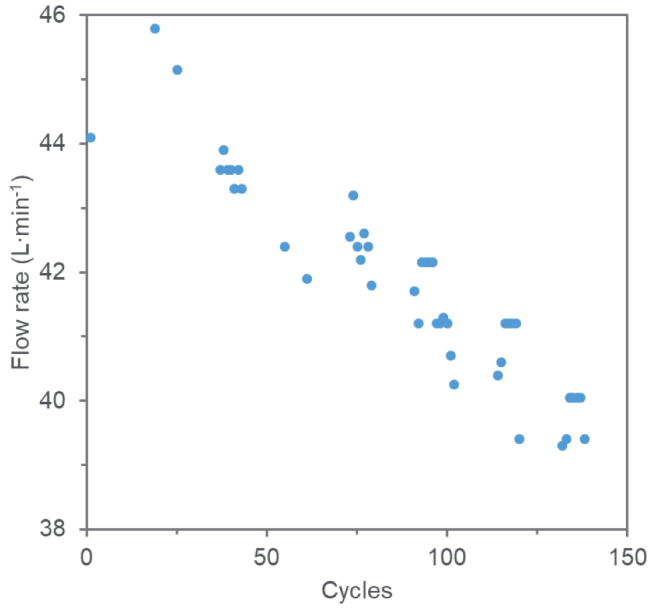

Figure S3.2. The flow rate of air influent during the 150 adsorption-desorption cycles

We have also corrected the proportional change of CO_2 adsorption amount based on a constant influent CO_2 concentration and a constant influent flow rate (**Figure S3.3**).

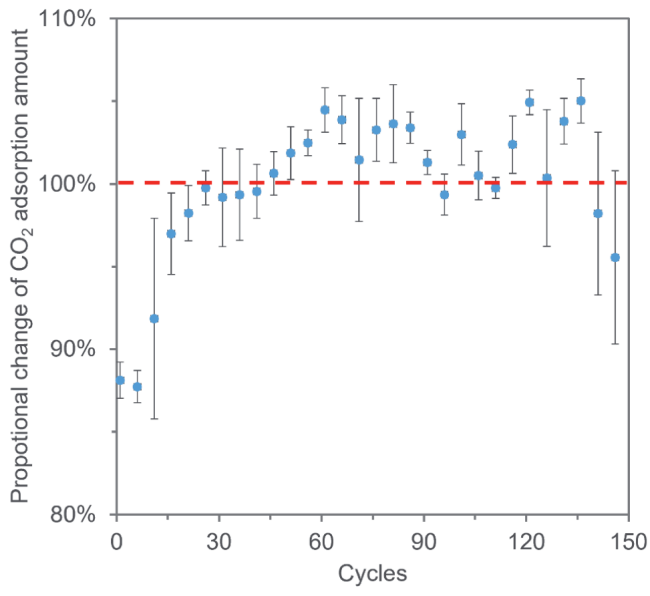

Figure S3.3. Proportional change of CO_2 adsorption amount in 150 adsorption-desorption cycles corrected by influent CO_2 concentration and flow rate.

Scanning electron microscope (SEM) and energy dispersive X-Ray spectroscopy (EDX) analysis of resin surface

The scanning electron microscope (SEM) and energy dispersive X-Ray spectroscopy (EDX) images of the surface of a used resin bead are shown in **Figure S3.4**. The weight percentage of all the elements detected are listed in **Table S3.1**. The precipitation on the surface of the resin was identified to contain mainly Na, C, and O.

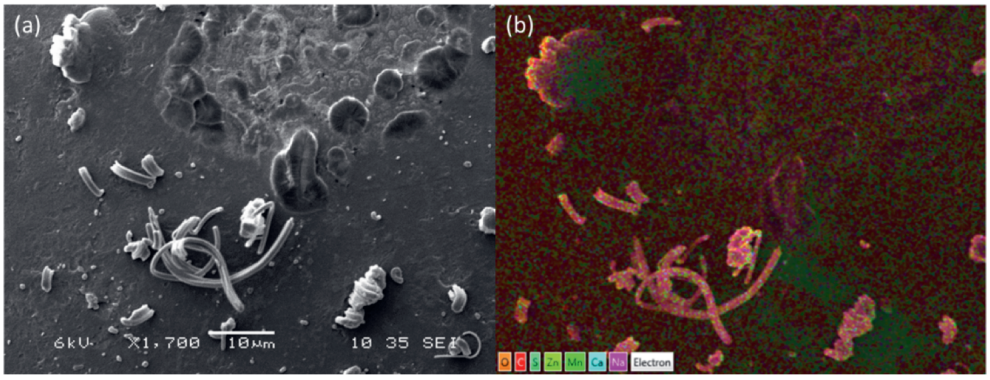

Figure S3.4. (a) Scanning electron microscope (SEM) and (b) energy dispersive X-Ray spectroscopy (EDX) images of the surface of a used resin bead.

Table S3.1. Weight percentage of the elements detected by energy dispersive X-Ray spectroscopy (EDX) analysis on the surface of a used resin bead.

Element	Wt%
C	79.84
O	16.77
Na	3.36
Al	0.01
Si	0.02
Total:	100.00

After rinsing the used resin with de-ionized water, the surface of the resin revealed to be rougher than the surface of a fresh resin (**Figure S3.5**).

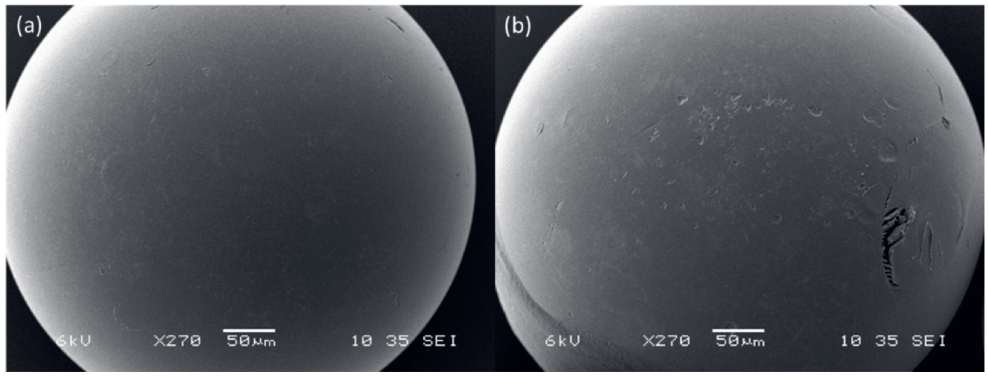

Figure S3.5. SEM image of (a) a fresh resin and (b) a used resin (rinsed by de-ionized water).

Adsorption with DI-water rinsed resins

After each regeneration step, a layer of the alkaline regeneration solution remains on the surface of the resins. We have performed one adsorption experiment with DI water-rinsed resins so that the influence of the remaining regeneration solution on the adsorption performance could be identified. **Table S3.2** showed the comparison of the CO_2 adsorption amount of the rinsed column with one of the non-rinsed column experiments. The effect of air humidity is excluded in this comparison as both experiments have a similar water loss. Therefore, the CO_2 adsorption amount decreased by 17% without the remaining regeneration solution.

Table S3.2. Comparison of CO_2 adsorption amount and water loss of non-rinsed and DI water-rinsed resin column.

	Non-rinsed column	DI water-rinsed column
Adsorption amount (mmol/g)	1.08	0.90
Water loss (L)	0.27	0.27

Composition of the gas desorbed from the electrochemical cell

The gas composition of the gas desorbed from the electrochemical cell is listed in **Table S3.3**. In all the experiments, the gas desorbed contains more than 96% of CO_2. The H_2 gas is likely permeated from the anode through the MEA to be present in acidifying solution and desorbed into gas phase, while the presence of O_2 and N_2 is most likely caused by the introduction of air during sampling.

Table S3.3. Gas composition of the desorbed gas from the electrochemical cell during 10 desorption experiments.

	CO_2	H_2	O_2	N_2
Experiment 1	97.80%	0.83%	0	1.37%
Experiment 2	96.21%	1.02%	0.64%	2.13%
Experiment 3	96.54%	0.78%	0.62%	2.06%
Experiment 4	96.95%	0.83%	0.59%	1.63%
Experiment 5	96.94%	0.81%	0.59%	1.66%
Experiment 6	96.44%	1.11%	0.65%	1.80%
Experiment 7	96.36%	1.07%	0.68%	1.89%
Experiment 8	96.77%	0.95%	0.61%	1.67%
Experiment 9	96.23%	1.17%	0.69%	1.91%
Experiment 10	97.82%	0.97%	0	1.21%

Change of measured parameters in a desorption step

During the desorption step, the pH of the acidifying solution decreased so that CO_2 could be desorbed into the gas phase (**Figure S3.6**a). Due to the ion exchange between OH^- and CO_3^{2-} /HCO_3^-, the conductivity of the outlet solution of the adsorber is lower than the conductivity of the inlet solution (**Figure S3.6**b). The desorption step finishes when the conductivities of the outlet and inlet solution of the adsorber are equal.

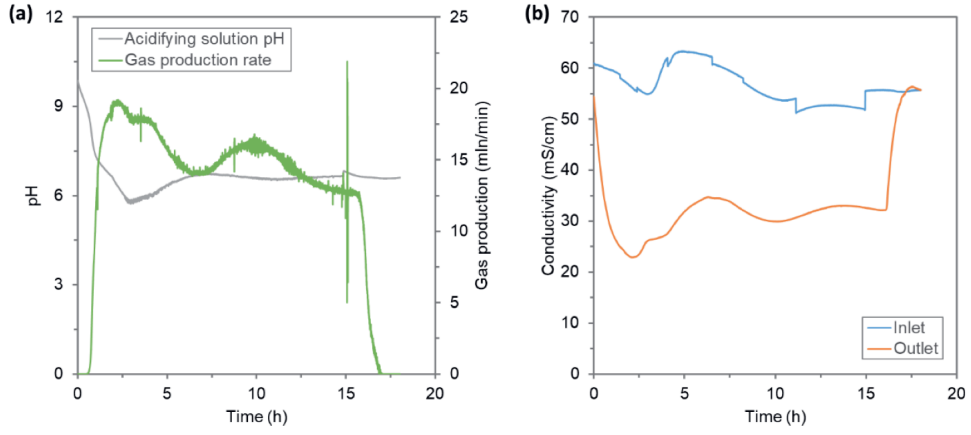

Figure S3.6. (a) The pH of acidifying solution and gas desorption rate change over time in a desorption step; (b) change of conductivity of the inlet and outlet solution of the adsorber over time during a desorption step.

四

Chapter 4

Optimization of an electrochemical direct air capture process with decreased CO_2 desorption pressure and addition of background electrolyte

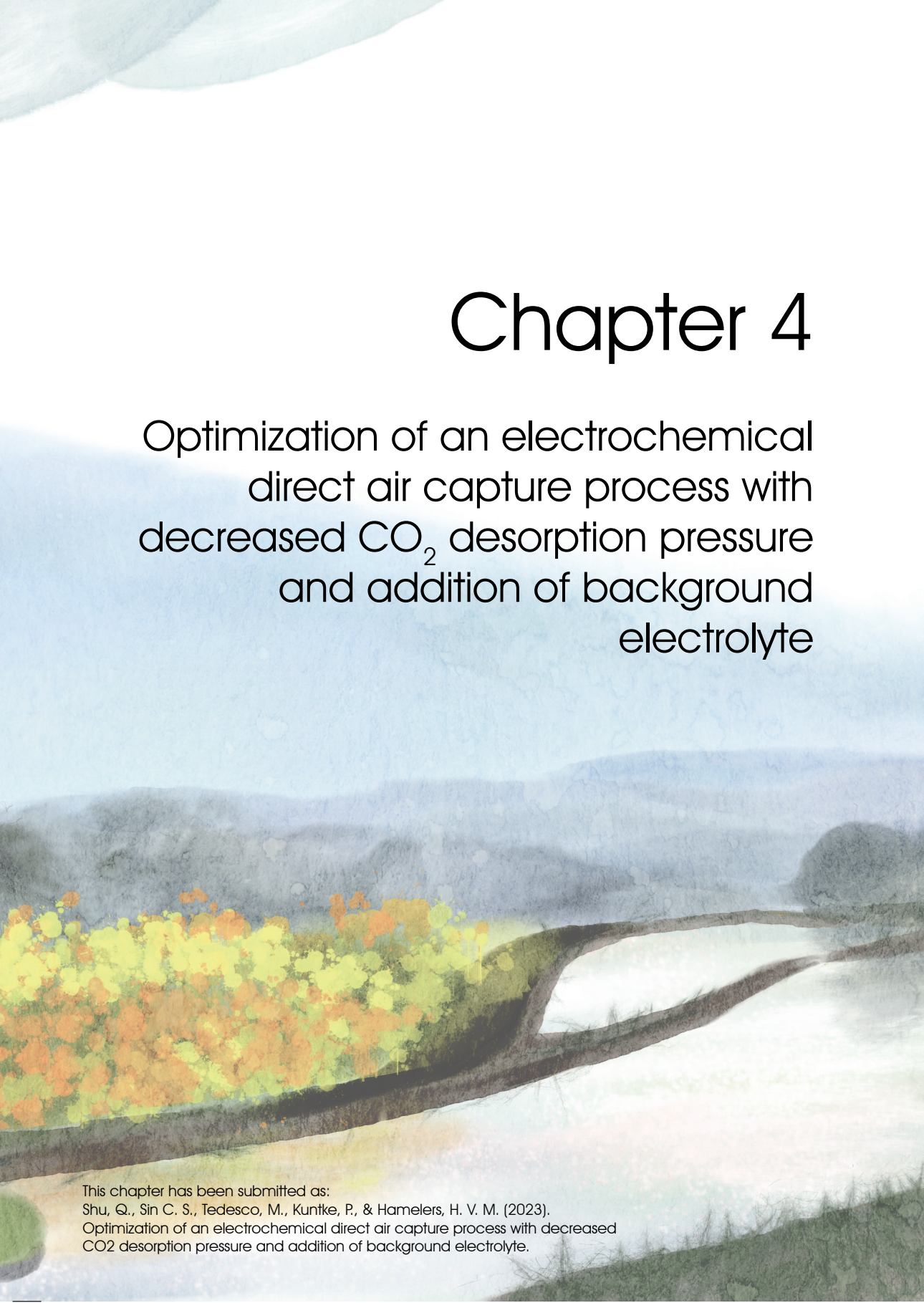

This chapter has been submitted as:
Shu, Q., Sin C. S., Tedesco, M., Kuntke, P., & Hamelers, H. V. M. (2023). Optimization of an electrochemical direct air capture process with decreased CO2 desorption pressure and addition of background electrolyte.

Abstract

An electrochemical process based on pH-swing has been proposed recently to regenerate spent alkaline absorbent from direct air capture (DAC). In this work, we experimentally investigated and theoretically simulated two optimization strategies to further reduce the energy consumption of such novel electrochemical process. First, partial vacuum was applied to the gas phase during CO_2 desorption to increase the gas production rate. The energy consumption of the electrochemical cell decreased by 12 to 15% when the CO_2 partial pressure in the gas phase was reduced from 0.9 to 0.3 atm. Second, phosphate and sulphate were tested as background electrolyte to the alkaline absorbent, reducing the energy consumption by minimizing the ohmic losses in the electrochemical cell. The optimal concentration for phosphate was 0.1 M, while the CO_2 production rate was limited by either the total carbon feeding rate or the high acidifying solution pH at higher concentrations of phosphate. Moreover, due to the low pKa and high molar conductivity of sulphate compared to phosphate, sulphate addition showed an even lower energy consumption than phosphate addition. Finally, the lowest experimental energy consumption was 247 kJ mol^{-1} CO_2 achieved with CO_2 partial pressure of 0.3 atm and 0.1 M of sulphate addition at current density of 150 A m^{-2} while our mathematical model predicted a theoretical minimum energy consumption of 138 kJ mol^{-1} under the same condition. Overall, the investigated optimization strategies advanced the development of an energy-efficient electricity-driven process for direct air capture.

4.1. Introduction

Climate change caused by anthropogenic emissions of greenhouse gases is one of the biggest threats of the century [129]. The atmospheric carbon dioxide (CO_2) concentration has increased by 50% comparing to pre-industrial level [130]. The heat-trapping nature of CO_2 has warmed the atmosphere, ocean, and land, which leads to vital signs of global warming, e.g., shrinking ice sheets, rising sea level, and more extreme natural events [131–133]. In response to the escalating impacts of climate change, carbon dioxide removal (CDR), aiming explicitly to reduce CO_2 levels from the atmosphere, has emerged as a crucial process that helps achieve carbon neutrality and provides opportunities for negative CO_2 emissions [134–136]. Direct air capture (DAC), a promising strategy of CDR, aims to produce high-purity CO_2 stream from ambient air via an adsorption/desorption cycle [137–139]. Although the low CO_2 concentration in the air makes DAC thermodynamically unfavourable comparing to other carbon capture processes from more CO_2-concentrated gas streams, DAC has the advantage of high flexibility in operation location, and the deployment of DAC technologies is critical for urgently mitigating the rapid climate change [140,141].

DAC with liquid alkaline absorbent and regeneration using a thermal swing has been demonstrated by Keith et al. [142]. Alternative electrochemical regeneration processes have been proposed to replace the consumption of thermal energy by electricity [143–146]. Several groups have studied using bipolar membrane electrodialysis (BPMED) to create a pH swing so that CO_2 is evolved from the spent absorbent under a low pH while the alkaline absorbent is regenerated under a high pH [147–150]. We recently showed the simultaneous CO_2 desorption and regeneration of spent DAC alkaline absorbent utilizing a H_2-recycling electrochemical system [151,152]. In this electrochemical system, H_2 is oxidized to protons (H^+) at the anode. The produced protons reduce the pH of the spent alkaline absorbent so that the carbonate (CO_3^{2-}) and bicarbonate (HCO_3^-) ions in solution are converted into carbonic acid ($H_2CO_3^*$, including dissolved CO_2). When the solution is saturated with carbonic acid, CO_2 gas evolves and is separated from the liquid solution. The CO_2-depleted solution is reduced at cathode where the alkaline absorbent is regenerated due to the production of hydroxide ion (OH^-). The reduction reaction at cathode also produces H_2 that can compensate for the H_2 consumption at anode.

Using such electrochemical DAC design, we have previously reached an energy consumption of 374 kJ mol^{-1} CO_2 under 50 A m^{-2}, while model predictions suggested a theoretical minimum as low as 164 kJ mol^{-1} CO_2 under same conditions [151]. The low energy consumption made this process competitive compared to the state of the art, such as the calciner thermal cycle process assessed by Keith et al. (338 kJ mol^{-1} CO_2) [142] and the bipolar membrane electrodialysis process evaluated by Sabatino et al. (236 kJ mol^{-1} CO_2) [153]. However, the gap between the experimental and simulated energy consumption implies an optimization potential. Therefore, in this work, we aim to investigate two operational strategies to reduce the energy consumption of the proposed DAC process.

The energy consumption of the process is inversely proportional to the CO_2 production rate and proportional to the electric power of the electrochemical cell. The CO_2 production rate is determined by the driving force for CO_2 desorption that originates from the difference between the dissolved CO_2 concentration and the CO_2 partial pressure in the gas phase, and lower CO_2 partial pressure in the gas phase facilitates the desorption of CO_2 from liquid phase to gas phase [154,155]. Therefore, in this work, we attempted to increase the CO_2 production rate of the electrochemical cell by applying partial vacuum to the gas phase during the desorption step. Moreover, we also showed the impact of reduced CO_2 partial pressure in the gas phase on the performance of the electrochemical cell under different operational conditions.

Under galvanostatic (i.e., constant current) conditions, the power of the electrochemical cell is dominated by the potential drop over the cell. The potential drop largely depends on the ohmic resistance of the solutions and the electrode overpotentials. In this regard, we added background electrolytes in different concentrations and forms to the absorbent to increase the ionic conductivity and studied the effect on the performance of the system. Sabatino et al. simulated the addition of inert salt in a bipolar membrane electrodialysis DAC process and showed the benefit of reducing the energy consumption [156]. Furthermore, Jeremiasse et al. demonstrated that the concentration overpotential for hydrogen evolution was reduced in the presence of buffer [157]. Thus, we compared one background electrolyte with buffer capacity (phosphate) and one without buffer capacity (sulphate) to explore the difference in system performance under different operational conditions.

4.2. Materials and methods

4.2.1. Experimental setup

The electrochemical cell consisted of three compartments, i.e., anode compartment, acidifying compartment, and cathode compartment, enclosed by two poly(methyl methacrylate) (PMMA) endplates (21 cm × 21 cm × 2.5 cm) (**Figure 4.1**). Two Ru/Ir-coated titanium mesh electrodes (9.8 cm X 9.8 cm) were used, one as the cathode and the other as the current collector for the anode. The anode was a membrane electrode assembly (MEA) (FuelCellsEtc, USA) comprising a gas diffusion layer (GDL) (10 cm X 10 cm), coated by a Platinum-Vulcan (carbon) catalyst (0.5 mg Pt cm^{-2}), incorporated with a Nafion N117 cation exchange membrane (CEM) (15 cm X 15 cm). The GDL side and the CEM side of the MEA were facing the anode compartment and acidifying compartment, respectively. The acidifying and cathode compartments were separated by an additional CEM (15 cm X 15 cm, Fumasep FKB-PK-75, FUMATECH, Germany), and two polymeric nitrile spacers (500 μm thick, Sefar, Switzerland) were used to create the flow channel for these two compartments.

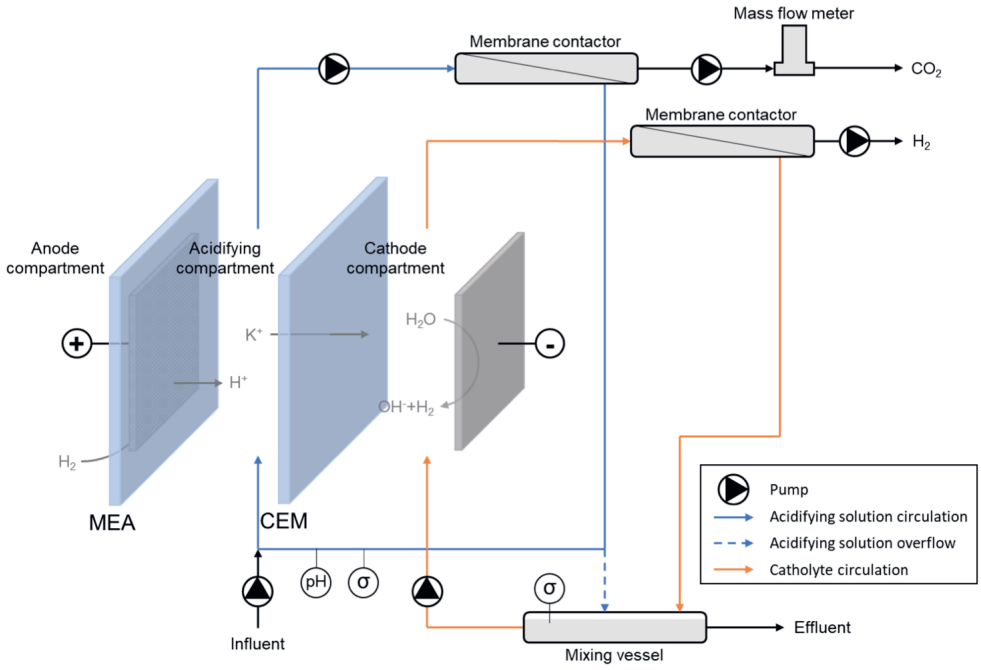

Figure 4.1. Schematic representation of the process with electrochemical regeneration of alkaline DAC absorbent. Influent: spent alkaline absorbent from the absorber. Effluent: regenerated absorbent to send to the absorber. MEA = membrane electrode assembly, CEM = cation exchange membrane.

Two circulation loops were used for the acidifying and cathode compartments, respectively. In each circulation loop, the outlet from the cell was directed into a hollow fibre membrane contactor (Liqui-Cel™ EXF-2.5×8, 3M, USA), where the produced CO_2 (or H_2) gas could be separated, and the liquid stream from the membrane contactor flowed back into the cell. The influent of the system, which was the spent alkaline absorbent, was mixed with the acidifying solution before entering the acidifying compartment. While the overflow of acidifying solution flowed into the mixing vessel in the catholyte circulation loop, the overflow of surplus catholyte left the circulation as effluent. Three peristaltic pumps (Masterflex L/S, Metrohm Applikon BV, the Netherlands) were installed in the system, one for the influent and two for the two circulation loops (800 mL min^{-1}). Two additional peristaltic pumps (Masterflex L/S, Metrohm Applikon BV, the Netherlands) were connected to the gas outlets of the membrane contactors to maintain the desired air pressure, which was measured by two manometers (Cerabar PMP21, Endress+Hauser, Germany; MAN-SD1S, Kobold Messering GmbH, Germany). The gas side of the membrane contactor in the catholyte circulation loop was kept at a gas pressure of 0.70 atm to enhance the removal efficiency of H_2, and avoid gas entrained in the cell through the circulation loop. In the CO_2 gas stream, the water vapor of the separated gas was removed via a Nafion tubing (TUB-0003, CO2Meter.com, USA). The gas production rate was recorded by a mass flow meter (EL-FLOW Prestige FG-111B, Bronkhorst, the Netherlands). Gas samples were taken from the setup during experiments,

and their compositions were analyzed by gas chromatography (μGC, Varian CP-4900, Agilent, USA). Although the H_2 produced at the cathode could be in principle directly recirculated to the anode, a tailor-made electrolyzer was used to feed H_2 to the anode for simplicity.

A galvanostatic/potentiostat (IviumStat, Ivium, the Netherlands) was connected to the cell to apply a constant current. Two saturated calomel reference electrodes (+0.244 V vs SHE, QM712X, ProSense BV, the Netherlands) were placed at the inlets of the acidifying and cathode compartments to measure the anode and cathode potentials. A multimeter (8846A, Fluke, the Netherlands) was connected between the two reference electrodes to measure the potential difference across the acidifying and cathode compartments. The conductivities of the acidifying and catholyte solutions were measured by two conductivity sensors (Memosens CLS82D, Endress+Hauser BV, the Netherlands) placed in the two circulation loops, while the pH of the acidifying solution was measured by a pH sensor (Orbisint CPS11D, Endress+Hauser BV, the Netherlands). The concentrations of ions in the influent, the acidifying solution, and the catholyte solution were measured by ion chromatography (761 Compact IC, Metrohm, Switzerland).

4.2.2. Experimental procedure

The experiments were operated in a continuous mode with the influent solution constantly feeding into the acidifying circulation loop until the complete system reached steady-state. The influent solutions for the electrochemical system resembled spent potassium hydroxide absorbents. The composition is determined by the equilibrium between 400 ppm of CO_2 under atmospheric pressure and the alkaline absorbent based on Henry's law and the equilibria of species in the liquid phase. The equilibria change with different K^+ concentrations, different background electrolyte addition, and different concentrations of the background electrolyte. The detailed compositions of all the influent solutions are listed in **Table S4.1**.

To evaluate the performance of the system under different fluid dynamic and current conditions, we defined the "K^+ load ratio" (L_{K^+}) as a control parameter to describe the ratio between the applied current density and the K^+ loading rate:

$$L_{K^+} = \frac{j_c\, A}{c_{K^+,0}\, Q\, F} \tag{4.1}$$

where j_c is the current density (A m^{-2}), A is the active membrane area (m^2), $c_{K^+,0}$ is the K^+ concentration in the influent (mol m^{-3}), Q is the influent flow rate (m^3 s^{-1}), and F is the Faraday constant (96485 C mol^{-1}).

Firstly, the effect of pressure at the gas side of the membrane contactor ($p_{CO_2,g}$) on the performance of the system was investigated. Three different conditions were selected to perform experiments with $p_{CO_2,g}$ ranging from 0.3 to 0.9 atm (**Table 4.1**). Secondly, experiments with different amount of phosphate buffer solution addition (no buffer, 0.1 M buffer,

and 0.2 M buffer) were performed under the optimum $p_{CO_2,g}$ identified previously. The current density was kept constant at 150 A m^{-2}, while the influent K^+ concentration was 1.0 M. Different L_{K^+} from 0.7 to 1.1 were tested by adjusting the influent flow rate. Moreover, we have performed experiments with fixed total carbon concentration in the influent and fixed influent flow rate, to keep constant the total carbon feeding rate into the cell. In this case, the influent K^+ concentration along with the L_{K^+} were different with different amount of buffer addition. Lastly, experiments with 0.1 M sulphate addition were performed to compare with experiments with 0.1 M phosphate buffer addition under different L_{K^+}.

Table 4.1. Different operational conditions for experiments investigating effects of pressure at the gas side of the membrane contactor ($p_{CO_2,g}$).

	Current density (A m^{-2})	L_{K^+}	Phosphate buffer
Condition 1	150	0.8	0.1 M
Condition 2	150	0.9	0.1 M
Condition 3	200	0.8	0.1 M

4.2.3. Equilibrium model

An equilibrium model was developed to simulate the performance of the electrochemical cell. The simulation describes the mass transport and steady-state conditions of the acidifying and cathode compartments with some general assumptions including: i) well-mixed compartments; ii) ideal membrane behavior; and iii) no neutral species (H_2CO_3 and H_3PO_4) transport through the membrane.

Solution equilibrium

The solutions contain cations (K^+ and H^+), anions (OH^-, HCO_3^-, CO_3^{2-}, $H_2PO_4^-$, HPO_4^{2-}, PO_4^{3-}, and SO_4^{2-}), and neutral species (H_2CO_3 and H_3PO_4), and they are assumed to be always in acid-base equilibrium. They equilibrium constants are defined as follows:

$$K_H = \frac{c_{H_2CO_3}}{p_{CO_2(g)}} \tag{4.2}$$

$$K_{c1} = \frac{c_{H^+}\, c_{HCO_3^-}}{c_{H_2CO_3}} \tag{4.3}$$

$$K_{c2} = \frac{c_{H^+}\, c_{CO_3^{2-}}}{c_{HCO_3^-}} \tag{4.4}$$

$$K_{p1} = \frac{c_{H^+}\, c_{H_2PO_4^-}}{c_{H_3PO_4}} \tag{4.5}$$

$$K_{p2} = \frac{c_{H^+}\, c_{HPO_4^{2-}}}{c_{H_2PO_4^-}} \tag{4.6}$$

$$K_{p3} = \frac{c_{H^+}\, c_{PO_4{}^{3-}}}{c_{HPO_4{}^{2-}}} \tag{4.7}$$

$$K_w = c_{H^+}\, c_{OH^-} \tag{4.8}$$

where K_H is the Henry' law constant of CO_2 (mol m^{-3} atm^{-1}), K_{c1} and K_{c2} are the first and second dissociation constants of H_2CO_3 (mol m^{-3}), respectively, K_{p1}, K_{p2}, and K_{p3} are the first, second, and third dissociation constants of H_3PO_4 (mol m^{-3}), respectively, K_w is the water dissociation constant (mol^2 m^{-6}), $p_{CO_2(g)}$ is the partial pressure of CO_2 gas, and $c_{H_2CO_3}$, $c_{HCO_3{}^-}$, $c_{CO_3{}^{2-}}$, $c_{H_3PO_4}$, $c_{H_2PO_4{}^-}$, $c_{HPO_4{}^{2-}}$, $c_{PO_4{}^{3-}}$, c_{H^+}, and c_{OH^-} are the concentrations of corresponding ions (M), respectively.

The electroneutrality of all charged species holds in all solutions:

$$c_{K^+} + c_{H^+} = c_{OH^-} + c_{HCO_3{}^-} + 2\, c_{CO_3{}^{2-}} + c_{H_2PO_4{}^-} + 2\, c_{HPO_4{}^{2-}} + 3\, c_{PO_4{}^{3-}} + 2\, c_{SO_4{}^{2-}} \tag{4.9}$$

where $c_{SO_4{}^{2-}}$ is the concentration of SO_4^{2-} (mol m^{-3}).

The influent of the acidifying compartment is a solution in equilibrium with 1 atm 400 ppm CO_2 that consists of 1.0 M K^+. The acidifying solution is in equilibrium with a defined gas pressure in the membrane contactor (assuming pure CO_2).

Either phosphate or sulphate is added to the influent when simulating the corresponding experiments.

Mass transport

The applied current density determines the total flux of cations (K^+ and H^+) transported through the CEM:

$$J_{tot} = J_{K^+} + J_{H^+} = \frac{j_c}{F} \tag{4.10}$$

where J_{tot} is the total molar flux of cations through the CEM (mol m^{-2} s^{-1}) and J_{K^+} and J_{H^+} are the molar fluxes of K^+ and H^+ (mol m^{-2} s^{-1}), respectively.

The ion fluxes can be expressed by Nernst-Planck equation:

$$J_{K^+} = -D_{K^+}\left(\frac{dc_{K^+}}{dx} + c_{K^+,m}\frac{d\phi}{dx}\right) \tag{4.11}$$

$$J_{H^+} = -D_{H^+}\left(\frac{dc_{H^+}}{dx} + c_{H^+,m}\frac{d\phi}{dx}\right) \tag{4.12}$$

where D_{K^+} and D_{H^+} are the diffusion coefficients of K^+ and H^+ (m^2 s^{-1}), respectively, c_{K^+} and c_{H^+} are the concentrations of K^+ and H^+ at different positions inside the membrane (mol m^{-3}), respectively, $c_{K^+,m}$ and $c_{H^+,m}$ are the average concentrations of K^+ and H^+ in the

membrane (mol m^{-3}), respectively, x is the position inside the membrane (m), and ϕ is the dimensionless electric potential, to be multiplied by RT/F (R: ideal gas constant = 8.314 J K^{-1} mol^{-1}, T: temperature in K) to obtain the dimensional voltage.

The concentration gradient of cations over the CEM is assumed to be linear, and the boundary conditions of the membrane are not considered so that the ion concentration on the surface of the membrane equals the concentration in the bulk solution.

Mass balances

The mass balances of K^+ and total carbon in acidifying and cathode compartments were considered under steady-state conditions. In the acidifying compartment, the K^+ transported away equals the concentration difference between the influent ($c_{K^+,0}$, mol m^{-3}) and the acidifying solution ($c_{K^+,1}$, mol m^{-3}):

$$J_{K^+} = \frac{Q}{A}\,(c_{K^+,0} - c_{K^+,1}) \tag{4.13}$$

CO_2 is desorbed from the acidifying solution as the pH decreases. Therefore, the total carbon concentration difference between the influent ($c_{C,0}$, mol m^{-3}) and the acidifying solution ($c_{C,1}$, mol m^{-3}) corresponds to the specific CO_2 production rate (J_{CO_2}, mol m^{-2} s^{-1}):

$$J_{CO_2} = \frac{Q}{A}\,(c_{C,0} - c_{C,1}) \tag{4.14}$$

The transported K^+ and the remaining part in the acidifying solution blend in the cathode compartment, so the catholyte has the same K^+ concentration as the influent. Since no carbon species leaves the solution after the membrane contactor, the total carbon concentration in the catholyte remains as in the acidifying solution.

Energy consumption

This model assumes an ideal electrical behavior in the cell which neglects the electrode overpotentials and the boundary layer effects of the electrodes and membrane. Therefore, the cell voltage (E_{cell}, V) is calculated as the sum of equilibrium potential (E_{eq}, V), membrane potential (E_m, V), and ohmic losses (E_{ohmic}, V).

$$E_{cell} = E_{eq} + E_m + E_{ohmic} \tag{4.15}$$

E_{eq} is the potential invested in creating the pH difference between the anode (pH_{anode}) and cathode ($pH_{cathode}$) considering each pH unit requires 59.2 mV of potential drop:

$$E_{eq} = 0.0592\,(pH_{cathode} - pH_{anode}) \tag{4.16}$$

E_m is the potential drop over the CEM resulted from K^+ concentration gradient:

$$E_m = \frac{R\,T}{F} \ln \frac{c_{K^+,2}}{c_{K^+,1}} \tag{4.17}$$

where $c_{K^+,2}$ is the K^+ concentration in the catholyte (mol m^{-3}).

E_{ohmic} includes the potential drops in the acidifying and cathode compartments due to ionic resistance:

$$E_{ohmic} = j_c \left(\frac{d_a}{\sigma_a} + \frac{d_c}{\sigma_c}\right) \tag{4.18}$$

where d_a and d_c are the thicknesses of the acidifying and cathode compartments (m), respectively, and σ_a and σ_c are the conductivities of the acidifying solution and catholyte (S m^{-1}), respectively.

Finally, the energy consumption (EC) is then calculated by:

$$EC = \frac{E_{cell}\, j_c}{J_{CO_2}} \tag{4.19}$$

4.3. Results and discussion

4.3.1. Effects of decreased CO_2 desorption pressure

In the experiments with reduced CO_2 partial pressure at the gas side ($p_{CO_2,g}$) of the membrane contactor, the energy consumption of the electrochemical system decreased with decreasing p_{CO_2} (**Figure 4.2**). We have observed this decrease in energy consumption under applied partial vacuum with different applied current densities and different load ratios of K^+ (L_{K^+}).

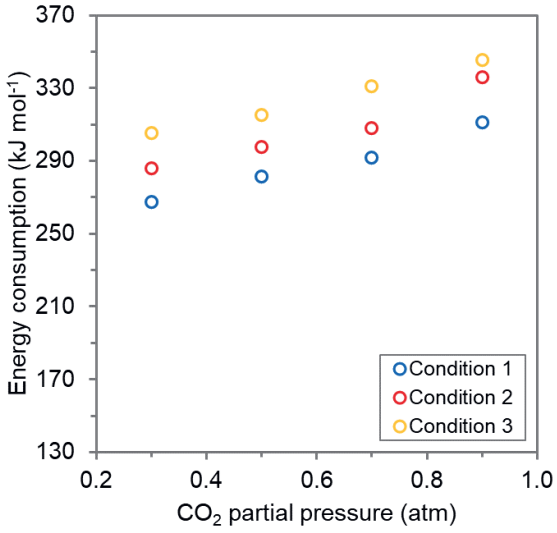

Figure 4.2. Energy consumption at different CO_2 partial pressure at the gas side of the membrane contactor ($p_{CO_2,g}$). Condition 1: j_c = 150 A m^{-2}, L_{K^+} = 0.8, 0.1 M phosphate buffer; condition 2: j_c = 150 A m^{-2}, L_{K^+} = 0.9, 0.1 M phosphate buffer; condition 3: j_c = 200 A m^{-2}, L_{K^+} = 0.8, 0.1M phosphate buffer.

The decrease in energy consumption originated from two aspects: increased CO_2 production rate and decreased cell voltage. The driving force for CO_2 desorption was the difference in CO_2 partial pressure between the liquid and gas side of the membrane contactor [158], so reducing $p_{CO_2,g}$ increased the CO_2 production rate (**Figure 4.3**a). With $p_{CO_2,g}$ decreased from 0.9 atm to 0.3 atm, the benefits from increasing CO_2 production rate accounted for 84% of the total energy reduction at the experimental conditions with L_{K^+} = 0.8 (condition 1 & 3), while this benefit accounted only for 54% at condition 2 with L_{K^+} = 0.9. In condition 2, the pH of the acidifying solution was around 1-unit lower comparing to the acidifying solution in condition 1. The lower acidifying solution pH resulted in a higher concentration of H_2CO_3 and a higher CO_2 partial pressure in the liquid phase. Hence, the driving force for CO_2 desorption was higher under condition 2 comparing to condition 1, which led to a higher CO_2 production rate at $p_{CO_2,g}$ = 0.9 atm. When $p_{CO_2,g}$ decreased to 0.3 atm, the applied partial vacuum dominated the desorption of CO_2 so that the difference in CO_2 production rate was minimized. The model results showed the same trend of CO_2 production rate change in all the conditions with different $p_{CO_2,g}$, although the overall values of the simulation were higher than the experimental results, likely due to some CO_2 leakage during experiments.

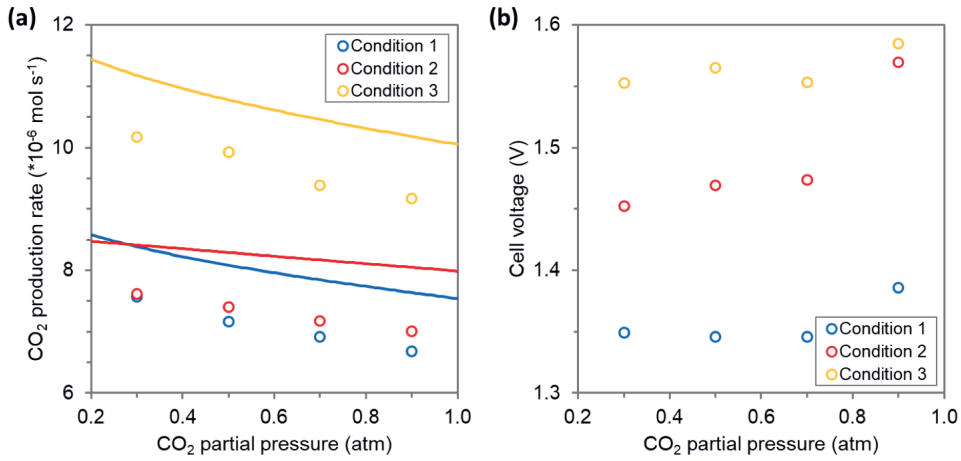

Figure 4.3. Change of (a) CO_2 production rate and (b) cell voltage under different p_{CO_2} values. Condition 1: j_c = 150 A m^{-2}, L_{K^+} = 0.8, 0.1 M phosphate buffer; condition 2: j_c = 150 A m^{-2}, L_{K^+} = 0.9, 0.1 M phosphate buffer; condition 3: j_c = 200 A m^{-2}, L_{K^+} = 0.8, 0.1M phosphate buffer. Symbols (○): experimental data; lines: model predictions.

The applied partial vacuum reduced the cell voltage especially when $p_{CO_2,g}$ decreased from 0.9 to 0.7 atm (**Figure 4.3**b). One assumption for the reduced cell voltage was that the elimination of CO_2 gas bubbles in the cell decreased the electrical resistance. Generally, the CO_2 gas formed inside the cell could be carried out instantly by the liquid flow. However, some bubbles may remain trapped in the meshed spacer, thus increasing the electrical resistance [159,160]. With a reduced pressure in the gas phase, the volumes of the gas (bubbles) formed were bigger according to ideal gas law. Therefore, the larger-volume bubbles were easier to be carried out of the cell by the liquid flow instead of being trapped in the spacer [161]. This elimination of gas bubbles occurred mainly between $p_{CO_2,g}$ of 0.9 and 0.7 atm, and further decrease of $p_{CO_2,g}$ did not have a significant impact on the cell voltage. Moreover, as the model did not include the effect of gas bubbles on cell voltage, so the results of the model simulation were not presented in the figure.

Low pressure of the desorbed CO_2 creates an energy penalty for the downstream processes as CO_2 needs to be pressurized for transport and storage [162,163], e.g., the thermodynamical minimum energy required to pressurize CO_2 gas from 0.3 atm to 0.9 atm is 2.7 kJ mol^{-1}. Although the practical energy consumption to compress CO_2 gas at lower pressure requires slightly more energy due to the larger volume of gas [164], this energy penalty is negligible comparing to the reduction of energy consumption (i.e., 40-50 kJ mol^{-1} in the experimental conditions tested) brought by the applied partial vacuum during CO_2 desorption. Therefore, a decreased CO_2 desorption pressure is beneficial for reducing the overall energy consumption of the electrochemical system by increasing CO_2 production rate and decreasing cell voltage.

4.3.2. Effect of phosphate buffer on cell performance

We expected the addition of phosphate buffer to the absorbent would lower the energy consumption by reducing the ohmic resistance and the electrode overpotential. However, in this study, the energy consumption of experiments with buffer addition was not always lower than the experiments without buffer addition. Instead, adding phosphate buffer shifted the optimal L_{K^+} for the lowest energy consumption of the electrochemical cell (**Figure 4.4**). The lowest energy consumption was achieved without adding buffer at L_{K^+} = 1.0, with 0.1 M buffer at L_{K^+} = 0.8, and with 0.2 M buffer at L_{K^+} = 0.7 (energy consumption of 305 kJ mol^{-1}, 267 kJ mol^{-1}, and 297 kJ mol^{-1}, respectively). This shift of optimal L_{K^+} was also observed with the model simulation where the optimal L_{K^+} value decreases with increasing buffer concentration. Overall, both experimental and model results show that the lowest energy consumption of all investigated conditions occurred with 0.1 M buffer at L_{K^+} = 0.8.

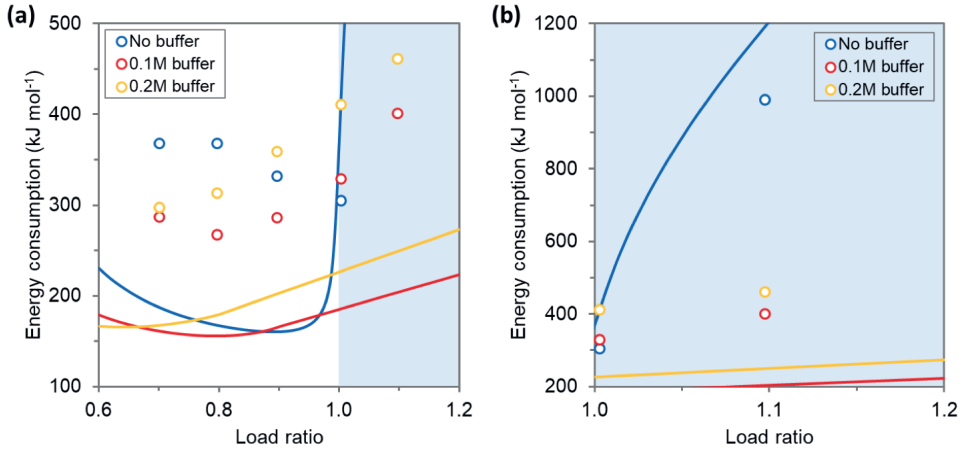

Figure 4.4. Energy consumption under different load ratio and phosphate buffer concentration. (a) Load ratio range between 0.6 and 1.2, (b) a zoomed view for load ratio between 1.0 and 1.2. Symbols (○): experimental data; lines: model predictions.

The energy consumption is proportional to the cell voltage and inversely proportional to the CO_2 production rate. Cell voltage increased with higher L_{K^+} owing to the lower conductivity of the acidifying solution and higher potential drop at the boundary layers of the MEA and CEM (**Figure 4.5**a). As more K^+ ions were transported to the cathode compartment and CO_3^{2-}/HCO_3^- ions were converted to CO_2 gas, the conductivity of the acidifying solution decreased with a higher L_{K^+} (**Table S4.2**), which led to a greater ohmic loss in the cell. Moreover, this depletion of K^+ and CO_3^{2-}/HCO_3^- ions was intensified near the surface of the MEA at the acidifying compartment side, which resulted in a larger potential drop at the boundary layer of the MEA [165]. Furthermore, the K^+ concentration gradient over the CEM was larger with a higher L_{K^+} (**Table S4.2**), and this larger gradient contributed to the increase of the membrane potential of the CEM [166]. On the other hand, adding phosphate buffer provided

extra conductivity in both the acidifying solution and the boundary layer of the MEA, since the anionic phosphate species remained in the acidifying solution increased the total ion concentration. Hence, we observed a lower cell voltage with more phosphate buffer added, and the difference of cell voltage was larger with a higher L_{K^+} when more K^+ and CO_3^{2-}/HCO_3^- were removed. Although Jeremiasse et al. showed a reduced concentration overpotential for hydrogen evolution with phosphate buffer addition [157], this reduction was not evident in our experiments due to the extreme catholyte pH (>13). The small fluctuation of the cathode overpotential (**Table S4.3**) could be explained by the influence of hydrogen gas bubbles on the cathode potential measurement [161].

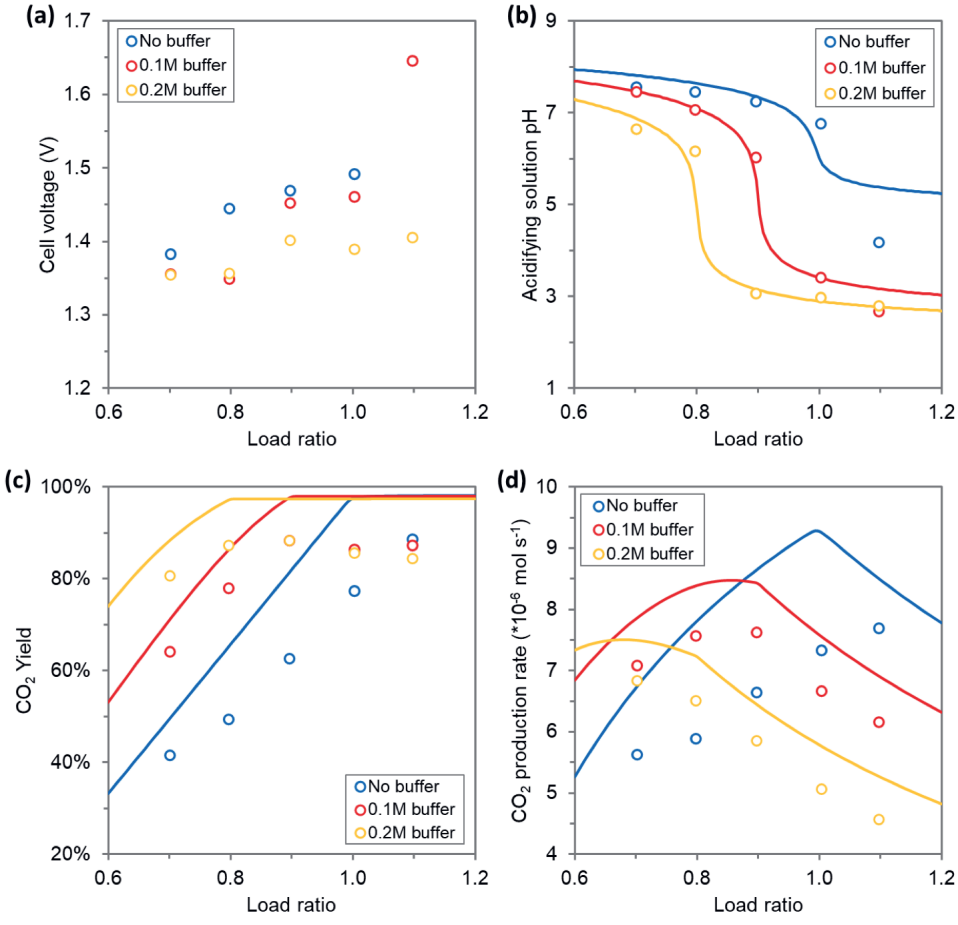

Figure 4.5. Experimental and model simulated results of (a) cell voltage, (b) acidifying solution pH, (c) CO_2 yield, and (d) CO_2 production rate under different load ratio and phosphate buffer concentration. Symbols (○): experimental data; lines: model predictions.

The protons produced at the anode were transported to the acidifying compartment under the applied constant current, which led to the decrease of the acidifying solution pH. The

steady-state pH of the acidifying solution decreased at a higher L_{K^+} (**Figure 4.5**b), which was attributed to more protons received by each unit volume of acidifying solution. This decrease in pH was not linear to the increase in L_{K^+} due to the buffering effect of CO_3^{2-}/HCO_3^- ions and/or the added phosphate buffer. In the experiments without buffer, the acidifying solution needed to overcome two buffering zones of CO_3^{2-}/HCO_3^- (pK_a = 10.33 and 6.35). The concentration of CO_3^{2-}/HCO_3^- ions was reduced in the experiments with phosphate buffer since the total K^+ concentration in the influent was remained constant in all the experiments. Moreover, phosphate buffer only has one buffering zone (pK_a = 7.20) in the pH range of the desired pH swing in the acidifying solution. As a result, the addition of phosphate buffer solution decreased the steady-state pH of the acidifying solution. This conclusion also explains the discrepancy between the experimental and simulated acidifying solution pH at L_{K^+} = 1.1 with no buffer addition, as any background anions "contamination" in the experiments would decrease the acidifying solution pH.

Due to the displacement of CO_2 equilibria, more CO_2 could be evolved with a lower pH of the acidifying solution. Thus, the CO_2 yield, which is defined as the ratio of CO_2 gas production rate to the total carbon feeding rate into the cell, followed a reverse trend to the pH of the acidifying solution (**Figure 4.5**c). The yield reached its maximum when all the dissolved carbon species had been converted to H_2CO_3 at around pH = 4. At $p_{CO_2,g}$ = 0.3 atm, the concentration of H_2CO_3 in the acidifying solution was 10.2 mM based on Henry's law. This 10.2 mM of H_2CO_3 could not be desorbed into the gas phase even with further decrease of the acidifying solution pH at higher L_{K^+}, so the yield kept constant at the maximum. Due to less total carbon in the influent of experiments with phosphate buffer, the remained H_2CO_3 accounted for a larger portion in these experiments. Hence, the maximum CO_2 yield decreased with increasing concentration of phosphate buffer.

Although the CO_2 yield was proportional to the CO_2 production rate, the change of the CO_2 production rate did not follow the same trend as the CO_2 yield, due to the variation of the total carbon feeding rate (**Figure 4.5**d). In experiments with the same buffer concentration, the total carbon feeding rate decreased with higher L_{K^+} attributed to the lower flow rate of the influent (1.33 mL min^{-1} at L_{K^+} = 0.7 while 0.85 mL min^{-1} at L_{K^+} = 1.1). Consequently, the CO_2 production rate decreased sharply after the CO_2 yield reached the maximum. Moreover, the total carbon feeding rate decreased by 19% and 38% with 0.1 M and 0.2 M phosphate buffer added, respectively. Therefore, the CO_2 production rate of the experiments without buffer addition exceeded those of the experiments with buffer added at higher L_{K^+}.

As shown in **Figure 4.4**, the experiments with no buffer addition had the lowest energy consumption at L_{K^+} = 1.0, which was lower than in the experiments with buffer addition at the same L_{K^+}. However, the buffer addition limited the total carbon feeding rate. Thus, we have also performed experiments with fixed total carbon feeding rate (**Table 4.2**). The lowest energy consumption was achieved with 0.1 M phosphate buffer added, which was confirmed

by the model simulation (617 kJ mol^{-1} without buffer, 156 kJ mol^{-1} with 0.1 M buffer, 160 kJ mol^{-1} with 0.2 M buffer). Adding phosphate provided extra conductivity in the acidifying compartment and lowered the L_{K^+} due to the increasing influent K^+ concentration, so the cell voltage was lower with more buffer added. Moreover, the acidifying solution pH was comparable between the experiment without buffer and with 0.1 M buffer, but the CO_2 production rate with 0.1 M buffer was 4% higher, which indicated that adding phosphate buffer facilitated the desorption of CO_2 gas. However, in the experiment with 0.2 M buffer, the CO_2 production rate was the lowest due to the higher acidifying solution pH at a relatively low L_{K^+}.

Table 4.2. Experimental conditions and results of the experiments with fixed total carbon feeding rate.

	No buffer	**0.1 M buffer**	**0.2 M buffer**
Total carbon feeding rate (mol s^{-1})	9.5×10^{-6}	9.5×10^{-6}	9.5×10^{-6}
L_{K^+}	1.00	0.84	0.72
Energy consumption (kJ mol^{-1})	305	273	286
Cell voltage (V)	1.49	1.38	1.35
Acidifying solution pH	6.8	6.8	7.3
CO_2 production rate (mol s^{-1})	7.3×10^{-6}	7.6×10^{-6}	7.1×10^{-6}

4.3.3. Effects of adding sulphate solution

As the previous section concludes, adding 0.1 M phosphate buffer reduced the energy consumption of the electrochemical system, where phosphate essentially acts as a supporting electrolyte in the system. In fact, adding sulphate to the absorbent reduced the energy consumption even further, while the energy consumption trend with different L_{K^+} is the same with both phosphate and sulphate (**Figure 4.6**). Thus, among all the investigated experimental conditions, the lowest energy consumption was 247 kJ mol^{-1} achieved at $p_{CO_2,g}$ = 0.3 atm, L_{K^+} = 0.8, j_c = 150 A m^{-2}, and with 0.1 M of sulphate addition. The model predicted the lowest energy consumption of 138 kJ mol^{-1} under the same condition, while the difference between the experiment and the simulation could be attributed to electrode overpotentials and CO_2 leakage (which were not covered by the model).

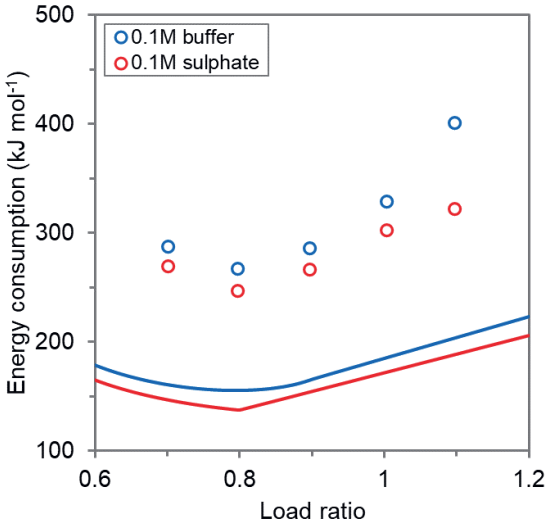

Figure 4.6. Energy consumption under different load ratio with 0.1 M of phosphate buffer or 0.1 M of sulphate added. Symbols (○): experimental data; lines: model simulation results.

Firstly, while phosphate buffer has one buffering zone in the pH range of the acidifying solution, sulphate does not have any buffer capacity. As a result, the pH of acidifying solution under the same L_{K^+} was lower with sulphate addition than with phosphate addition (**Figure 4.7**a). At $L_{K^+} < 0.9$, the lower pH favored the desorption of CO_2 so that the CO_2 production rate was higher with sulphate addition (**Figure 4.7**b). However, when the pH of acidifying solution was lower than 4, the CO_2 yield reached its maximum, and the CO_2 production rate was limited by the total carbon feeding rate. Therefore, the CO_2 production rate was equivalent with different electrolytes addition at $L_{K^+} \geq 0.9$. Secondly, the cell voltage only showed differences at $L_{K^+} > 0.8$ between sulphate addition and phosphate addition (**Figure 4.7**c). As discussed before, the benefit of adding phosphate buffer was primarily to increase the conductivity in the acidifying compartment provided by phosphate. Moreover, sulphate ions have higher molar conductivity comparing to HPO_4^{2-} and $H_2PO_4^-$ (i.e., the main phosphate species in the pH range of the acidifying solution). Furthermore, the impact of the ionic conductivity was higher at high L_{K^+} when the acidifying solution was more depleted. Hence, the ohmic losses originated from the ionic resistance was lower when adding sulphate than with phosphate at $L_{K^+} > 0.8$ (**Figure 4.7**d). The difference in ohmic losses accounted for 23%, 51%, and 16% of the cell voltage difference at $L_{K^+} = 0.9$, 1.0, and 1.1, respectively. The rest of the cell voltage difference between different electrolytes addition could be explained by the boundary effects on the surface of the MEA. On the surface of the acidifying compartment side of the MEA, the K^+ concentration decreased and H^+ concentration increased with higher L_{K^+}, which induced a lower local pH. Driven by the current applied, the anionic species moved towards the surface of the MEA. As discussed before, without the addition of buffer or sulphate, due to the formation of non-conductive H_2CO_3, the boundary layer of the

MEA provided a high potential drop. While H_3PO_4 has a lower pK_a than H_2CO_3 (2.10 vs 6.35), more charged phosphate species ($H_2PO_4^-$/HPO_4^{2-}) could be present at the boundary layer and provide conductivity. Moreover, H_2SO_4, as a strong acid, has a pKa of -2.80, so all the sulphate species at the boundary layer were in charged dissociated form. Therefore, adsorbent with sulphate addition reduced the potential drop at the boundary layer of the MEA, which led to the lower cell voltage.

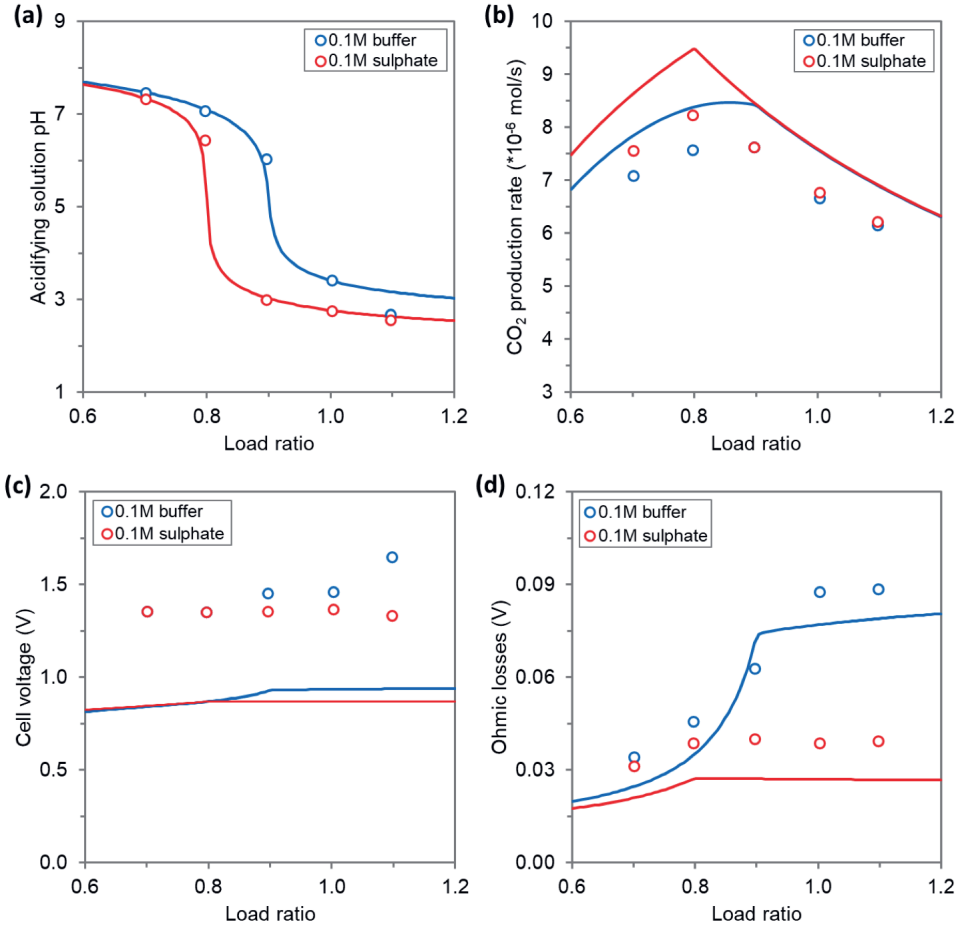

Figure 4.7. Experimental and model simulated results of (a) acidifying solution pH, (b) CO_2 production rate, (c) cell voltage, and (d) ohmic losses under different load ratio with 0.1 M phosphate buffer or 0.1 M sulphate addition. Symbols (○): experimental data; lines: model simulation results.

4.4. Conclusions

In this work, we have shown different strategies to reduce the energy consumption for the electrochemical DAC process by decreasing the CO_2 desorption pressure and adding background electrolyte. When the CO_2 partial pressure at the gas phase of the membrane contactor

was reduced from 0.9 to 0.3 atm, the energy consumption of the process decreased 12 to 15% among the three tested conditions. The applied partial vacuum increased the CO_2 production rate by increasing the driving force for CO_2 desorption from liquid to gas and decreased the cell voltage by diminishing gas bubbles in the electrochemical cell. Moreover, the addition of 0.1 and 0.2 M of phosphate changed the optimum L_{K^+}, where we observed the lowest energy consumption at L_{K^+} = 0.8 with 0.1 M buffer. The addition of the phosphate buffer increased the conductivity of both the acidifying solution and the boundary layer of the MEA, so the cell voltage decreased with more buffer added. However, the CO_2 production rate was limited by either the total carbon feeding rate with higher buffer concentration at fixed influent K^+ concentration or a higher acidifying solution pH with higher buffer concentration at fixed total carbon feeding rate. Finally, because of the low pKa and high molar conductivity of sulphate comparing to phosphate, 0.1 M sulphate addition showed lower energy consumption than 0.1 M phosphate addition at the same L_{K^+}. Among all the investigated conditions, the lowest energy consumption was 247 kJ mol^{-1} achieved at $p_{CO_2,g}$ = 0.3 atm, L_{K^+} = 0.8, j_c = 150 A m^{-2} with 0.1 M of sulphate addition, while the model predicted the minimum of 138 kJ mol^{-1} under the same condition. The experimental lowest energy consumption of this work is 34% lower comparing to our previous work, which makes this electrochemical process more competitive among all the DAC technologies.

Supporting Information

Influent preparation

Experiments were performed using influents with different potassium and total carbon concentrations. The influent solutions resembled a spent potassium hydroxide absorbent solution, with and without a background electrolyte, which was in equilibrium with ambient air. The compositions of influents were calculated by considering the Henry's law, the equilibrium of carbonate, phosphate and water dissociation, and electroneutrality. The detailed compositions of all the influent solutions are listed in **Table S4.1**.

Table S4.1. Composition of absorbent solutions with different amount of phosphate/sulphate and their corresponding spent solutions. The influents for experiments were the spent absorbent solutions.

Absorbent	Spent absorbent (influent)	Influent K^+ concentration (M)	Total carbon concentration (M)
1 M KOH	0.224 M $KHCO_3$ 0.388 M K_2CO_3	1.0	0.612
0.8 M KOH 0.1 M K_2HPO_4	0.197 M $KHCO_3$ 0.300 M K_2CO_3 0.098 M K_2HPO_4 0.002 M K_3PO_4	1.0	0.497
0.6 M KOH 0.2 M K_2HPO_4	0.167 M $KHCO_3$ 0.215 M K_2CO_3 0.197 M K_2HPO_4 0.003 M K_3PO_4	1.0	0.382
0.6 M KOH 0.2 M K_2HPO_4	0.167 M $KHCO_3$ 0.215 M K_2CO_3 0.197 M K_2HPO_4 0.003 M K_3PO_4	1.0	0.382
1M KOH 0.1 M K_2HPO_4	0.224 M $KHCO_3$ 0.388 M K_2CO_3 0.098 M K_2HPO_4 0.002 M K_3PO_4	1.2	0.612
1M KOH 0.2 M K_2HPO_4	0.224 M $KHCO_3$ 0.388 M K_2CO_3 0.196 M K_2HPO_4 0.003 M K_3PO_4	1.4	0.612
0.8 M KOH 0.1 M K_2SO_4	0.197 M $KHCO_3$ 0.301 M K_2CO_3 0.100 M K_2SO_4	1.0	0.498

Effect of phosphate buffer on cell performance

We have performed experiments with different amount of phosphate buffer addition at fixed influent K^+ concentration of 1 M and L_{K^+} ranging from 0.7 to 1.1. **Table S4.2** listed the conductivity and K^+ concentration of both the acidifying solution and the catholyte.

Table S4.2. Measured conductivity and K^+ concentration of both the acidifying solution and the catholyte in the experiments with different amount of phosphate buffer addition under varying L_{K^+}.

Buffer addition	L_{K^+}	Acidifying solution		Catholyte	
		Conductivity (mS cm^{-1})	K^+ concentration (M)	Conductivity (mS cm^{-1})	K^+ concentration (M)
None	0.7	28.33	0.34	124.92	1.04
	0.8	24.46	0.26	134.99	1.07
	0.9	17.87	0.19	155.97	1.06
	1.0	8.39	0.08	185.87	1.10
	1.1	0.14	0.00	203.88	1.20
0.1 M phosphate	0.7	26.60	0.30	127.32	1.05
	0.8	18.58	0.23	144.54	1.06
	0.9	12.95	0.14	156.73	0.95
	1.0	9.04	0.10	160.98	1.10
	1.1	8.95	0.10	159.52	1.08
0.2 M phosphate	0.7	25.16	0.31	110.67	0.99
	0.8	22.44	0.29	114.93	0.98
	0.9	15.69	0.20	117.30	0.93
	1.0	15.12	0.19	117.60	1.04
	1.1	14.70	0.17	115.68	0.98

The anode overpotential (η_{anode}) was determined by the difference between measured anode potential ($E_{anode,measured}$) and the calculated anode potential (E_{anode}) based on actual conditions:

$$\eta_{anode} = E_{anode,measured} - E_{anode} \quad \text{(S4.1)}$$

$$E_{anode} = E^0_{anode} - \frac{R\,T}{z\,F}\ln\left(\frac{pH_2}{[H^+]^2}\right) \quad \text{(S4.2)}$$

Where E^0_{anode} is the standard anode potential (-0.244 V vs SCE), pH_2 is the hydrogen partial pressure at anode (0.95 atm, considering 5% CO_2 leaked from acidifying compartment), and $[H^+]$ equals to 0.54 M based on a fully saturated Nafion membrane.

The cathode overpotential ($\eta_{cathode}$) was determined by the difference between the calculated cathode potential ($E_{cathode}$) based on actual conditions and measured cathode potential ($E_{cathode,measured}$):

$$\eta_{cathode} = E_{cathode} - E_{cathode,measured} \quad \text{(S4.3)}$$

$$E_{cathode} = E^0_{cathode} - \frac{R\,T}{z\,F} \ln\left(pH_2\,[OH^-]^2\right) \quad \text{(S4.4)}$$

Where $E^0_{cathode}$ is the standard cathode potential (-1.072 V vs SCE), pH_2 is the hydrogen partial pressure at cathode (0.7 atm), and $[OH^-]$ is the concentration of OH^- (M) in catholyte calculated from measured pH.

The ohmic losses (E_{ohmic}) are calculated based on eq. 4.18 of the article, where σ_a and σ_c are the measured conductivities of the acidifying solution and catholyte (S m^{-1}), respectively.

Table S4.3 listed the results of electrode overpotentials and ohmic losses of the experiments performed with phosphate buffer addition.

Table S4.3. Experimental results of electrode overpotentials and ohmic losses in the experiments with different amount of phosphate buffer addition under varying L_{K^+}.

Buffer addition	L_{K^+}	η_{anode} (V)	$\eta_{cathode}$ (V)	E_{ohmic} (V)
None	0.7	0.17	0.30	0.03
	0.8	0.28	0.24	0.04
	0.9	0.32	0.23	0.05
	1.0	0.29	0.22	0.09
	1.1	1.92	0.41	5.53
0.1 M phosphate	0.7	0.14	0.26	0.03
	0.8	0.14	0.25	0.05
	0.9	0.38	0.22	0.06
	1.0	0.17	0.25	0.09
	1.1	0.26	0.24	0.09
0.2 M phosphate	0.7	0.18	0.27	0.04
	0.8	0.19	0.25	0.04
	0.9	0.20	0.26	0.05
	1.0	0.13	0.26	0.06
	1.1	0.14	0.26	0.06

Chapter 5

Process layouts and parameters impacting electrochemical direct air capture process

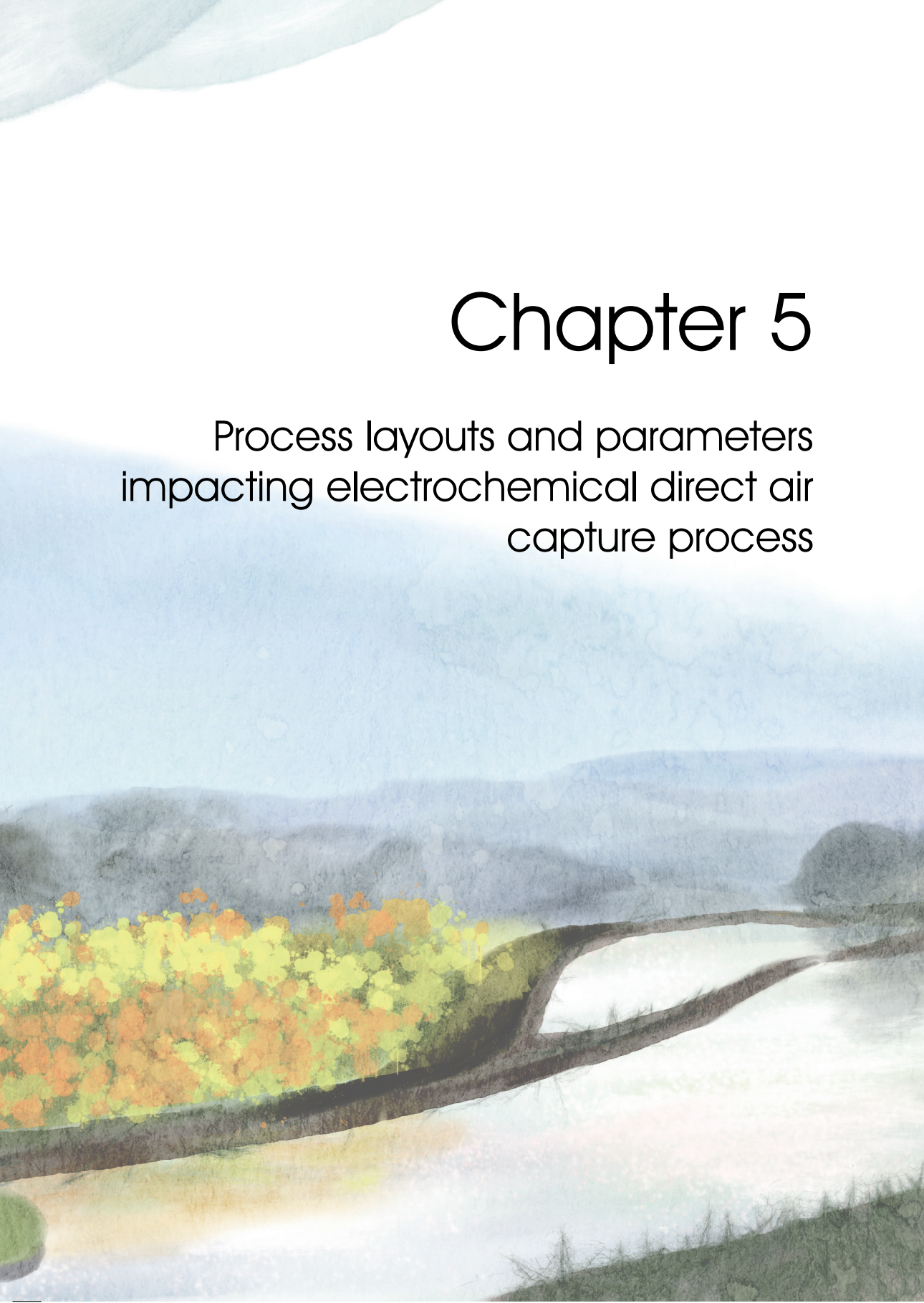

Abstract

Electrochemical techniques have been recently proposed as promising alternative regeneration methods for direct air capture (DAC). In this work, we investigated the effects of various process layouts and operating conditions on the performance of an electrochemical regeneration of an alkaline absorption DAC process using a mathematical model. Based on our model predictions, the circulation of solution in each compartment is crucial to reduce the negative effects of gas bubbles. The energy consumption dropped by 20% with the recirculation ratio increased from 5 to 10. However, with reduced gas bubble resistance, this benefit became less impactful at even higher recirculation ratio, and the higher recirculation ratio also increased the investment in pumping energy. Moreover, the energy consumption of the process can be reduced with a lower current density or a higher concentration of SO_4^{2-} as background electrolyte. However, the tradeoffs with CO_2 production rate and CO_2 capture capacity of the absorbent need to be considered when choosing the optimal operating parameters. Furthermore, three process layouts were simulated to explore the benefits of external versus internal CO_2 desorption. A 2-unit external desorption layout was identified as the most energy efficient option across a wide range of operating conditions, as it had a high desorption efficiency and a low CO_2 gas void fraction in the cell. Among all the investigated conditions, the lowest energy consumption achieved was 128 kJ mol^{-1} CO_2, which made this technology a promising candidate for DAC absorbent regeneration.

5.1. Introduction

The burning of fossil fuels and other anthropogenic activities have significantly increased the concentration of greenhouse gases (GHGs) including CO_2 in the atmosphere.[2,3] From 2010 to 2019, annual GHG emissions reached the highest levels in human history, and current efforts to reduce emissions have not been sufficient to meet the target of limiting global warming to 1.5°C as set by the Paris Agreement.[12,13] To tackle the rapid climate change caused by increasing atmospheric CO_2 concentration, immediate action is required, including the implementation of direct air capture (DAC) technologies.[41,106] DAC is a process that captures atmospheric carbon dioxide (CO_2) and produces high-purity CO_2 for consequent storage or utilization, and it can help counterbalance hard-to-eliminate emissions and achieve net-zero CO_2 emissions.[35] The most studied DAC technologies involve the use of chemical sorbents, such as strongly alkaline solution or amine, to capture CO_2 from the air.[107] The atmospheric CO_2 is captured by the sorbents spontaneously at ambient temperature, while the sorbents regeneration is energy intensive and can require high temperatures >100°C. Although such temperature swing processes allow for high CO_2 capture efficiency, they suffer from a variety of challenges due to the high-temperature thermal regeneration, e.g., sorbent degradation, volatility, and toxicity of the thermal degradation compounds.[167–170] In recent years, electrochemical regeneration of DAC processes has attracted increasing research attentions,[46–48,171–173] due to the applied moderate operating conditions of ambient temperature and the ability for directly integration with renewable energy.

In our previous work, we demonstrated the use of an electrochemical system to simultaneously regenerate spent alkaline absorbent and desorb high-purity CO_2 (**Figure 5.1**).[117] The spent alkaline absorbent is the effluent of the CO_2 absorption unit that contains carbonate (CO_3^{2-}) and bicarbonate (HCO_3^-) ions, which is fed into an electrochemical cell as influent. In the electrochemical system, H_2 is oxidized at the anode (hydrogen oxidation reaction, HOR), and the spent solution is first acidified in the acidifying compartment by the H^+ migrated from anode to facilitate the desorption of CO_2 gas according to the displacement of the CO_2 equilibria. After separating the desorbed CO_2 from the solution using a membrane contactor, the solution is alkalinized in the cathode compartment where OH^- ions are produced by water reduction (hydrogen evolution reaction, HER). The alkalinized solution leaves the system as effluent and can be reused as absorbent for DAC. Hence, based on HOR and HER, a pH swing is established in two adjacent compartments of the electrochemical cell, and CO_2 is desorbed in the acidifying compartment (low pH), while alkaline absorbent is regenerated in the cathode compartment (high pH).

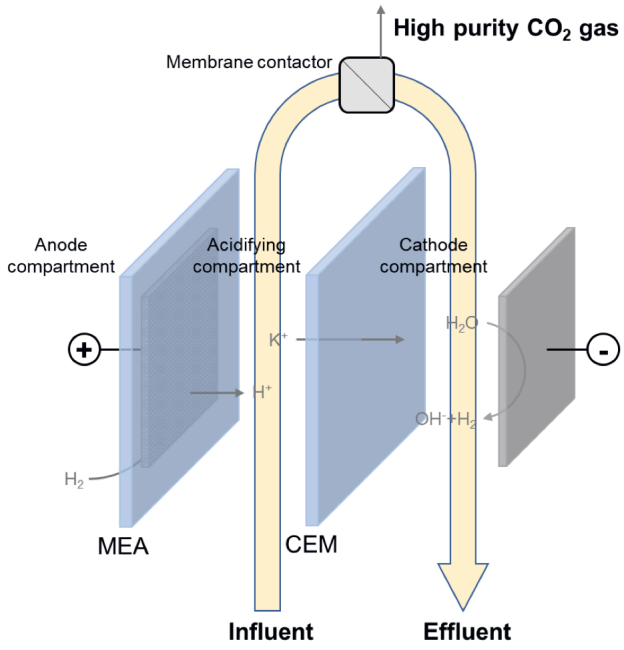

Figure 5.1. Schematic representation of the electrochemical process for the regeneration of alkaline DAC absorbent. Influent: spent alkaline absorbent from the absorber. Effluent: regenerated absorbent to send to the absorber. MEA = membrane electrode assembly, CEM = cation exchange membrane.

The electrochemical regeneration process is a promising technology in terms of performance, safety, reliability, and scalability potential.[117,174] One of the key challenges is to reduce the energy consumption of the system. The energy losses in electrochemical processes involve the negative effects from gas bubbles "trapped" inside the cell, as they provide additional electrical resistance and reduce effective areas of electrodes and membranes.[175–177] Eisaman et al. applied a high pressure on a bipolar membrane electrodialysis (BPMED) cell to eliminate these CO_2 bubbles and reduce energy consumption.[61] However, the high-pressure operation significantly increases the complexity of the system. On the other hand, Valluri and Kawatra have designed a process based on BPMED to produce sulfuric acid (H_2SO_4) and sodium hydroxide (NaOH), where the NaOH was used to capture CO_2 and H_2SO_4 was used to desorb CO_2 by mixing it with the spent alkaline solution.[51] The advantage of this acid-base production process is that the system can be operated under room temperature and atmospheric pressure.

In this study, we propose different process layouts to acidify the spent absorbent and promote the CO_2 evolution at different points of the process (**Figure 5.2**). In particular, we consider three different process layouts in this work: internal (**Figure 5.2**b), 1-unit external (**Figure 5.2**c), and 2-unit external desorption layout (**Figure 5.2**d). While the CO_2 is only desorbed inside the cell in the internal desorption layout, the external desorption layouts have the potential to reduce the CO_2 formation inside the cell by removing it externally. Moreover,

we have added circulation loops for both acidifying and cathode compartments to investigate the effects of the circulation on the performance of the electrochemical cell, as the formed gas bubbles can be removed out of the cell more effectively at higher solution flow rates. Furthermore, as we have shown previously that the addition of background electrolyte in the absorbent reduced the energy consumption of the system, the effects of the background electrolyte concentration are also investigated. Overall, in this study, we developed a mathematical model to investigate different process layouts and operating conditions considering flow rates, applied current densities, and sulphate concentrations (as background electrolyte) in the absorbent. We aim to understand the behavior of the system under different conditions and give direction to further development and application of the technology.

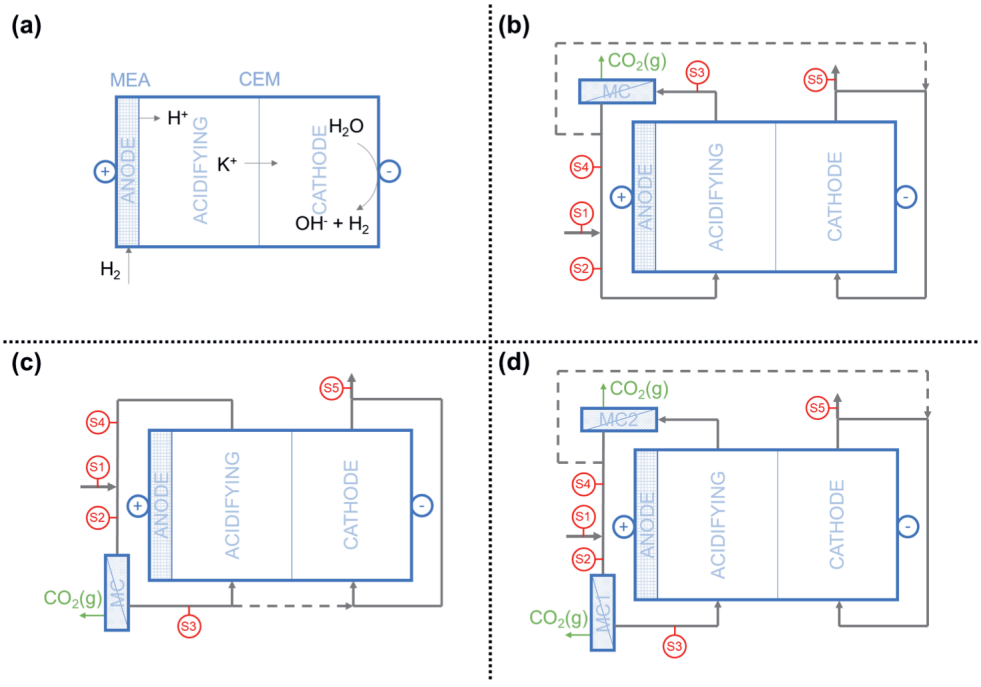

Figure 5.2. (a) Three compartments of the electrochemical cell: anode, acidifying, and cathode compartments. MEA = membrane electrode assembly, CEM = cation exchange membrane. Flow schemes of (b) internal desorption layout, (c) 1-unit external desorption layout, (d) 2-unit external desorption layout. S1 and S5 are the influent (spent alkaline absorbent) and effluent (regenerated alkaline absorbent) of the system, respectively, while S2, S3, and S4 represent different flow streams of the system. The dashed line shows the overflow from acidifying solution circulation to catholyte circulation. MC = membrane contactor.

5.2. Modelling theory background

A mathematical model has been developed to simulate the performance of the electrochemical regeneration system for DAC under thermodynamic equilibria. The electrochemical cell was modelled as a two-phase system (i.e., a liquid and a gas phase), where the liquid phase included both ionic species (K^+, H^+, HCO_3^-, CO_3^{2-}, SO_4^{2-}, and OH^-) and non-charged species

(H_2CO_3 and H_2O). All the species were in equilibrium according to the dissociation constants of H_2CO_3, HCO_3^-, and H_2O, and we assumed that electroneutrality was maintained in the solution. Moreover, the liquid phase of the influent and the acidifying solution was always in equilibrium with the gas phase based on the Henry's law for CO_2, while the catholyte was considered a closed system where the total amount of dissolved carbon species remained constant. The influent solution of the system was the spent alkaline absorbent from the absorption step that was assumed to be in equilibrium with atmosphere (400 ppm CO_2). In the electrochemical cell, CO_2 was desorbed into a gas phase with a CO_2 partial pressure of 0.6 atm (partial vacuum on pure CO_2 gas).

The electrochemical cell consisted of three compartments: anode, acidifying, and cathode compartments (**Figure 5.2**a). H_2 was oxidized at the anode, while H^+ was produced and transported to the acidifying compartment. The faradaic efficiency of the hydrogen oxidation reaction was assumed to be 1. In the acidifying compartment, the spent alkaline absorbent was acidified by the H^+ coming from anode, and the cations in the solution (K^+ and H^+) migrate through the CEM to the cathode compartment. The total flux of cations (J_{tot}) was determined by the applied current density (j_c):

$$J_{tot} = \frac{j_c}{F} = J_{K^+} + J_{H^+} \tag{5.1}$$

where F is the Faraday constant (96485 C mol^{-1}), J_{K^+} and J_{H^+} are the molar fluxes of K^+ and H^+ over the CEM, respectively.

The transport of K^+ and H^+ can be expressed by the Nernst-Planck equation:

$$J_{K^+} = -D_{K^+}\left(\frac{dc_{K^+}}{dx} + c_{K^+,m}\frac{d\phi}{dx}\right) \tag{5.2}$$

$$J_{H^+} = -D_{H^+}\left(\frac{dc_{H^+}}{dx} + c_{H^+,m}\frac{d\phi}{dx}\right) \tag{5.3}$$

where D_{K^+} is the diffusion coefficients of K^+ inside the cation exchange membrane, c_{K^+} is the concentration of K^+ at different positions inside the membrane, $c_{K^+,m}$ is the average concentration of K^+ in the membrane, while D_{H^+}, c_{H^+}, and $c_{H^+,m}$ are the counterparts for H^+, x is the position inside the membrane, and ϕ is the dimensionless electric potential, which can be multiplied by RT/F to obtain the dimensional voltage.

In the internal desorption layout (**Figure 5.2**b), the influent (S1) mixed with the acidifying circulation loop (CO_2 depleted residual stream (S4)) before entering the cell. The mixture (S2) was supplied to the acidifying compartment where the pH of the solution decreased, which facilitated the desorption of CO_2 gas. The outflow from the acidifying compartment (S3) was directed into the membrane contactor where the CO_2 gas was separated from the liquid phase. A part of the CO_2 depleted residual stream (S4) overflowed to the catholyte circulation loop (same flow rate with S1), while the rest of this stream (S4) was recirculated

and mixed with the influent. In the cathode compartment, the catholyte received the cations that migrated through the CEM from the acidifying compartment. As a result, the catholyte had the same total K^+ concentration as the influent. Moreover, H_2O was reduced to H_2 and OH^- at the cathode, and OH^- regenerated the alkalinity of the solution, while H_2 could be recirculated to anode. The catholyte was recirculated at the same rate as the acidifying solution, and the excess solution left the circulation loop as the effluent (S5) of the system (regenerated alkaline absorbent). In this case, the corresponding mass balance of K^+ in the streams was as follows:

$$J_{K^+} = \frac{Q_1}{A} \times \left(c_{K^+,1} - c_{K^+,3}\right) \tag{5.4}$$

$$c_{K^+,2} \times (Q_1 + Q_4) = c_{K^+,1} \times Q_1 + c_{K^+,4} \times Q_4 \tag{5.5}$$

$$c_{K^+,4} = c_{K^+,3} \tag{5.6}$$

$$c_{K^+,5} = c_{K^+,1} \tag{5.7}$$

where $c_{K^+,1}$, $c_{K^+,2}$, $c_{K^+,3}$, $c_{K^+,4}$, and $c_{K^+,5}$ are the K^+ concentration of S1, S2, S3, S4, and S5 respectively, A is the active membrane area, and Q_1 and Q_4 are the flow rates of S1 and S4 respectively. The ratio between Q_4 and Q_1 was defined as the recirculation ratio (λ_r):

$$\lambda_r = \frac{Q_4}{Q_1} \tag{5.8}$$

In the 1-unit external desorption layout (**Figure 5.2**c), after the mixing of the influent (S1) with the outlet of the acidifying compartment (S4), the mixture (S2) first flowed through a membrane contactor to remove the desorbed CO_2 gas, then the degassed solution (S3) partially overflowed into the catholyte circulation loop and partially recirculated back in the acidifying compartment. The excess catholyte (S5) left the system as regenerated alkaline absorbent. As a results, while eqs. 5.4, 5.5, and 5.7 were still valid for the mass balances of K^+, eq. 5.6 changed to the follow:

$$c_{K^+,2} = c_{K^+,3} \tag{5.9}$$

In the 2-unit external desorption layout (**Figure 5.2**d), the influent (S1) blended in the acidifying circulation loop, and the mixture (S2) passed through the first membrane contactor for the first-step CO_2 desorption. The partially degassed solution (S3) flowed into the acidifying compartment where CO_2 was desorbed for the second time. Then we assumed a second membrane contactor was used to remove the desorbed CO_2 gas, and a part of the CO_2 depleted residual stream overflowed to catholyte circulation loop while the rest (S4) remained in the acidifying circulation loop and mixed with the influent. Therefore, eqs. 5.5, 5.7, and 5.9 were applicable for the K^+ mass balances in this case, whereas the molar flux of K^+ (eq. 5.4) should be replaced by:

$$J_{K^+} = \frac{Q_1}{A} \times \left(c_{K^+,1} - c_{K^+,4}\right) \tag{5.10}$$

The total amount of CO_2 desorbed was determined by the difference between the total carbon concentrations in the inlet and the outlet of the acidifying circulation loop. Hence, the CO_2 production rate (J_{CO_2}) for internal desorption and 2-unit external desorption layouts can be calculated by eq. 5.11, while the CO_2 production rate for 1-unit external desorption was expressed by eq. 5.12.

$$J_{CO_2} = \frac{Q}{A} \left(c_{C,1} - c_{C,4}\right) \tag{5.11}$$

$$J_{CO_2} = \frac{Q}{A} \left(c_{C,1} - c_{C,3}\right) \tag{5.12}$$

where $c_{C,1}$, $c_{C,3}$, and $c_{C,4}$ are the total carbon concentration in S1, S3, and S4, respectively.

The CO_2 bubbles formed inside the acidifying compartment contribute to the electrical resistance of the cell. In the internal desorption layout, all the CO_2 evolution occurred inside the acidifying compartment. In the 1-unit and 2-unit external desorption layout, CO_2 evolution occurred first at the mixing point of the influent (S1) and the acidifying circulation loop (S4), then more CO_2 bubbles were formed in the acidifying compartment when the solution was further acidified. The amount of the bubbles formed was determined by the flow rate of the stream flowing through the acidifying compartment and the total carbon concentration difference in the compartment. To include the bubble effects on the electrical resistance of the cell, the conductivity of the solution inside the acidifying compartment was corrected using Bruggeman (eq. 5.13, for ϵ = 0 – 0.12) and Maxwell (eq. 5.14, for ϵ > 0.12) equations[178]:

$$\frac{\sigma_a}{\sigma_{a,0}} = (1 - \epsilon)^{1.5} \tag{5.13}$$

$$\frac{\sigma_a}{\sigma_{a,0}} = \frac{1-\epsilon}{1+\frac{\epsilon}{2}} \tag{5.14}$$

where $\sigma_{a,0}$ is the conductivity of the acidifying solution without gas bubbles, σ_a is the corrected conductivity considering the bubble effects, ϵ is the gas void fraction. $\sigma_{a,0}$ is calculated using OLI Studio: Stream Analyzer (ver. 10.0, OLI Systems, NJ, USA) based on the composition of the acidifying solution. Here, we defined the gas void fraction (ϵ) as the volume fraction of CO_2 gas in the stream flowing through the acidifying compartment:

$$\epsilon = \frac{V_g}{V_g + V_l} \tag{5.15}$$

where V_g and V_l are the volume of CO_2 gas bubbles and liquid stream, respectively. V_g is calculated based on the total carbon concentration difference in the inlet and outlet of the acidifying compartment.

A similar approach has been taken to correct the conductivity for catholyte considering the H_2 gas forming inside the cathode compartment. The eqs. 5.13 – 5.15 were applied to make the correction, where V_g was calculated based on the assumption that each two electrons transferred formed one H_2.

The energy consumption (EC) of the electrochemical system was calculated as the ratio between the power input and the CO_2 production rate:

$$EC = \frac{E_{cell}\, j_c}{J_{CO_2}} \tag{5.16}$$

where E_{cell} is the cell voltage which is defined as the sum of the equilibrium potential (E_{eq}), membrane potential (E_m), and ohmic losses (E_{ohmic}).

E_{eq} is the potential drop originated the pH difference between the anode (pH_{anode}) and cathode ($pH_{cathode}$) considering a potential drop of 59.2 mV for each pH unit:

$$E_{eq} = 0.0592\ (pH_{cathode} - pH_{anode}) \tag{5.17}$$

where pH_{anode} is the pH at the membrane electrode assembly which is assumed to be 0.27 based on a fully saturated Nafion membrane,[98] while $pH_{cathode}$ equals to the pH of the effluent of the catholyte circulation loop (S5).

E_m is the potential drop over the CEM caused by the difference of the K^+ concentration in the acidifying solution ($c_{K^+,a}$) and catholyte ($c_{K^+,c}$):

$$E_m = \frac{R\,T}{F} \ln \frac{c_{K^+,c}}{c_{K^+,a}} \tag{5.18}$$

where R is the ideal gas constant, T is the temperature.

E_{ohmic} is derived from the ohmic resistance of the acidifying solution and catholyte:

$$E_{ohmic} = j_c \left(\frac{d_a}{\sigma_a} + \frac{d_c}{\sigma_c}\right) \tag{5.19}$$

where d_a and d_c are the thicknesses of the acidifying and cathode compartments, respectively, and σ_c is the conductivity of the catholyte.

With a defined design of the electrochemical cell, the performance of the system is determined by the concentration of K^+ in the influent, influent flow rate, and the applied current density. Therefore, we defined a control parameter "K^+ load ratio" (L_{K^+}) to investigate the behavior of the electrochemical cell:

$$L_{K^+} = \frac{j_c A}{c_{K^+,1} Q_1 F} \tag{5.20}$$

where A is fixed at 0.01 m^2 in all the simulations, and $c_{K^+,1}$ is fixed at 1 M.

5.3. Modelling results and discussion

5.3.1. Effects of recirculation ratio

We first investigated the effects of recirculation ratio on the performance of the 1-unit external desorption layout with fixed current density of 200 A m^{-2} and sulphate concentration of 0.1 M. The energy consumption of the electrochemical cell was reduced with a higher recirculation ratio (**Figure 5.3**a). The reduction of energy consumption was primarily attributed to the difference in CO_2 production rate at high L_{K^+} and internal resistance from gas bubbles at low L_{K^+}.

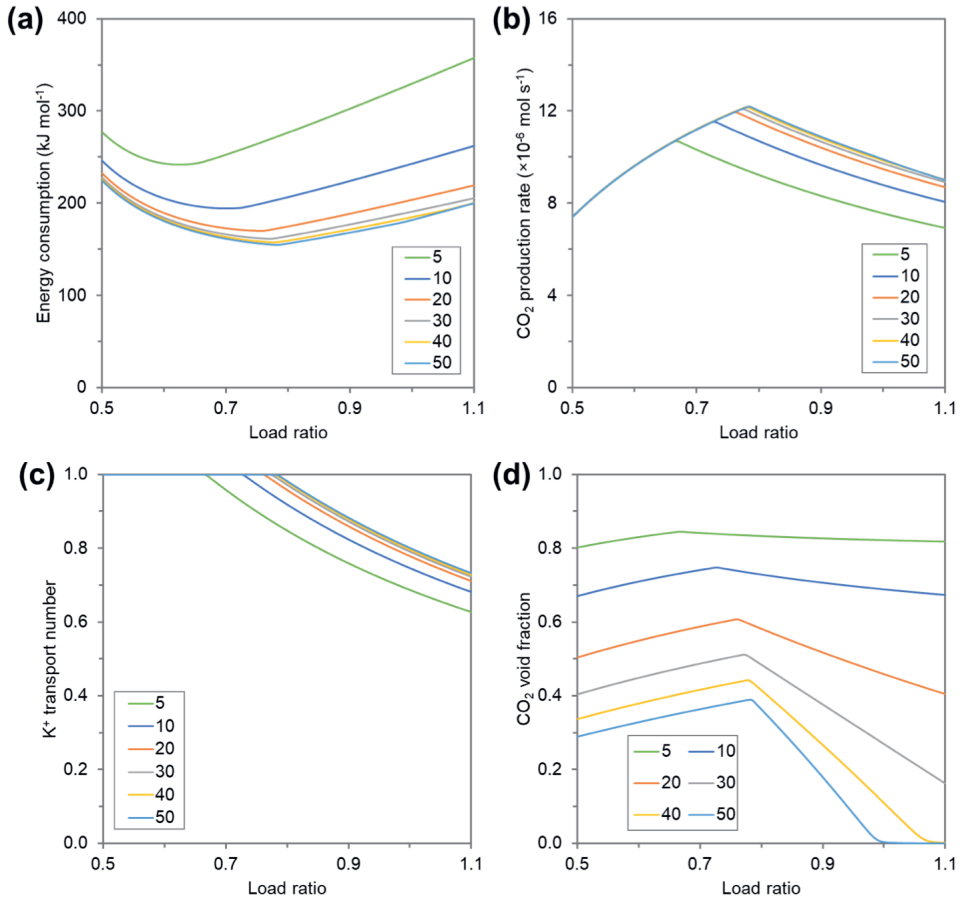

Figure 5.3. Model predictions of process performance for 1-unit external desorption layout at different recirculation ratio (5, 10, 20, 30, 40, and 50). Current density: 200 A m^{-2}, sulphate concentration: 0.1 M. (a) Energy consumption of the electrochemical cell; (b) CO_2 production rate; (c) K^+ transport number; (d) CO_2 void fraction in the acidifying compartment.

In the acidifying compartment, K^+ was replaced by H^+, so the CO_2 equilibria displaced towards the formation of H_2CO_3 that could be desorbed as CO_2 gas. The CO_2 production rate increased with higher L_{K^+} until all the carbon species in the solution were H_2CO_3, and further increase of L_{K^+} limited the loading rate of total carbon in the influent, which led to a decline of the CO_2 production rate (**Figure 5.3**b). The CO_2 production rate reached a higher maximum value with a higher recirculation ratio, which could be explained by the lower pH of the mixed solution of the influent and the acidifying circulation (**Figure S5.1**). The difference in CO_2 production rate was also reflected by the change of K^+ transport number (**Figure 5.3**c) that was defined as the ratio of K^+ transport to the total cation (K^+ and H^+) transport over the CEM. When only K^+ was transported over the CEM to carry the current, all the H^+ migrated into the acidifying compartment contributed to covert HCO_3^-/CO_3^{2-} to desorb CO_2 gas.

However, when the concentration of H^+ in the acidifying compartment was high enough, H^+ was also transported over the CEM to cathode compartment, which led to a decrease of K^+ transport number. The transport of H^+ was unwanted, as it did not favor the desorption of CO_2 gas. Therefore, we observed the decline of CO_2 production rate when K^+ transport number started to decrease. Moreover, with a faster circulation of the acidifying solution, the formed CO_2 gas bubbles were carried out of the cell by a larger flow of the solution. Hence, as shown in **Figure 5.3**d, the CO_2 void fraction was lower with a higher recirculation ratio, which resulted in a lower ohmic resistance in the electrochemical cell that further decreased the energy consumption. Finally, the effects on both CO_2 production rate and the CO_2 void fraction became less significant with increased recirculation ratio. Overall, the energy consumption dropped by 20% when the recirculation ratio increased from 5 to 10, while this reduction was only 2% when the recirculation ratio increased from 40 to 50.

For 2-unit external desorption and internal desorption layouts, the recirculation ratio only had an impact on the CO_2 void fraction (**Figure S5.2**a), as the CO_2 production rate remained constant with varying recirculation ratios (**Figure S5.2**b). Generally, the total amount of CO_2 production in the system is determined by the difference of total carbon in the influent and in the overflow solution from acidifying circulation to catholyte circulation. In the 2-unit external desorption and internal desorption layouts, the overflow solution had the same composition as S4, while the overflow solution in the 1-unit external desorption layout had the composition as S3. The discrepancy of K^+ concentration in the overflow solutions defined the difference of the CO_2 production rate in the different layouts. Moreover, in the 1-unit external desorption layout, the CO_2 gas evolved in the acidifying compartment was retained in a closed system before mixing with the influent. After the mixing, due to the increase of pH and K^+ concentration in the solution, part of the evolved CO_2 could redissolve in the solution again. As a result, the CO_2 production rate was lower in the 1-unit external desorption layout comparing to the other two layouts, and the difference was minimized with increasing recirculation ratio where the discrepancy of K^+ concentrations in the overflow solution was decreased.

When no circulation of acidifying solution or catholyte was applied (recirculation ration = 1), the energy consumption of the 1-unit external desorption layout was higher than 1 MJ mol^{-1} due to the extremely high CO_2 void fraction (>0.9) (**Figure S5.3**). Therefore, it is crucial for such an electrochemical DAC regeneration system to have recirculation of solutions in each compartment, and the energy consumption of the electrochemical cell decreases with increasing recirculation ratio. However, a higher recirculation ratio with a fixed influent flow rate means more pumping energy investment to recirculate the solution at a faster rate.[179] Hence, the tradeoff between the benefit on the cell energy consumption and the cost on pumping energy needs to be further quantified based on the cell design and the pressure drop over the cell.

5.3.2. Effects of current density

Increased current density has two major effects on the electrochemical cell: higher CO_2 production rate and higher energy consumption. The CO_2 production rate increased linearly with current density under the same L_{K^+}, as the amount of produced H^+ at the anode and the total carbon amount in the influent increased proportionally. Moreover, the change of CO_2 production rate over L_{K^+} remained the same trend with different current densities (**Figure S5.4**). Therefore, according to eq. 5.16, the determining parameter for the energy consumption was the cell voltage. As shown in **Figure 5.4**a, in the 1-unit external desorption layout, the energy consumption increased with current density under the same L_{K^+}. This increase was dominated by the ohmic resistance in the cell where the gas bubble effects played a major role, especially at high current density. For instance, when the CO_2 void fraction reached maximum at L_{K^+} = 0.73 with recirculation ratio of 10 (**Figure 5.4**b), the system reached its minimum energy consumption at 200 A m^{-2}. Nevertheless, due to the more significant impact of gas bubble effects at high current density, at 1000 A m^{-2}, the energy consumption at L_{K^+} = 0.73 was the highest within the L_{K^+} range studied. As demonstrated in the previous section, the energy consumption and CO_2 void fraction were reduced with higher recirculation ratio. It was worth noticing that the CO_2 void fraction could be reduced to almost 0 with recirculation ratio of 50, which implied that the effect of CO_2 gas bubbles in the cell was negligible. Finally, due to the effects of CO_2 gas bubbles, the optimal L_{K^+} for achieving the lowest energy consumption changed with different current densities, which should be carefully considered when choosing the operational parameters in practice.

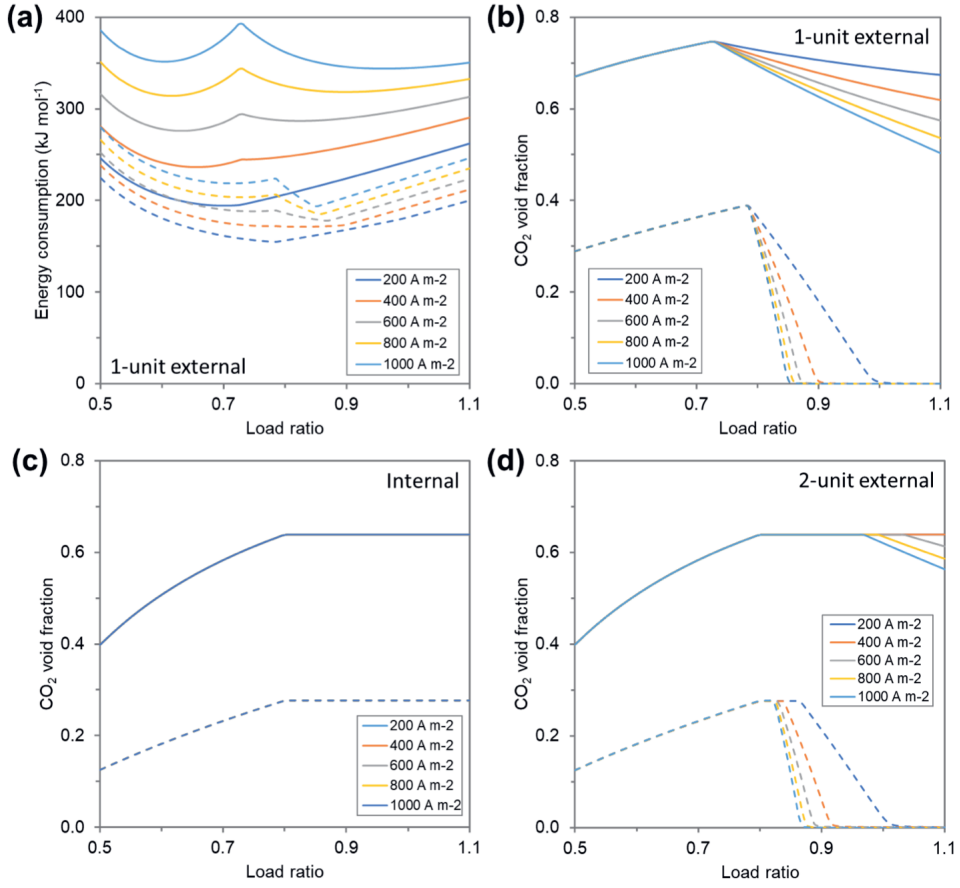

Figure 5.4. Simulated results of system performance indicators with different current densities (200 – 1000 A m^{-2}) and recirculation ratio (10 for solid line and 50 for dashed line). The sulphate concentration was fixed at 0.1 M. (a) Energy consumption of the electrochemical cell with 1-unit external desorption layout; CO_2 void fraction in the acidifying compartment with (b) 1-unit external desorption layout, (c) internal desorption layout, and (d) 2-unit external desorption layout.

In the 1-unit external desorption layout, higher current density resulted in a lower pH of the acidifying solution (S4) at a high L_{K^+} when all the carbon compounds in S4 were in the form of H_2CO_3 (**Figure S5.5**). The lower pH of S4 led to a larger amount of external CO_2 desorption after the mixing of influent and S4. As a result, less carbon remained in the solution after degassing (S3), which limited the amount of internal CO_2 desorption and the CO_2 void fraction in the acidifying compartment. In the internal desorption layout, as all the CO_2 was desorbed inside the acidifying compartment, the CO_2 void fraction did not change with current density (**Figure 5.4**c). The 2-unit external desorption layout showed a mixed CO_2 void fraction behavior of the internal desorption and the 1-unit external desorption layouts that resulted in the lowest CO_2 void fraction among all the layouts (**Figure 5.4**d). At a low L_{K^+}, CO_2 was only desorbed in the acidifying compartment, so the CO_2 void fraction showed

the same behavior as in the internal desorption layout. At a high L_{K^+}, the pH of the acidifying solution (S4) was low enough that CO_2 could also be desorbed after the mixture of the influent and S4 (**Figure S5.5**), then the CO_2 void fraction showed a similar trend as in the internal desorption layout.

Overall, the CO_2 production rate was increased by increasing current density, which is advantageous for large scale application to reduce the capital expenditures of these systems. However, higher current density led to a higher energy consumption due to the ohmic losses in the electrochemical cell. This increase of energy consumption with current density was less significant at higher recirculation ratio, as the gas bubble effects in the cell could be diminished. With external desorption layouts, the effects of CO_2 gas bubbles in the acidifying compartment could be eliminated when all the CO_2 was desorbed externally.

5.3.3. Effects of sulphate concentration

The addition of background electrolytes (SO_4^{2-}) in the absorbent provided additional conductivity to the solution, especially when most of other ions were removed in the acidifying compartment at high L_{K^+}. To investigate the effects of SO_4^{2-} addition to the performance of the system, we have conducted model simulations for different concentrations of SO_4^{2-} addition with fixed K^+ concentration of 1 M under current density of 200 A m^{-2} and recirculation ratio of 10. As shown in **Figure 5.5**a, with increased concentration of SO_4^{2-} addition, the lowest energy consumption of the electrochemical cell was achieved at a lower L_{K^+}: L_{K^+} = 0.70 for 0.1 M SO_4^{2-} addition, L_{K^+} = 0.55 for 0.2 M SO_4^{2-} addition, L_{K^+} = 0.42 for 0.3 M SO_4^{2-} addition, and L_{K^+} = 0.20 for 0.4 M SO_4^{2-} addition. This shift of the optimal L_{K^+} for achieving the lowest energy consumption was primarily due to that the SO_4^{2-} addition changed the CO_2 production rate (**Figure 5.5**b). Since the influent K^+ concentration was fixed at 1 M, the addition of SO_4^{2-} reduced the concentration of HCO_3^-/CO_3^- that limited the amount of total carbon feeding into the electrochemical system and decreased the buffer capacity of the solution. As a result, on the one hand, we observed lower CO_2 production rate with higher concentration of SO_4^{2-} at high L_{K^+} due to the limitation of the total carbon feeding. On the other hand, due to the lower buffer capacity of the influent with more SO_4^{2-} addition, less protons were required to lower the pH, which led to an earlier decrease of K^+ transport number with increasing L_{K^+} (**Figure 5.5**c). As explained previously, the CO_2 production rate was the highest when the K^+ transport number started to decrease from 1. Therefore, with more SO_4^{2-} addition, the peak of CO_2 production rate shifted towards a lower L_{K^+}.

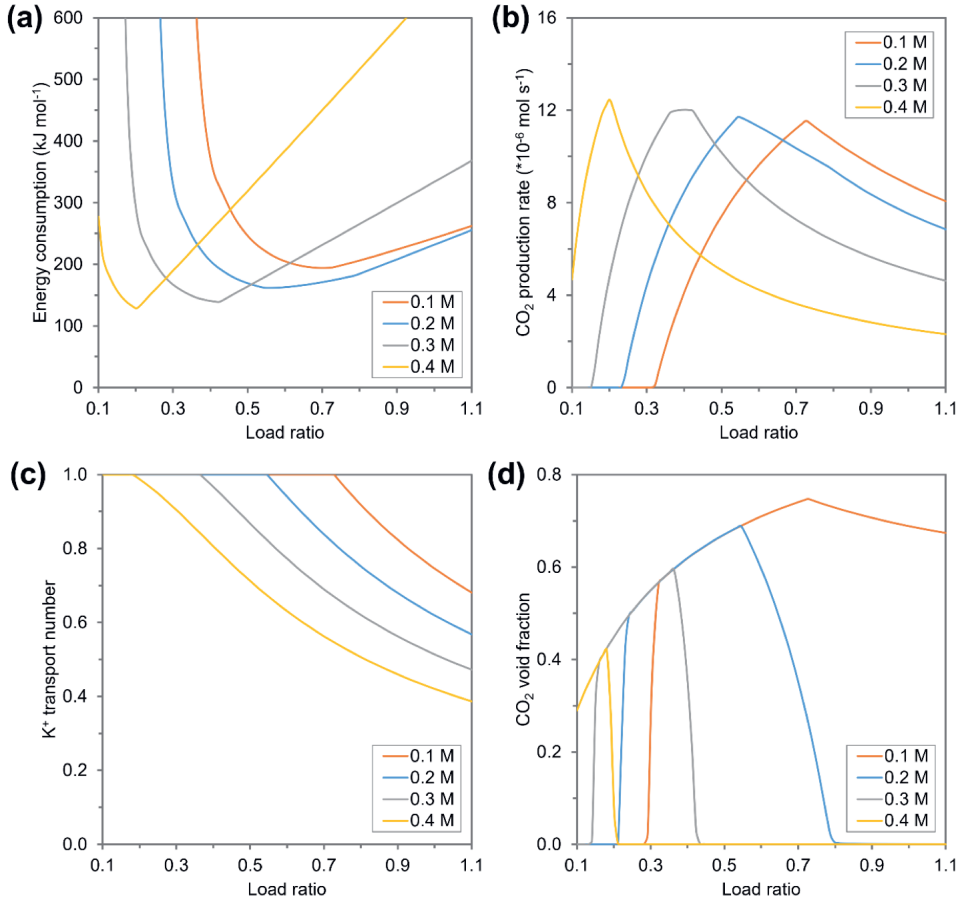

Figure 5.5. Simulated results of system performance indicators for 1-unit external desorption layout with different amount of sulphate addition (0.1 – 0.4 M). The current density was 200 A m^{-2}, while the recirculation ratio was fixed at 10. (a) Energy consumption of the electrochemical cell; (b) CO_2 production rate; (c) K^+ transport number; (d) CO_2 void fraction in the acidifying compartment.

The lowest energy consumption also decreased with more SO_4^{2-} addition (194 kJ mol^{-1} with 0.1 M SO_4^{2-} and 128 kJ mol^{-1} with 0.1 M SO_4^{2-}), which was attributed to the change of CO_2 void fraction in the acidifying compartment. In the 1-unit external desorption layout, as the solution was acidified to a lower pH with more SO_4^{2-} addition, more CO_2 was desorbed externally after mixing of the influent with the acidifying solution, which resulted in less bubble formation in the cell. Moreover, as the peak of CO_2 production rate was achieved at lower L_{K^+} with more SO_4^{2-} addition, the influent flow rate was higher under this condition. While the highest CO_2 production rate with different concentration of SO_4^{2-} addition remained similar, a higher flow rate of acidifying solution resulted in a lower CO_2 void fraction. Therefore, the CO_2 void fraction was significantly reduced with increasing SO_4^{2-} concentration (**Figure 5.5**d), which led to the reduction of energy consumption.

As shown in **Figure 5.6**a, the minimum energy consumption of the system in all the process layouts was reduced with the increase of SO_4^{2-} concentration from 0.1 to 0.2 M. Same as in the 1-unit external desorption layouts, this decrease of energy consumption was ascribed to the changes of both CO_2 production rate and CO_2 void fraction. The maximum CO_2 production rate for each layout was achieved at a lower L_{K^+} with a higher SO_4^{2-} concentration (**Figure 5.6**b). With 0.2 M SO_4^{2-} addition, the 1-unit external desorption layout benefited from lower pH of the acidifying solution that led to more desorption of CO_2 externally. Thus, we observed that the CO_2 production rate of 1-unit external desorption layout reached the same level as the other two layouts at $L_{K^+} > 0.80$. Moreover, the low CO_2 void fraction for external desorption layouts contributed to the lower energy consumption with 0.2 M SO_4^{2-} addition at high L_{K^+} comparing to internal desorption layout (**Figure S5.6**).

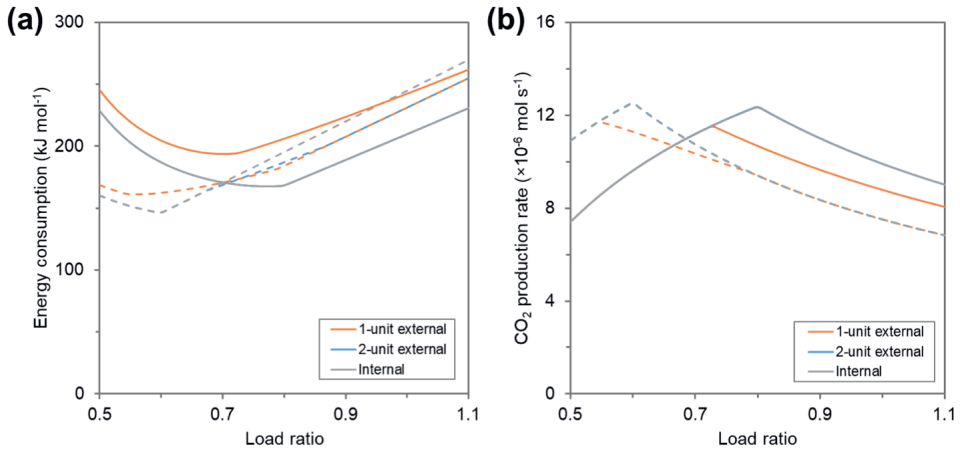

Figure 5.6. Simulated results of system performance indicators for different process layouts with different amount of sulphate addition (solid line: 0.1 M, dashed line: 0.2 M). The current density was 200 A m^{-2}, while the recirculation ratio was fixed at 10. (a) Energy consumption of the electrochemical cell; (b) CO_2 production rate. The energy consumption of internal and 2-unit external desorption layouts overlap with each other at sulphate concentration of 0.1 M, while the CO_2 production rate of these two layouts are identical with each other for both sulphate concentrations. The energy consumption of 2-unit external desorption layout at sulphate concentration of 0.2 M overlaps with internal desorption layout at $L_{K^+} < 0.68$ and overlaps with 1-unit external desorption layout at $L_{K^+} > 0.86$.

Generally, adding more SO_4^{2-} resulted in a shift of the optimal L_{K^+} to a lower value and reduced the lowest energy consumption for the electrochemical cell. Moreover, for external desorption layouts, CO_2 void fraction could be eliminated under a low recirculation ratio and a low current density. With a high concentration of SO_4^{2-} and a high L_{K^+}, the function of the electrochemical cell was to produce acid and base, while CO_2 was desorbed by mixing the produced acid with the spent alkaline absorbent. In this way, the operation of the system was approaching the one described by Valluri and Kawatra.[51] However, the addition of SO_4^{2-} reduced the alkalinity of the absorbent, and SO_4^{2-} was not available for CO_2 capture. Thus, the CO_2 capture capacity of the absorbent was reduced with more SO_4^{2-} addition, which

required a larger volume of the absorbent and more pumping energy to maintain the CO_2 capture rate. Therefore, the tradeoff between the absorption and the desorption steps needs further evaluation before choosing an optimal concentration of SO_4^{2-} addition for application.

5.3.4. General perspectives

The model simulation results shed a light on the effects of recirculation ratio, current density, and SO_4^{2-} concentration. The system achieved a low energy consumption when all these parameters together delivered a high CO_2 production rate and a low gas void fraction in the cell. Moreover, the process layouts also had a huge impact on the performance of the system. The internal desorption layout was widely used in electrochemical CO_2 capture processes. [52,117,180] The advantage of this layout was that all the protons produced at anode were used for the desorption of CO_2 gas at the optimal L_{K^+}. However, for large scale applications, the CO_2 bubbles formed in the electrochemical cell increased largely the energy consumption due to the additional resistance. To minimize the bubble effects, a higher circulation flow rates or a higher concentration of SO_4^{2-} addition could be applied, but they required either more pumping energy or loss of CO_2 capture capacity of the absorbent.

The external desorption layouts had the potential to desorb all the CO_2 outside the cell so that the negative effects of CO_2 bubbles were excluded. Nevertheless, the 1-unit external desorption layout was limited by the low CO_2 desorption efficiency as part of the desorbed CO_2 in the acidifying compartment re-dissolved into the solution after the mixture with influent, although this limitation was eliminated when all the CO_2 was desorbed externally. Moreover, the inflow of the acidifying compartment had a lower pH in the 1-unit external desorption layout comparing to the other two layouts (**Figure S5.7**a), which led to a higher concentration of HCO_3^- and a lower concentration of CO_3^{2-} in the solution. Consequently, as the conversion from HCO_3^- to CO_2 required only one H^+ while CO_3^{2-} requires two H^+, more CO_2 could be desorbed in the acidifying compartment with 1-unit external desorption layout at the same L_{K^+}. Thus, the CO_2 void fraction in the acidifying compartment was higher with 1-unit external desorption layout (**Figure S5.7**b), which led to a higher ohmic loss in the cell. This higher energy consumption of the 1-unit external desorption layout comparing to the internal desorption layout was confirmed by our experimental results under multiple current densities (**Figure S5.9**). On the other hand, the 2-unit external desorption layout prevented this re-dissolution of CO_2 by adding one extra desorption unit. Therefore, the 2-unit external desorption layout had the best performance in the widest range of operating conditions. With 2-unit external desorption layout, the lowest energy consumption of all the conditions theoretically investigated was achieved at 138 kJ mol^{-1} CO_2 at L_{K^+} = 0.6, current density of 200 A m^{-2}, recirculation ratio of 50, and 0.2 M sulphate addition.

The developed model can perfectly describe the equilibrium conditions of the electrochemical system. However, it has its limitation on predicting the energy consumption of the system due to an underestimation of potential drops at membrane and electrode surfaces. At

the anode, the possible flooding of the gas diffusion electrode limited the transport of H_2 to the surface of the electrode, which led to an increasing concentration overpotential at higher current density.[181] At the cathode, the formation of H_2 gas bubbles reduced the effective area of the electrode and increased local current density, which increased the cathode overpotential.[182,183] We observed an increasing discrepancy of energy consumption between the experimental and the simulated results with higher current densities (**Figure S5.9**). Future research should focus on integrating these boundary effects into the model to make better prediction on the energy performance of the system.

5.4. Conclusions

In this work, we have performed a theoretical study on an electrochemical alkaline DAC absorbent regeneration process. First, the modeling results provided insights into the effects of recirculation ratio, current density, and SO_4^{2-} concentration on the system. Increasing of the recirculation ratio reduced the electrical energy consumption of the electrochemical cell but resulted in higher pumping energy requirements. While the effects of the recirculation ratio become less significant at higher values, the optimal recirculation ratio is achieved when the tradeoff between the cell energy consumption and the cost on pumping energy is balanced. The increase of current density promoted the CO_2 production rates of the system, which would be favorable for large-scale application. However, the energy consumption of the electrochemical cell also increased at a higher current density. The SO_4^{2-} addition as background electrolyte reduced the energy consumption, and the optimal L_{K^+} to achieve the minimum energy consumption shifted towards lower L_{K^+} value with higher SO_4^{2-} concentration. Nevertheless, the addition of SO_4^{2-} reduced the CO_2 capture capacity of the absorbent, which needs to be considered when choosing the optimal concentration for SO_4^{2-} addition. Moreover, we compared three process layouts to investigate the benefits of desorbing CO_2 externally of the electrochemical cell. The 2-unit external desorption layout combined the benefits of both internal and 1-unit external desorption layouts, making it the most energy-efficient option across a wide range of operating conditions. Among all the investigated conditions, the lowest energy consumption achieved was 128 kJ mol^{-1} CO_2, which makes this technology a promising candidate for DAC absorbent regeneration. Finally, future studies should focus on the quantification of the boundary conditions of the membrane and electrode surfaces to have a better understanding on the practical energy performance of the system.

Supporting Information

Effects of recirculation ratio

The simulated results for the pH of the mixed solution of the influent and the acidifying circulation (S3) in 1-unit external desorption layout are plotted in **Figure S5.1**. The simulation conditions are current density of 200 A m^{-2}, sulphate concentration of 0.1 M, and recirculation ratio varies from 5 to 50.

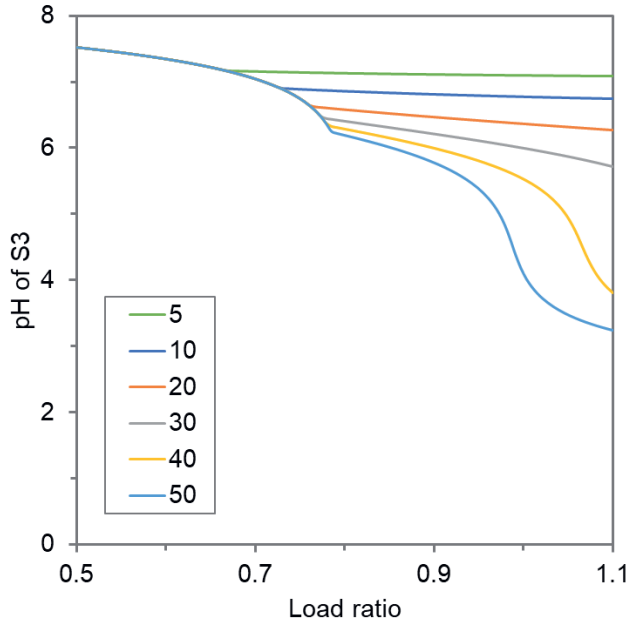

Figure S5.1. Model predictions of the pH of S3 for 1-unit external desorption layout at different recirculation ratio (5, 10, 20, 30, 40, and 50). Current density: 200 A m^{-2}, sulphate concentration: 0.1 M. S3 is the mixed solution of the influent and the acidifying circulation.

The simulated results for the CO_2 void fraction in the acidifying compartment and CO_2 production rate are depicted in **Figure S5.2**. The simulation conditions are current density of 200 A m^{-2}, sulphate concentration of 0.1 M, and recirculation ratio varies from 10 to 50. Noticeably, the CO_2 production rate remained constant with varying recirculation ratios.

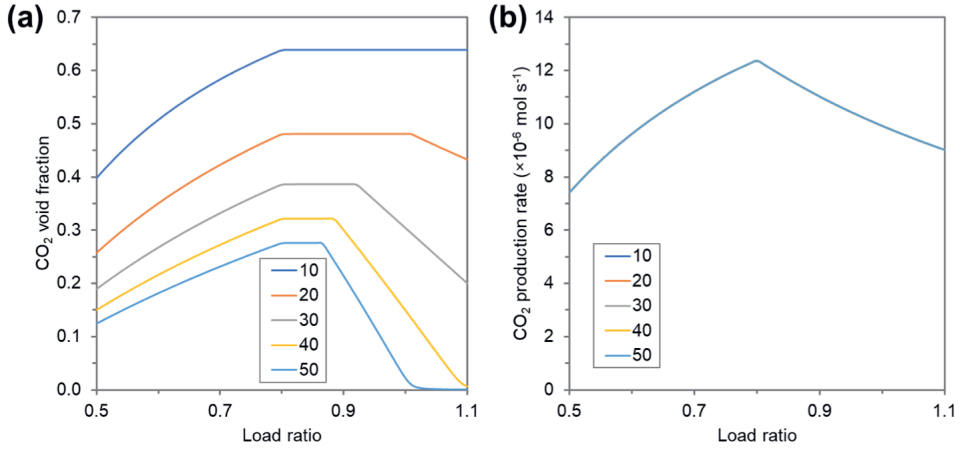

Figure S5.2. Model predictions of process performance for 2-unit external desorption layout at different recirculation ratio (10, 20, 30, 40, and 50). Current density: 200 A m^{-2}, sulphate concentration: 0.1 M. (a) CO_2 void fraction in the acidifying compartment; (b) CO_2 production rate. The CO_2 production rate lines are overlapping with each other.

When the solution in the cell is not actively circulated, the recirculation ratio equals to 1. The simulated energy consumption of the cell at recirculation ratio of 1, current density of 200 A m^{-2}, and sulphate concentration of 0.1 M is shown in **Figure S5.3**.

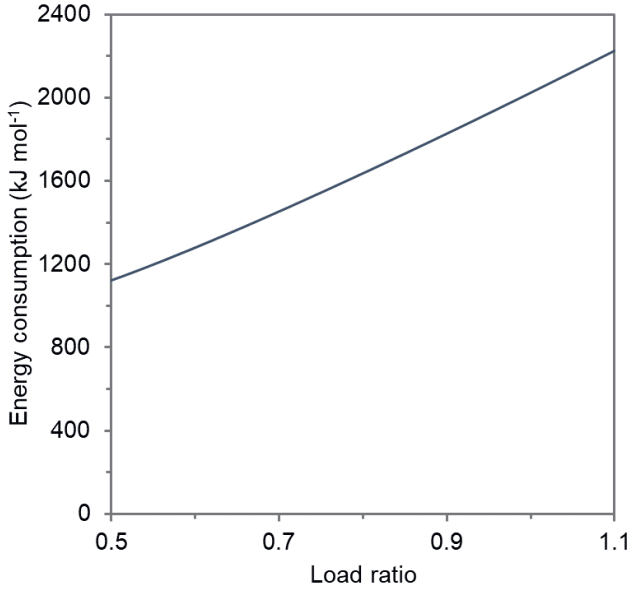

Figure S5.3. Model predictions of the energy consumption for 1-unit external desorption layout at recirculation ratio of 1 (no circulation), current density of 200 A m^{-2}, and sulphate concentration of 0.1 M.

Effects of current density

The simulated results for the CO_2 production rate with varying current densities from 200 to 1000 A m^{-2} in 1-unit external desorption layout are plotted in **Figure S5.4**. The simulation conditions are recirculation ratio of 10 and sulphate concentration of 0.1 M.

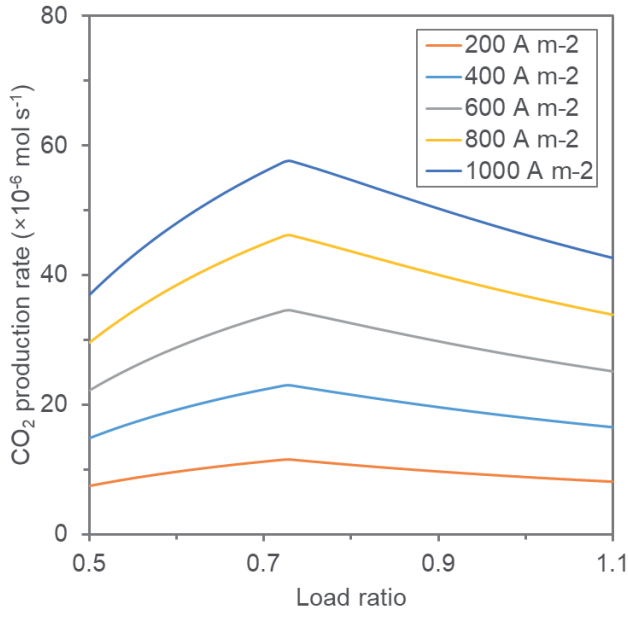

Figure S5.4. Simulated results of the CO_2 production rate for 1-unit external desorption layout with different current densities (200 – 1000 A m^{-2}). Recirculation ratio: 10, sulphate concentration: 0.1 M.

The simulated results for the pH of the acidifying compartment effluent (S4) in 1-unit external desorption layout are plotted in **Figure S5.5**. The simulation conditions are current density of 200 – 1000 A m^{-2}, sulphate concentration of 0.1 M, and recirculation ratio of 10 (**Figure S5.5**a) and 50 (**Figure S5.5**b).

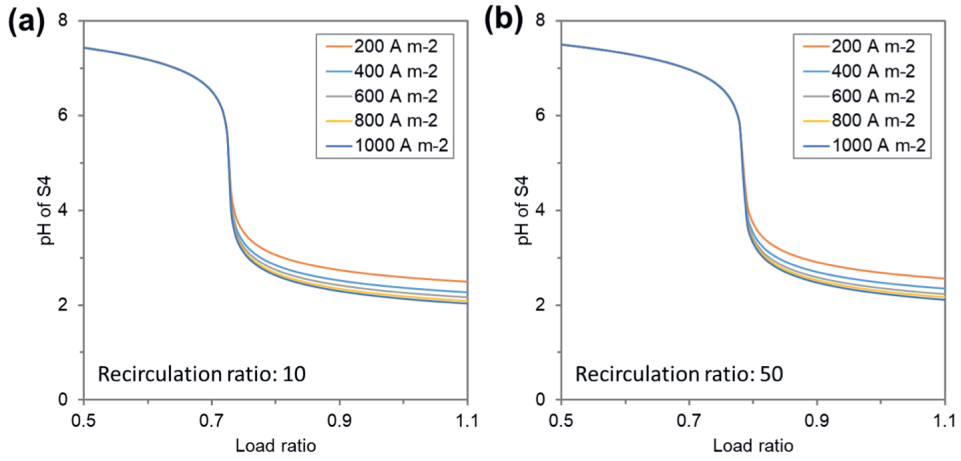

Figure S5.5. Model predictions of the pH of S4 for 1-unit external desorption layout at different current densities (200 – 1000 A m^{-2}). Recirculation ratio: (a) 10, (b) 50, sulphate concentration: 0.1 M. S4 is the effluent of the acidifying compartment.

Effects of sulphate concentration

The simulated results for the CO_2 void fraction in the acidifying compartment of different process layouts with 0.1 M or 0.2 M SO_4^{2-} addition are plotted in **Figure S5.6**. The CO_2 void fractions of the internal and 2-unit external desorption layouts are identical at sulphate concentration of 0.1 M.

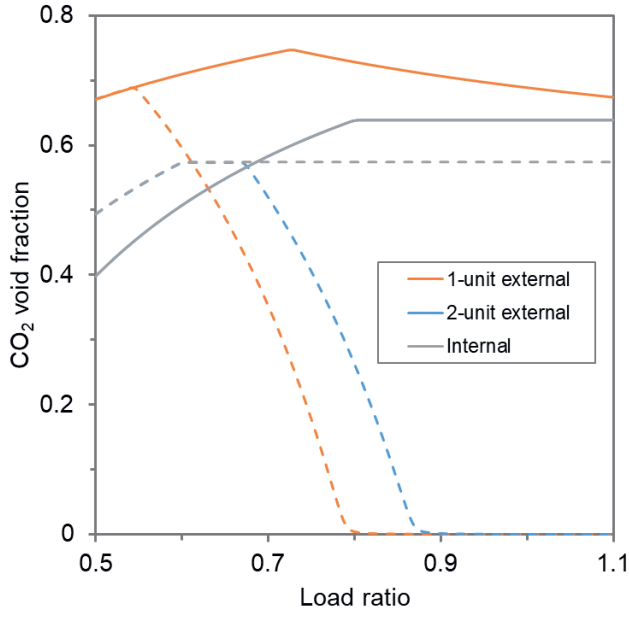

Figure S5.6. Simulated results of the CO_2 void fraction in the acidifying compartment for different process layouts with different amount of sulphate addition (solid line: 0.1 M, dashed line: 0.2 M). The current density was 200 A m^{-2}, while the recirculation ratio was fixed at 10. The CO_2 void fraction of the internal and 2-unit external desorption layouts overlap with each other at sulphate concentration of 0.1 M.

General perspectives

The simulated results for the pH of the acidifying compartment inlet and the CO_2 void fraction in the acidifying compartment in different process layouts are plotted in **Figure S5.7**. The current density was 200 A m^{-2}, the sulphate concentration was 0.1 M, and the recirculation ratio was fixed at 10. The simulation results for internal and 2-unit external desorption layouts were identical for both pH and CO_2 void fraction.

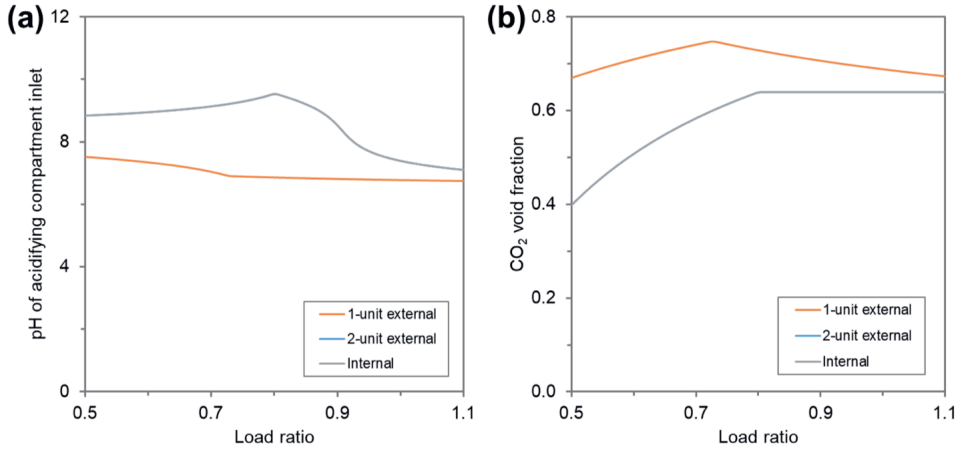

Figure S5.7. Simulated results of (a) the pH of the acidifying compartment inlet (S2 for internal desorption layout, S3 for external desorption layouts) and (b) CO_2 void fraction in the acidifying compartment for different process layouts. The current density was 200 A m^{-2}, the sulphate concentration was 0.1 M, and the recirculation ratio was fixed at 10. The results for internal and 2-unit external desorption layouts (grey line and blue line) are identical for both pH and CO_2 void fraction.

We have designed experiments to compare the performance of the system with either internal or 1-unit external desorption layout. The schematic drawing of the experimental setup is shown in **Figure S5.8**. The materials used in the setup is the same as the ones described in our previous work (Shu et al, Optimization of an electrochemical direct air capture process with decreased CO_2 desorption pressure and addition of background electrolyte, *under review*). To be noted, in the experiments, the circulation flow rate of both the acidifying solution and the catholyte circulation were kept constant at 100 mL min^{-1}. Thus, the recirculation ratio in the experiments was a variable solely dependent on the influent flow rate that was determined by applied current density and L_{K^+}.

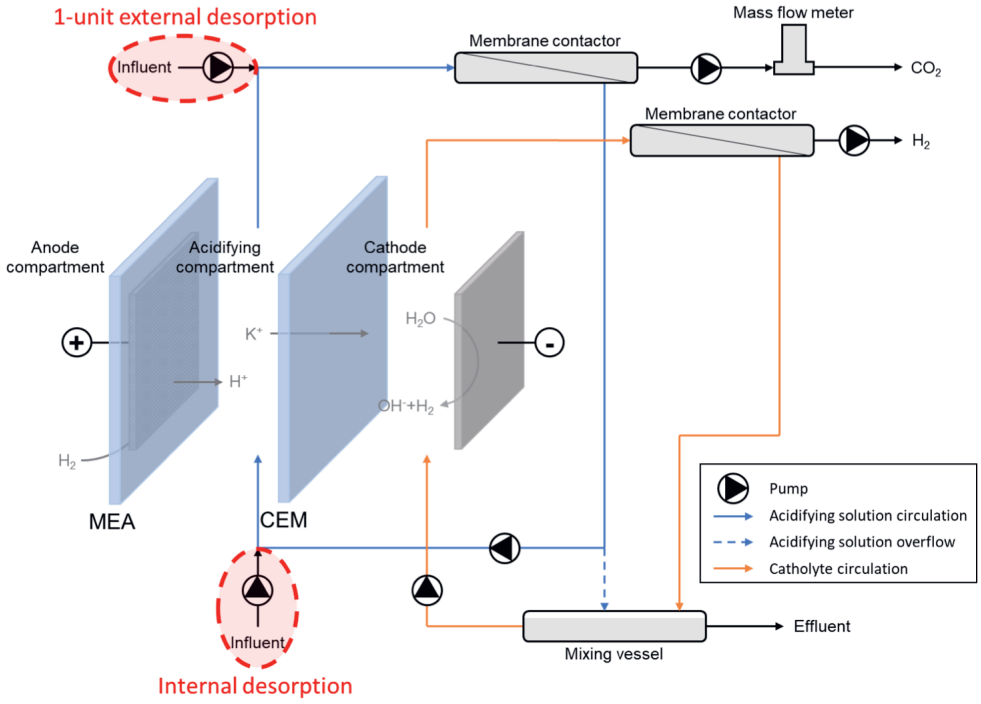

Figure S5.8. Schematic representation of the electrochemical process for the regeneration of alkaline DAC absorbent. Influent: spent alkaline absorbent from the absorber. Effluent: regenerated absorbent to send to the absorber. MEA = membrane electrode assembly, CEM = cation exchange membrane. The influent mixes with the acidifying solution circulation at either highlighted location for internal desorption or 1-unit external desorption layout.

We have performed the experiments with current densities ranging from 200 to 1000 A m^{-2}, while the L_{K^+} remained constant at 0.8 and the sulphate concentration was 0.1 M. The experimental results and the corresponding model simulation results are shown in **Figure S5.9**.

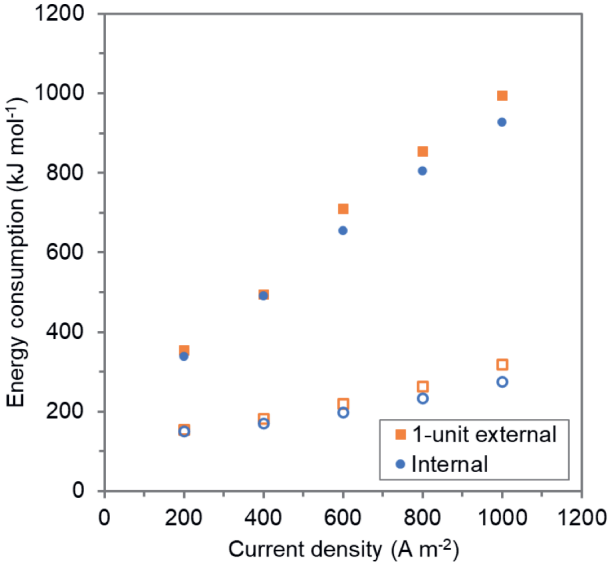

Figure S5.9. Experimental (solid symbols) and simulated (hollow symbols) results with internal and 1-unit external desorption layouts with fixed L_{K^+} = 0.8 under current density ranging from 200 to 1000 A m^{-2}.

Chapter 6

General discussion

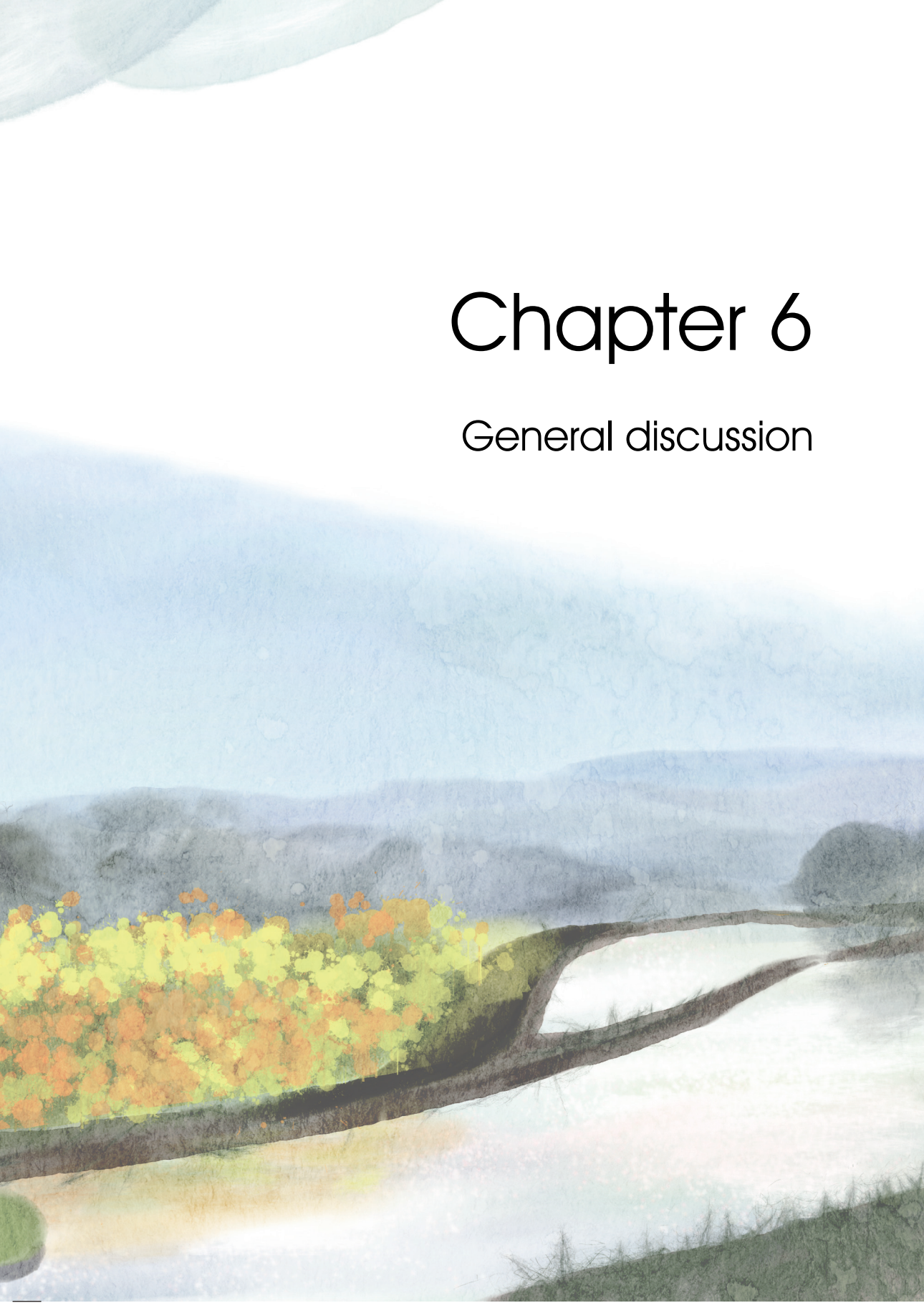

In this thesis, we explored a direct air capture (DAC) process that combined wet scrubbing or solid-sorbent adsorption with a H_2-recycling electrochemical system (HRES) for the regeneration of the sorbents. The focus of this study is on the performance of HRES regeneration system and the integration with the solid-sorbent adsorption step. We demonstrated the proof of concept of the electrochemical system in Chapter 2, the results proved the feasibility of using it for regenerating spent alkaline absorbents from DAC wet scrubbing process. In Chapter 3, we investigated the CO_2 adsorption using electrochemically regenerated anion exchange resins (AERs). The HRES was integrated with an adsorption column packed with AERs, and the produced alkaline solution from the electrochemical cell regenerated the resins and increased the CO_2 capture capacity of the resins. As the performance and reliability of the process have been demonstrated, the following chapters focused on the optimization of the electrochemical system aiming to reduce the energy consumption. In Chapter 4, we achieved a reduced energy consumption by decreasing the CO_2 desorption pressure and adding background electrolyte (i.e., phosphate or sulphate). In Chapter 5, we used theoretical simulation to investigate the performance of the electrochemical system and indicated the optimal operating conditions and process layout.

In this chapter, we will compare the developed technology with other carbon capture processes and discuss the application potential of the technology. Moreover, we identify the limitations of the technology and propose future research directions. Finally, we give some concluding remarks to put the developed technology into a broader context of closing global carbon cycle.

6.1. Comparison of carbon capture technologies

6.1.1. Direct air capture versus trees

One of the biggest doubts from general public on development of DAC technologies is the necessity of the investment while simple and straightforward solutions (e.g., planting more trees) are already available. Indeed, afforestation and reforestation are very important mitigation options for climate change. They can also bring additional benefits including enhanced biodiversity and improved soil carbon and nutrient cycles. However, there are risks associated with afforestation and reforestation, such as lower groundwater levels and competition with food production for land use.[36,37] In contrast, DAC technologies have the advantages of high capture efficiency and long-term storage reliability.

According to European Environment Agency (EEA), a mature tree can capture 22 $kgCO_2$ per annum.[184] Comparing with the commercial DAC plant Orca that has a carbon capture capacity of 4 $ktCO_2$ per annum,[185] to achieve the same amount of carbon removal from atmosphere, approximately 182000 trees need to be planted. So many mature trees would occupy more than 1 km^2 (10^6 m^2) of land. In comparison, the land use of the Orca plant is only about 1700 m^2. Hence, the DAC technology is more than 500 times more

efficient than planting trees. Moreover, the electrochemical process developed in this thesis can further reduce the land use of the DAC process, as the land use of heat exchange modules can be saved due to the room temperature operation. Furthermore, if the electrochemical process is considered to be fully powered by solar energy, the land occupation of the solar panels is estimated to be less than 5% of the trees. To achieve the climate goals of 1.5°C, DAC is expected to remove CO_2 from the atmosphere in the scale of several $GtCO_2$ per annum, which would translate to millions km^2 of land full of trees. Therefore, it is not realistic to only rely on the CO_2 removal capacities of trees to mitigate climate change, and DAC works as an efficient complementary approach to reach climate goals. Finally, trees can only store CO_2 over their lifetime (on average 100 years), so the permanent underground storage of CO_2 through DAC is a more reliable long-term CO_2 reduction solution.

6.1.2. pH-swing-based technologies

As the source of CO_2 capture and the applied current density vary significantly in each study, it is hard to directly compare the performance of the electrochemical system developed in this thesis with other existing technologies. The energy consumptions of this work and other existing electrochemical carbon capture technologies are listed in **Table 6.1**. In this discussion, we narrow down our focus on the pH-swing-based electrochemical carbon capture technologies, including technologies using bipolar membrane electrodialysis (BPMED) and proton-coupled electron transfer (PCET) molecules. We will discuss the effects of the source of CO_2 capture and current density on the electrochemical systems and compare the performance of the systems in terms of energy consumption and reliability.

Table 6.1. Overview of the energy consumptions of this work and other existing electrochemical carbon capture technologies.

Capture method	CO_2 source	Minimum energy consumption (kJ mol^{-1} CO_2)	Current density (A m^{-2})
MCDI[55]	Synthetic flue gas (15% CO_2)	40	0.2
BPMED[49]	$KHCO_3$	100	50
	K_2CO_3	200	50
BPMED[51]	Synthetic flue gas (16% CO_2)	52	180
EMAR[57]	Synthetic flue gas (15% CO_2)	30	40
pH swing with PCET molecules[53]	Synthetic flue gas (15% CO_2)	61	200
This work	Air (400 ppm CO_2)	247	150

Source of CO_2 capture

The CO_2 partial pressure in the source of the carbon capture determines the molar ratio of CO_3^{2-}/HCO_3^- in the feed solution of the electrochemical cell. When an alkaline absorbent is used for CO_2 capture from a flue gas containing 15% CO_2, the carbon species in the spent solution is mostly HCO_3^- based on CO_2 equilibria. For DAC with 400 ppm of CO_2 in the air, the spent alkaline solution would have a CO_3^{2-}/HCO_3^- molar ratio of about 3:2 at equilibrium. It requires two-proton transfer (equivalent to two-electron transfer) to convert one CO_3^{2-} to H_2CO_3 and further desorb as CO_2 gas, while the desorption of CO_2 from HCO_3^- only requires one-proton transfer. Therefore, the theoretical minimum energy consumption for a pH-swing-based technology is around 27% lower for capturing from flue gas than for DAC.

The other gases in the capture source also have effects on the performance of the system. Based on our study, some of the impurities in flue gas might be beneficial for the operation of inorganic pH-swing processes (e.g., HRES and BPMED) instead of just causing negative effects. For instance, the dissolution of impurities, such as SO_x and NO_x, could add background anions in the (spent) absorbent. As demonstrated in Chapter 4 and 5, the addition of background electrolytes reduced the energy consumption of the electrochemical system, which provided a positive side of the impurities from flue gas. However, as also discussed in previous chapters, a high concentration of background electrolytes reduced the capture capacity of the absorbent, which made the capture process less favorable. Moreover, it is not clear if the dissolved impurities would appear in the desorbed gas stream CO_2. Hence, further studies with such impurities are required to investigate the impact on the carbon capture processes. Moreover, the reduced form of the PCET molecules is significantly reactive with oxygen from the air, which restricts the application of the pH swing process with PCET

molecules in DAC. Finally, to the best of our knowledge, this work is the first study on DAC electrochemical system tested with real ambient air, which makes it one step further towards the practical application of the technology in large-scale.

Current density

A high current density is desired for the large-scale application of an electrochemical carbon capture system to reduce the capital expenditure (CAPEX) and the footprint of the system. However, a higher current density generally leads to a higher energy consumption in an electrochemical system, mainly due to the electrical resistance in the cell (e.g., resistance of the bulk solutions, boundary layers, and gas bubbles) and the non-ideal behaviors of the membranes and electrodes. All the above-mentioned technologies have a high energy consumption under high current densities, which limits their applications.

Specifically for electrochemical carbon capture technologies, one of the challenges for achieving lower energy consumption is to minimize the CO_2 gas formation inside the cell. When the spent absorbent is acidified inside the cell, CO_2 gas is formed that adds additional electrical resistance and reduces effective areas of membranes and electrodes. Different methods have been proposed for reducing the gas formation inside the cell, including high-pressure operation of BPMED [61] and external desorption layouts we proposed in Chapter 5. Nevertheless, one operating parameter, the flow velocity inside the electrochemical cell compartments, is often overlooked. In Chapter 5, we demonstrated that it is essential to circulate the solution in each compartment to increase the flow velocity and reduce the negative effects from gas bubbles. When the circulation of solution is fast enough, the effects of the gas bubbles can be eliminated. On the other hand, a higher flow velocity leads to a higher pressure drop over the cell, which results in an increase of pumping energy. Therefore, it is crucial for future techno-economic studies on electrochemical carbon capture technologies to take the circulation of solutions into account to determine the optimal operating conditions for the system.

Reliability

One of the advantages of the HRES comparing to BPMED is that there is no net production of O_2 and H_2. The H_2 production at the cathode of the HRES is consumed at the anode. In BPMED, the electrode reactions produce O_2 at the anode and H_2 at the cathode. Although both gases are valuable products, the handling of the flammable and explosive gases would introduce extra risks to the DAC plant. Moreover, the HRES establishes the pH swing based on an inorganic solution, which is safer and stabler than the organic solution like PCET molecules that might degrade and produce carcinogenic compounds. Finally, the HRES uses industry-proved components that guarantee its stability in long-term operation. The membrane electrode assembly (MEA) and ion exchange membranes used in the cell are widely used in proton-exchange membrane fuel cells and electrolyzers, which has been operated stable at high current density (> 5 kA m^{-2}) and high temperature (around 80°C).[66,68]

6.1.3. Ion-exchange-resin-based technologies

While amine-functionalized ion exchange resins (AERs) are eligible adsorbents for DAC, the electrochemical regeneration of the AERs showed several advantages over the thermal swing and moisture swing processes, including the resin stability and CO_2 capture capacity.

In a thermal swing process with AERs, CO_2 is captured by the resins under room temperature, and the regeneration of the resins is performed by heating up the resins to around 105°C.[111,112] In practice, air needs to be evacuated before heating up the resins, as the oxidative degradation of the functional groups on the resins occurs at temperatures higher than 60°C.[115] Even without O_2, Parvazinia et al. reported 5% degradation of the resins after 275 adsorption-desorption cycles.[112] On the other hand, the chemical regeneration of the resins using the alkaline solution produced by the electrochemical cell, due to the room temperature operation, showed great stability with no apparent degradation of the resins over 150 adsorption-desorption cycles.

In a moisture swing process, CO_2 can be adsorbed by dry resins and desorbed when the resins are wet. The CO_2 capture capacity of the resins was reported to be 0.86 mmol g^{-1} dry resins for DAC, and this capacity decreases with increasing humidity of the air.[116,186] In comparison, when the resins are regenerated with an electrochemical system, the highest CO_2 capture capacity achieved in the experiments was 1.76 mmol g^{-1} dry resins for DAC, with part of the capacity provided by the residual alkaline solution on the resin surface after the regeneration step. The electrochemically regenerated resins also showed a relatively high capacity with a humid air, as the capacity decreased only 22% with the relative humidity of the air source increased from 33 to 84%.

6.2. Challenges and perspectives on future research

6.2.1. CO_2 leakage

In Chapter 2 and 4, the experimental results and the simulated results showed a discrepancy in CO_2 production rate, which was likely due to the leakage of CO_2 from the system. The leakage of CO_2 could occur externally or internally of the cell. Externally, the desorbed CO_2 gas could leak from the membrane contactor, tubing, or connectors when the setup was not entirely gas tight. Internally, when the removal of CO_2 gas by the membrane contactor was incomplete, CO_2 could be carried by the overflow solution from the acidifying compartment to the cathode compartment. Moreover, the neutral carbon species ($H_2CO_3^*$) can permeate through the ion exchange membranes driven by a concentration gradient. Hence, the $H_2CO_3^*$ in the acidifying compartment can diffuse through the MEA or the CEM and leak to the anode or cathode compartment, respectively.

The external leakage of CO_2 would be mainly affected by the residence time of the solution in the electrochemical system, as the chance for the external leakage is bigger with

a longer residence time. Furthermore, the internal leakage would be affected by the removal efficiency of the membrane contactor and the production rate of CO_2. The removal efficiency of the membrane contactor was determined by the driving force of CO_2 desorption from liquid phase to gas phase (i.e., CO_2 partial pressure difference between the liquid and gas side of the membrane contactor). A higher production rate of CO_2 led to the increase of CO_2 concentration (partial pressure) in the acidifying solution, which facilitates the desorption of CO_2 in the membrane contactor but also the leakage of CO_2 through the membranes to other compartments. We took the experiments with decreased CO_2 desorption pressure in Chapter 4 as an example to plot the CO_2 leakage ratio ((simulated CO_2 production rate – experimental CO_2 production rate) / simulated CO_2 production rate) of these experiments in **Figure 6.1**. The results of Condition 1 and 2 showed a higher CO_2 leakage ratio with higher CO_2 desorption pressure, probably due to the insufficient removal efficiency at the membrane contactor. The slight difference in residence time of these two conditions due to different L_{K^+} did not show a clear impact on the leakage of CO_2. The residence time of the solution in Condition 3 was 25% shorter than in Condition 1 because of the increase of current density, which resulted in lower CO_2 leakage ratios in Condition 3. In Condition 3, due to the high CO_2 production rate and short residence time, the impact of the CO_2 desorption pressure became less significant.

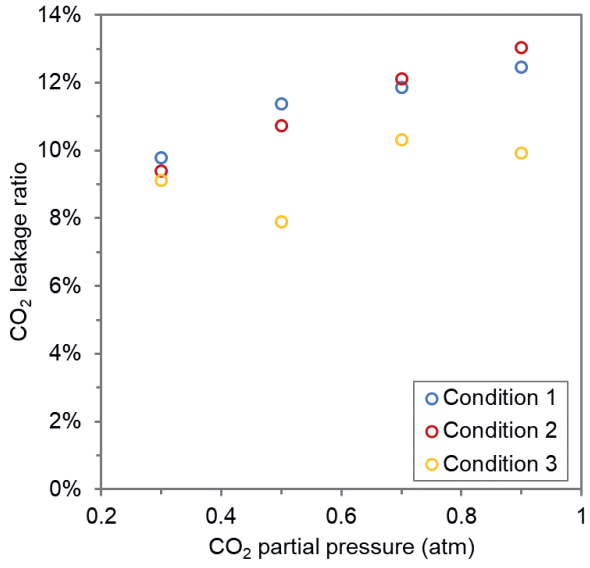

Figure 6.1. CO_2 leakage ratio of the decrease CO_2 desorption pressure experiments in Chapter 4. Condition 1: j_c = 150 A m^{-2}, L_{K^+} = 0.8, 0.1 M phosphate buffer; condition 2: j_c = 150 A m^{-2}, L_{K^+} = 0.9, 0.1 M phosphate buffer; condition 3: j_c = 200 A m^{-2}, L_{K^+} = 0.8, 0.1M phosphate buffer. j_c is the applied current density, L_{K^+} is the load ratio of K^+.

Finally, for large-scale application of the HRES, the external leakage should be avoided by a gas-tight design. The internal leakage can be minimized by improving the CO_2 removal

efficiency of the degassing unit and developing more selective ion exchange membranes to prevent the transport of non-charged CO_2 species from transporting through the membrane.

6.2.2. Modelling of the electrochemical system

In Chapter 2 to 5, we developed and improved a mathematical model to simulate the performance of the HRES. Although the model was validated by the experimental results on predicting the equilibrium conditions in the system (i.e., pH, conductivity, and solution compositions), it is still challenging to predict the energy consumption of the system. Other than the CO_2 leakage issue as stated in the previous section, the current model does not include the boundary conditions on the surface of the electrodes and membranes, which leads to an underestimation of the cell voltage and energy consumption.

A membrane electrode assembly (MEA) containing a gas diffusion electrode (GDE) and a cation exchange membrane (CEM) was used at the anode side of the electrochemical cell (**Figure 6.2**). Although the GDE had a layer of hydrophobic coating, the flooding of the electrode would still happen due to the non-ideal performance of the coating.[181] The flooding of the GDE limited the transport of H_2 to the catalytic layer of the electrode where it can be oxidized. As a result, due to the limited access of H_2 at the electrode surface, the concentration overpotential at the anode increased. Moreover, on the other side of the MEA, the H^+ and HCO_3^- were both transported towards the surface of the CEM under the electrical field. The low local pH led to the formation of H_2CO_3 and evolution of CO_2 gas. The formation of electroneutral species decreased the conductivity on the surface of the CEM, which caused a large potential loss. In Chapter 4, we demonstrated the benefits of adding background electrolytes to the acidifying solution that provided extra conductivity at the membrane surface. However, due to the extremely low local pH at the surface of the CEM, the evolution of CO_2 gas was not avoidable, which increased the potential drop in the cell by adding extra resistance and reducing effective membrane area.

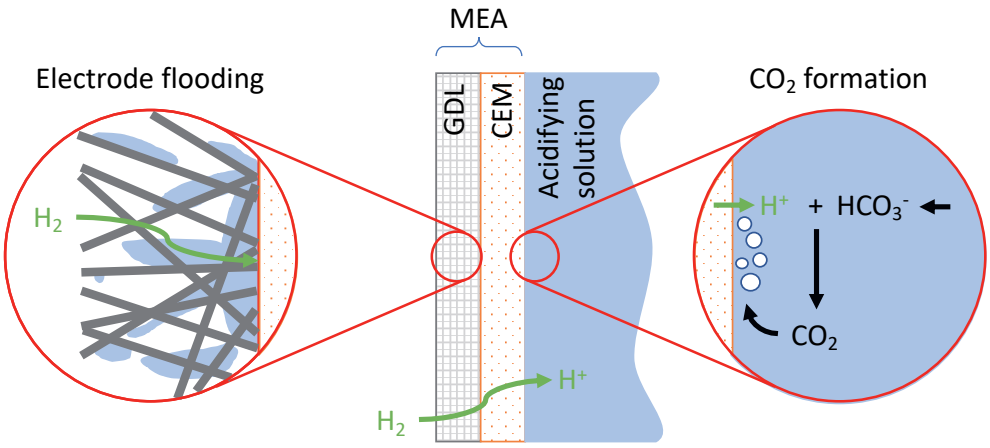

Figure 6.2. Boundary effects on the surfaces of the gas diffusion electrode (GDE) and the cation exchange membrane (CEM). MEA: membrane electrode assembly.

Electrode flooding has been studied extensively in fuel cell and CO_2 reduction applications, and improvements have been proposed regarding the modification of the material and structural properties of the MEA.[187,188] Further studies are required to investigate the application of these improvement methods in an HRES cell. Furthermore, the CO_2 formation phenomenon at the membrane surface needs more quantification methods (e.g., measuring local pH to quantify the amount of CO_2 gas formed) to better understand the behavior and include in the model.

6.2.3. Effects of background electrolytes

In Chapter 3, we have combined the electrochemical system with an adsorption step using amine-functionalized AERs, where the AERs were used as the CO_2 sorbent and the alkaline solution produced by the electrochemical cell was used to regenerate the CO_2-saturated AERs. We showed the stability of the resins in 150 adsorption-desorption cycles with no measurable degradation. Moreover, in Chapter 4 and 5, we have demonstrated both experimentally and theoretically the positive impact of sulphate (background electrolyte) addition in the absorbent on the energy performance of the electrochemical cell. However, the effects of the sulphate addition on the performance of the adsorption step remains unclear. Therefore, we experimentally studied the difference in carbon capture capacity of AERs using alkaline solution with or without addition of sulphate as background electrolyte. We have first performed 17 adsorption-desorption cycles while the resins were regenerated with 1 M KOH solution. The average amount of CO_2 adsorption in these 17 cycles, 0.72 mmol CO_2 g^{-1} dry resins, was considered as the maximum adsorption amount under the operating condition. Then another 34 adsorption-desorption cycles were performed with the resins regenerated by 0.8 M KOH mixed with 0.1 M K_2SO_4. The proportional change of the CO_2 adsorption amount has been

plotted in **Figure 6.3**, and it showed a 30% decrease with 0.1 M SO_4^{2-} addition in the regeneration solution.

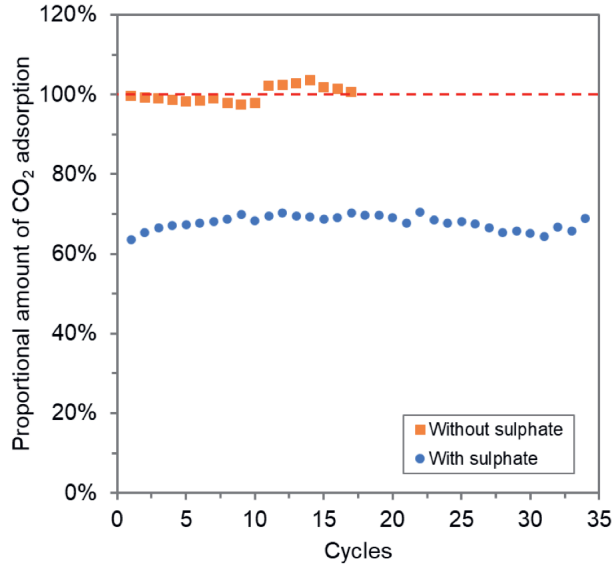

Figure 6.3. Proportional change of CO_2 adsorption amount in repeated adsorption-desorption cycles. The adsorption steps were performed with ambient air, while the resins were regenerated with either 1 M KOH or 0.8 M KOH mixed with 0.1 M K_2SO_4. The average amount of CO_2 adsorption in the 17 cycles with pure KOH regeneration was counted as 100%, then the proportional CO_2 adsorption amount of each cycle was calculated accordingly.

The amount of CO_2 that can be captured by the resins is primarily determined by the available sites of OH^- on the surface of the resins. With a complete regeneration using pure KOH, all the resins can be regenerated to OH^- form that have the maximum capacity for CO_2 capture. The addition of SO_4^{2-} in the regeneration solution has changed the equilibrium during regeneration. The quaternary amine groups on the surface of the resins have higher affinity towards divalent ions.[189] As a result, using the mixture of 0.8 M KOH and 0.1 M K_2SO_4 as the regeneration solution, the SO_4^{2-} ions occupied more than 20% of the quaternary amine groups after regeneration, while less than 80% of the functional groups can be regenerated to OH^- form. Moreover, the selectivity of SO_4^{2-} was also higher than CO_3^{2-}, so the exchange of SO_4^{2-} ions with CO_3^{2-} ions during the adsorption step was not favored. Furthermore, with a fixed composition of the regeneration solution, the ions in the solution and the ions on the resins reached the same equilibrium state in every cycle. Therefore, we observed the stable adsorption behavior in 34 cycles showing that the SO_4^{2-} ions did not accumulate in the resins. Finally, due to the reduced CO_2 adsorption amount when regenerated with SO_4^{2-} added solution, the process required more operational cycles or larger quantity of resins to achieve the same desired amount of CO_2 capture. This extra cost in the adsorption step needs to be

assessed together with the benefit on energy consumption of the electrochemical cell to determine the optimal concentration of SO_4^{2-} addition.

6.3. Towards a sustainable carbon cycle

The carbon cycle describes the flow of carbon atoms among various carbon reservoirs on Earth, including the atmosphere, land, oceans, and living organisms. The balance of the global carbon cycle plays a crucial role in regulating the Earth climate, making Earth a livable planet for human beings. However, human activities, such as the burning of fossil fuels and deforestation, have significantly perturbed the carbon cycle.[190] These activities have rapidly released the carbon from fossil fuels and biomass into the atmosphere, resulting in a sharp increase of the atmospheric CO_2 concentration. The increase of CO_2 concentration in the atmosphere has led to a warming planet and other climate changes. To mitigate the risks of the climate change, the Intergovernmental Panel on Climate Change (IPCC) has set the goal of reaching net-zero emissions, which is also the way to move towards a sustainable carbon cycle.

The work of this thesis will contribute to the sustainable carbon cycle in two aspects: reducing atmospheric CO_2 concentration and providing a net-negative source of carbon. The developed electrochemical DAC technology can capture CO_2 from the atmosphere, and it is crucial for counterbalancing hard-to-eliminate emissions. The electrochemical process can be fully powered by renewable energy, which leads to a carbon-net-negative production of high-purity CO_2 gas. While the captured CO_2 can be permanently stored underground to reach the climate goals, it also provides a sustainable source of carbon for CO_2 conversion to fuels[191,192], chemicals[193,194], and production of microalgae[195,196]. Therefore, with support of renewable energy, electrochemical DAC and the utilization of the captured CO_2 will create a closed sustainable carbon cycle.

Closing the carbon cycle will require a coordinated effort from individuals, businesses, and governments. By taking actions to reduce our carbon emissions and increase carbon removal, we can help to mitigate the impacts of climate change and create a more sustainable future.

Summary

Human activities, such as the burning of fossil fuels and deforestation, have increased the concentration of greenhouse gases (GHGs) in the atmosphere, contributing to global climate change. The resulting increase in the global average surface temperature by approximately 1.1°C since the late 19th century is damaging the living conditions on Earth, including triggering more frequent wildfires and causing longer periods of drought. The Paris Agreement, an international treaty on climate change, aims to limit global warming in this century to well below 2°C and preferably to 1.5°C. However, the current climate actions are inadequate to achieve the targets without immediate and deep emissions reductions across all sectors. It is crucial to implement sustainable strategies to reduce the atmospheric concentration of GHGs and mitigate the impacts of climate change. Strategies, including the deployment of electrification and development of renewable energy, will reduce the emissions of GHGs and provide a wide access to renewable electricity. Moreover, technologies that can remove atmospheric CO_2, the main climate change driver, are essential to achieve the net-zero emission goals. Therefore, in this thesis, I designed and developed an electrochemical direct air capture (DAC) system, aiming to reduce the atmospheric CO_2 concentration and produce high-purity CO_2 gas for further sequestration.

Conventional technologies based on alkaline absorbents have been demonstrated on a full scale for DAC. However, the regeneration of the spent alkaline absorbents requires a high temperature and is highly energy-demanding. In **Chapter 2**, a H_2-recycling electrochemical system (HRES) was experimentally demonstrated for simultaneous absorbent regeneration and CO_2 desorption. With H_2 oxidation and evolution reactions, a pH gradient was established in two adjacent compartments of the electrochemical cell. CO_2 was desorbed from the spent absorbent at a low pH, while the alkaline absorbent was regenerated at a high pH. The lowest experimental energy consumption was achieved at 374 kJ mol^{-1} CO_2 with a current density of 50 A m^{-2}, and the desorbed CO_2 gas had a purity higher than 95%. Moreover, up to 59% of the CO_2 capture capacity of the absorbent could be regenerated under the operating conditions investigated in this chapter. Finally, a mathematical model was developed to describe the performance of the system, and the simulation results showed a minimum energy consumption of 164 kJ mol^{-1} might be achieved.

In **Chapter 3**, the HRES was integrated with a CO_2 adsorption in a packed bed of amine-functionalized anion exchange resins (AERs). Due to the reaction between CO_2 and the quaternary amine groups on the resins, the AERs can capture CO_2 directly from the atmosphere. In the integrated system, the resin bed was regenerated by the alkaline solution produced in the cathode compartment of the HRES, while the spent regeneration solution was acidified in the acidifying compartment to desorb high-purity CO_2 gas (>95%). A small amount of the alkaline solution remained on the surface of the AERs after the regeneration step, which was found to be providing additional CO_2 capture capacity to the resins. After the electrochemical regeneration, the CO_2 capture capacity measured was up to 1.76 mmol g^{-1} dry resins. Moreover, no apparent degradation of the resins was observed after 150

adsorption-desorption cycles. Furthermore, the impact of the relative humidity of the air source on the performance of the adsorption step was also investigated. With an increase of relative humidity from 33% to 84%, the water loss of the process decreased by 63% while CO_2 capture capacity decreased by 22%. The energy consumption of the HRES in this study was 537 ± 33 kJ mol^{-1} at 200 A m^{-2}, and the increase of the energy consumption comparing to the previous chapter was attributed to the internal resistance of the cell and the increasing electrode overpotentials at higher current densities.

As the performance and reliability of the process have been demonstrated, the following chapters focused on the optimization of the electrochemical system aiming to reduce the energy consumption. In **Chapter 4**, two optimization strategies were investigated both experimentally and theoretically, including decreasing the CO_2 desorption pressure and adding background electrolyte. A partial vacuum was applied to the degassing unit to increase the driving force for the desorption of CO_2 and facilitate the removal of CO_2 gas bubbles from the electrochemical cell. When the CO_2 partial pressure for the desorbed CO_2 was reduced from 0.9 to 0.3 atm, the energy consumption of the electrochemical cell decreased by at least 12%. Moreover, phosphate and sulphate were added in the alkaline absorbent as background electrolyte to provide additional conductivity in the cell. The reduced ohmic losses in the bulk solutions and the boundary layers of the membranes have reduced the energy consumption of the cell. However, the CO_2 production rate was limited by either the low total carbon feeding rate or the high acidifying solution pH at higher concentrations of phosphate. Hence, the optimal concentration for phosphate addition was 0.1 M. Furthermore, 0.1 M of sulphate addition provided a lower energy consumption than 0.1 M of phosphate addition, as sulphate had a higher molar conductivity than phosphate, and the lower pKa of sulphate helped maintain the high conductivity also on the surface of the membrane. Overall, the lowest energy consumption was achieved experimentally at 247 kJ mol^{-1} CO_2 with CO_2 partial pressure of 0.3 atm and 0.1 M of sulphate addition under current density of 150 A m^{-2}. The model simulation results on the equilibrium conditions of the system matched with the observations in the experiments, but the energy consumption of the system was underestimated by the model.

One of the reasons for the underestimation of the model prediction was that the bubble resistance was not included in the previously developed model. Thus, in **Chapter 5**, the model was improved by including bubble resistance parameter and used to investigate the effects of various process layouts and operating conditions on the performance of electrochemical regeneration process. According to the simulation results, the circulation of solution in each compartment is crucial to reduce the gas bubble resistance. The energy consumption decreased by 20% with the recirculation ratio increased from 5 to 10. Nevertheless, as the gas bubble resistance was reduced with increasing recirculation ratio, the benefits from faster circulation became less significant. Therefore, the optimal recirculation ratio required to balance the tradeoff between the reduction of bubble resistance and the investment in pumping energy. Moreover, in the previous chapter, phosphate addition of more than 0.1 M did not

benefit the energy consumption of the system. However, the model developed in this chapter showed that the increasing concentration of SO_4^{2-} as background electrolyte decreased the energy consumption due to the lower pKa of sulphate than phosphate. Furthermore, a lower current density was also demonstrated to be favorable for reducing the energy consumption, although the CO_2 production rate was limited at a low current density which would increase the capital expenditure (CAPEX) and the footprint of the system. Finally, three process layouts, including one internal desorption layout and two external desorption layouts, were simulated to investigate the effects on CO_2 gas bubble formation. The 2-unit external desorption layout, having a high CO_2 desorption efficiency and a low amount of gas bubbles in the cell, was shown to be the most energy efficient option. Among all the investigated conditions in this chapter, the lowest energy consumption achieved was 128 kJ mol^{-1} CO_2, which made this technology a promising candidate for DAC absorbent electrochemical regeneration.

Chapter 6 compared the DAC process developed in this thesis with existing technologies and concepts. The DAC process showed clear advantage to planting trees in terms of less land use and more secured long-term storage. While comparing with other pH-swing-based electrochemical technologies, the effects of the source of CO_2 capture and the current density on the performance of the system have been discussed. Moreover, the challenges during the development of the technology, including CO_2 leakage issues, modeling of the electrochemical system, and the limitations of the absorption/adsorption step, have been addressed, and possible research directions regarding these challenges have been proposed. Lastly, the vision towards a sustainable carbon cycle is shared.

Bibliography

(1) *Elfstedentocht*. https://www.elfstedentocht.frl/ (accessed 2023-02-17).

(2) Osman, M. B.; Tierney, J. E.; Zhu, J.; Tardif, R.; Hakim, G. J.; King, J.; Poulsen, C. J. Globally Resolved Surface Temperatures since the Last Glacial Maximum. *Nature* **2021**, *599* (7884), 239–244. https://doi.org/10.1038/s41586-021-03984-4.

(3) Lynas, M.; Houlton, B. Z.; Perry, S. Greater than 99% Consensus on Human Caused Climate Change in the Peer-Reviewed Scientific Literature. *Environmental Research Letters* **2021**, *16* (11), 114005. https://doi.org/10.1088/1748-9326/ac2966.

(4) Caldeira, K.; Jain, A. K.; Hoffert, M. I. Climate Sensitivity Uncertainty and the Need for Energy Without CO2 Emission. *Science (1979)* **2003**, *299* (5615), 2052–2054. https://doi.org/10.1126/science.1078938.

(5) Lawrence, D.; Vandecar, K. Effects of Tropical Deforestation on Climate and Agriculture. *Nat Clim Chang* **2015**, *5* (1), 27–36. https://doi.org/10.1038/nclimate2430.

(6) *Carbon Dioxide | Vital Signs – Climate Change: Vital Signs of the Planet*. https://climate.nasa.gov/vital-signs/carbon-dioxide/ (accessed 2023-02-17).

(7) *Global Temperature | Vital Signs – Climate Change: Vital Signs of the Planet*. https://climate.nasa.gov/vital-signs/global-temperature/ (accessed 2023-02-17).

(8) Stoll, H. M.; Cacho, I.; Gasson, E.; Sliwinski, J.; Kost, O.; Moreno, A.; Iglesias, M.; Torner, J.; Perez-Mejias, C.; Haghipour, N.; Cheng, H.; Edwards, R. L. Rapid Northern Hemisphere Ice Sheet Melting during the Penultimate Deglaciation. *Nat Commun* **2022**, *13* (1), 3819. https://doi.org/10.1038/s41467-022-31619-3.

(9) Hong, C.; Zhang, Q.; Zhang, Y.; Davis, S. J.; Tong, D.; Zheng, Y.; Liu, Z.; Guan, D.; He, K.; Schellnhuber, H. J. Impacts of Climate Change on Future Air Quality and Human Health in China. *Proceedings of the National Academy of Sciences* **2019**, *116* (35), 17193–17200. https://doi.org/10.1073/pnas.1812881116.

(10) Mora, C.; Dousset, B.; Caldwell, I. R.; Powell, F. E.; Geronimo, R. C.; Bielecki, C. R.; Counsell, C. W. W.; Dietrich, B. S.; Johnston, E. T.; Louis, L. v; Lucas, M. P.; McKenzie, M. M.; Shea, A. G.; Tseng, H.; Giambelluca, T. W.; Leon, L. R.; Hawkins, E.; Trauernicht, C. Global Risk of Deadly Heat. *Nat Clim Chang* **2017**, *7* (7), 501–506. https://doi.org/10.1038/nclimate3322.

(11) Bender, M. A.; Knutson, T. R.; Tuleya, R. E.; Sirutis, J. J.; Vecchi, G. A.; Garner, S. T.; Held, I. M. Modeled Impact of Anthropogenic Warming on the Frequency of Intense Atlantic Hurricanes. *Science (1979)* **2010**, *327* (5964), 454–458. https://doi.org/10.1126/science.1180568.

(12) IPCC. *Global Warming of 1.5° C: An IPCC Special Report on the Impacts of Global Warming of 1.5° C above Pre-Industrial Levels and Related Global Greenhouse Gas Emission Pathways, in the Context of Strengthening the Global Response to the Threat of Climate Change, Sustainable Development, and Efforts to Eradicate Poverty*; v. Masson-Delmotte H. O. Pörtner D. Roberts J. Skea P.R. Shukla A. Pirani W., P. Z., Moufouma-Okia R. Pidcock S. Connors J. B. R. Matthews Y. Chen X. Zhou M. I. Gomis E. Lonnoy, C. P., T. Maycock T. Waterfield, M. T., Eds.; In Press, 2018.

(13) IPCC. *Climate Change 2022: Mitigation of Climate Change. Contribution of Working Group III to the Sixth Assessment Report of the Intergovernmental Panel on Climate Change*; 2022. https://doi.org/10.1017/9781009157926.

(14) Eskander, S. M. S. U.; Fankhauser, S. Reduction in Greenhouse Gas Emissions from National Climate Legislation. *Nat Clim Chang* **2020**, *10* (8), 750–756. https://doi.org/10.1038/s41558-020-0831-z.

(15) IPCC. Summary for Policymakers. In *Climate Change 2021: The Physical Science Basis. Contribution of Working Group I to the Sixth Assessment Report of the Intergovernmental Panel on Climate Change*; Masson-Delmotte, V., Zhai, P., Pirani, A., Connors, S. L., Péan, C., Berger, S., Caud, N., Chen, Y., Goldfarb, L., Gomis, M. I., Huang, M., Leitzell, K., Lonnoy, E., Matthews, J. B. R., Maycock, T. K., Waterfield, T., Yelekçi, O., Yu, R., Zhou, B., Eds.; Cambridge University Press: Cambridge, United Kingdom and New York, NY, USA, 2021; p 3−32. https://doi.org/10.1017/9781009157896.001.

(16) *Electrification – Analysis - IEA*. https://www.iea.org/reports/electrification (accessed 2023-02-17).

(17) Olabi, A. G.; Abdelkareem, M. A. Renewable Energy and Climate Change. *Renewable and Sustainable Energy Reviews* **2022**, *158*, 112111. https://doi.org/10.1016/J.RSER.2022.112111.

(18) Elavarasan, R. M.; Shafiullah, G.; Padmanaban, S.; Kumar, N. M.; Annam, A.; Vetrichelvan, A. M.; Mihet-Popa, L.; Holm-Nielsen, J. B. A Comprehensive Review on Renewable Energy Development, Challenges, and Policies of Leading Indian States with an International Perspective. *IEEE Access* **2020**, *8*, 74432–74457. https://doi.org/10.1109/ACCESS.2020.2988011.

(19) Qazi, A.; Hussain, F.; Rahim, N. A. B. D.; Hardaker, G.; Alghazzawi, D.; Shaban, K.; Haruna, K. Towards Sustainable Energy: A Systematic Review of Renewable Energy Sources, Technologies, and Public Opinions. *IEEE Access* **2019**, *7*, 63837–63851. https://doi.org/10.1109/ACCESS.2019.2906402.

(20) International Renewable Energy Agency. RENEWABLE ENERGY STATISTICS 2022. **2022**, 2.

(21) Bogdanov, D.; Ram, M.; Aghahosseini, A.; Gulagi, A.; Oyewo, A. S.; Child, M.; Caldera, U.; Sadovskaia, K.; Farfan, J.; de Souza Noel Simas Barbosa, L.; Fasihi, M.; Khalili, S.; Traber, T.; Breyer, C. Low-Cost Renewable Electricity as the Key Driver of the Global Energy Transition towards Sustainability. *Energy* **2021**, *227*, 120467. https://doi.org/10.1016/J.ENERGY.2021.120467.

(22) Ram, M.; Child, M.; Aghahosseini, A.; Bogdanov, D.; Lohrmann, A.; Breyer, C. A Comparative Analysis of Electricity Generation Costs from Renewable, Fossil Fuel and Nuclear Sources in G20 Countries for the Period 2015-2030. *J Clean Prod* **2018**, *199*, 687–704. https://doi.org/10.1016/J.JCLEPRO.2018.07.159.

(23) Luderer, G.; Madeddu, S.; Merfort, L.; Ueckerdt, F.; Pehl, M.; Pietzcker, R.; Rottoli, M.; Schreyer, F.; Bauer, N.; Baumstark, L.; Bertram, C.; Dirnaichner, A.; Humpenöder, F.; Levesque, A.; Popp, A.; Rodrigues, R.; Strefler, J.; Kriegler, E. Impact of Declining Renewable Energy Costs on Electrification in Low-Emission Scenarios. *Nat Energy* **2022**, *7* (1), 32–42. https://doi.org/10.1038/s41560-021-00937-z.

(24) *The Future of Hydrogen – Analysis - IEA*. https://www.iea.org/reports/the-future-of-hydrogen (accessed 2023-02-17).

(25) Gielen, D.; Saygin, D.; Taibi, E.; Birat, J. P. Renewables-Based Decarbonization and Relocation of Iron and Steel Making: A Case Study. *J Ind Ecol* **2020**, *24* (5), 1113–1125. https://doi.org/10.1111/JIEC.12997.

(26) *Hydrogen*. https://www.irena.org/Energy-Transition/Technology/Hydrogen (accessed 2023-02-17).

(27) Tollefson, J. Carbon Emissions Hit New High: Warning from COP27. *Nature*.

(28) Boot-Handford, M. E.; Abanades, J. C.; Anthony, E. J.; Blunt, M. J.; Brandani, S.; mac Dowell, N.; Fernandez, J. R.; Ferrari, M.-C.; Gross, R.; Hallett, J. P.; Haszeldine, R. S.; Heptonstall, P.; Lyngfelt, A.; Makuch, Z.; Mangano, E.; Porter, R. T. J.; Pourkashanian, M.; Rochelle, G. T.; Shah, N.; Yao, J. G.; Fennell, P. S. Carbon Capture and Storage Update. *Energy Environ Sci* **2014**, *7* (1), 130–189. https://doi.org/10.1039/c3ee42350f.

(29) Bui, M.; Adjiman, C. S.; Bardow, A.; Anthony, E. J.; Boston, A.; Brown, S.; Fennell, P. S.; Fuss, S.; Galindo, A.; Hackett, L. A.; Hallett, J. P.; Herzog, H. J.; Jackson, G.; Kemper, J.; Krevor, S.; Maitland, G. C.; Matuszewski, M.; Metcalfe, I. S.; Petit, C.; Puxty, G.; Reimer, J.; Reiner, D. M.; Rubin, E. S.; Scott, S. A.; Shah, N.; Smit, B.; Trusler, J. P. M.; Webley, P.; Wilcox, J.; mac Dowell, N. Carbon Capture and Storage (CCS): The Way Forward. *Energy Environ Sci* **2018**, *11* (5), 1062–1176. https://doi.org/10.1039/c7ee02342a.

(30) Townsend, A.; Raji, N.; Zapantis, A. The Value of Carbon Capture and Storage (CCS). *Global CCS Institute: Docklands, Australia* **2020**.

(31) *3. Global Status of CCS – Global Carbon*. https://status22.globalccsinstitute.com/2022-status-report/global-status-of-ccs/ (accessed 2023-02-17).

(32) Board, O. S.; Council, N. R. *Climate Intervention: Carbon Dioxide Removal and Reliable Sequestration*; National Academies Press, 2015.

(33) Rosa, L.; Sanchez, D. L.; Mazzotti, M. Assessment of Carbon Dioxide Removal Potential via BECCS in a Carbon-Neutral Europe. *Energy Environ Sci* **2021**, *14* (5), 3086–3097. https://doi.org/10.1039/D1EE00642H.

(34) Fuss, S.; Canadell, J. G.; Peters, G. P.; Tavoni, M.; Andrew, R. M.; Ciais, P.; Jackson, R. B.; Jones, C. D.; Kraxner, F.; Nakicenovic, N.; le Quéré, C.; Raupach, M. R.; Sharifi, A.; Smith, P.; Yamagata, Y. Betting on Negative Emissions. *Nature Climate Change 2014 4:10* **2014**, *4* (10), 850–853. https://doi.org/10.1038/nclimate2392.

(35) Erans, M.; Sanz-Pérez, E. S.; Hanak, D. P.; Clulow, Z.; Reiner, D. M.; Mutch, G. A. Direct Air Capture: Process Technology, Techno-Economic and Socio-Political Challenges. *Energy Environ Sci* **2022**, *15* (4), 1360–1405. https://doi.org/10.1039/D1EE03523A.

(36) Trabucco, A.; Zomer, R. J.; Bossio, D. A.; van Straaten, O.; Verchot, L. v. Climate Change Mitigation through Afforestation/Reforestation: A Global Analysis of Hydrologic Impacts with Four Case Studies. *Agric Ecosyst Environ* **2008**, *126* (1–2), 81–97. https://doi.org/10.1016/J.AGEE.2008.01.015.

(37) Zomer, R. J.; Trabucco, A.; Bossio, D. A.; Verchot, L. v. Climate Change Mitigation: A Spatial Analysis of Global Land Suitability for Clean Development Mechanism Afforestation and Reforestation. *Agric Ecosyst Environ* **2008**, *126* (1–2), 67–80. https://doi.org/10.1016/J.AGEE.2008.01.014.

(38) Fajardy, M.; mac Dowell, N. Can BECCS Deliver Sustainable and Resource Efficient Negative Emissions? *Energy Environ Sci* **2017**, *10* (6), 1389–1426.

(39) *Bioenergy with Carbon Capture and Storage – Analysis - IEA*. https://www.iea.org/reports/bioenergy-with-carbon-capture-and-storage (accessed 2023-02-17).

(40) Fridahl, M.; Lehtveer, M. Bioenergy with Carbon Capture and Storage (BECCS): Global Potential, Investment Preferences, and Deployment Barriers. *Energy Res Soc Sci* **2018**, *42*, 155–165. https://doi.org/10.1016/J.ERSS.2018.03.019.

(41) Sanz-Perez, E. S.; Murdock, C. R.; Didas, S. A.; Jones, C. W. Direct Capture of CO2 from Ambient Air. *Chem Rev* **2016**, *116* (19), 11840–11876. https://doi.org/10.1021/acs.chemrev.6b00173.

(42) Beuttler, C.; Charles, L.; Wurzbacher, J. The Role of Direct Air Capture in Mitigation of Anthropogenic Greenhouse Gas Emissions. *Frontiers in Climate* **2019**, *1*, 10.

(43) Deutz, S.; Bardow, A. Life-Cycle Assessment of an Industrial Direct Air Capture Process Based on Temperature–Vacuum Swing Adsorption. *Nat Energy* **2021**, *6* (2), 203–213.

(44) Wurzbacher, J. A.; Gebald, C.; Brunner, S.; Steinfeld, A. Heat and Mass Transfer of Temperature–Vacuum Swing Desorption for CO2 Capture from Air. *Chemical Engineering Journal* **2016**, *283*, 1329–1338. https://doi.org/10.1016/J.CEJ.2015.08.035.

(45) Keith, D. W.; Holmes, G.; st. Angelo, D.; Heidel, K. A Process for Capturing CO2 from the Atmosphere. *Joule* **2018**, *2* (8), 1573–1594. https://doi.org/https://doi.org/10.1016/j.joule.2018.05.006.

(46) Sharifian, R.; Wagterveld, M.; Digdaya, I. A.; Xiang, C.; Vermaas, D. A. Electrochemical Carbon Dioxide Capture to Close the Carbon Cycle. *Energy Environ Sci* **2021**. https://doi.org/10.1039/d0ee03382k.

(47) Diederichsen, K. M.; Sharifian, R.; Kang, J. S.; Liu, Y.; Kim, S.; Gallant, B. M.; Vermaas, D.; Hatton, T. A. Electrochemical Methods for Carbon Dioxide Separations. *Nature Reviews Methods Primers 2022 2:1* **2022**, *2* (1), 1–20. https://doi.org/10.1038/s43586-022-00148-0.

(48) E. Renfrew, S.; E. Starr, D.; Strasser, P. Electrochemical Approaches toward CO2 Capture and Concentration. *ACS Catal* **2020**, *10* (21), 13058–13074. https://doi.org/10.1021/acscatal.0c03639.

(49) Eisaman, M. D.; Alvarado, L.; Larner, D.; Wang, P.; Garg, B.; Littau, K. A. CO 2 Separation Using Bipolar Membrane Electrodialysis. *Energy Environ Sci* **2011**, *4* (4), 1319–1328.

(50) Iizuka, A.; Hashimoto, K.; Nagasawa, H.; Kumagai, K.; Yanagisawa, Y.; Yamasaki, A. Carbon Dioxide Recovery from Carbonate Solutions Using Bipolar Membrane Electrodialysis. *Sep Purif Technol* **2012**, *101*, 49–59. https://doi.org/https://doi.org/10.1016/j.seppur.2012.09.016.

(51) Valluri, S.; Kawatra, S. K. Reduced Reagent Regeneration Energy for CO2 Capture with Bipolar Membrane Electrodialysis. *Fuel Processing Technology* **2021**, *213*, 106691. https://doi.org/10.1016/J.FUPROC.2020.106691.

(52) Jin, S.; Wu, M.; Gordon, R. G.; Aziz, M. J.; Kwabi, D. G. PH Swing Cycle for CO2 Capture Electrochemically Driven through Proton-Coupled Electron Transfer. *Energy Environ Sci* **2020**. https://doi.org/10.1039/D0EE01834A.

(53) Jin, S.; Wu, M.; Jing, Y.; Gordon, R. G.; Aziz, M. J. Low Energy Carbon Capture via Electrochemically Induced PH Swing with Electrochemical Rebalancing. *Nature Communications 2022 13:1* **2022**, *13* (1), 1–11. https://doi.org/10.1038/s41467-022-29791-7.

(54) Legrand, L.; Shu, Q.; Tedesco, M.; Dykstra, J. E.; Hamelers, H. V. M. Role of Ion Exchange Membranes and Capacitive Electrodes in Membrane Capacitive Deionization (MCDI) for CO2 Capture. *J Colloid Interface Sci* **2020**, *564*, 478–490. https://doi.org/https://doi.org/10.1016/j.jcis.2019.12.039.

(55) Legrand, L.; Schaetzle, O.; de Kler, R. C. F.; Hamelers, H. V. M. Solvent-Free CO2 Capture Using Membrane Capacitive Deionization. *Environ Sci Technol* **2018**, *52* (16), 9478–9485. https://doi.org/10.1021/acs.est.8b00980.

(56) Stern, M. C.; Hatton, T. A. Bench-Scale Demonstration of CO2 Capture with Electrochemically-Mediated Amine Regeneration. *RSC Adv* **2014**, *4* (12), 5906–5914. https://doi.org/10.1039/C3RA46774K.

(57) Wang, M.; J. Herzog, H.; Alan Hatton, T. CO2 Capture Using Electrochemically Mediated Amine Regeneration. *Industrial & Engineering Chemistry Research* **2020**, *59* (15), 7087–7096. https://doi.org/10.1021/acs.iecr.9b05307.

(58) Stern, M. C.; Simeon, F.; Herzog, H.; Hatton, T. A. Post-Combustion Carbon Dioxide Capture Using Electrochemically Mediated Amine Regeneration. *Energy Environ Sci* **2013**, *6* (8), 2505–2517. https://doi.org/10.1039/C3EE41165F.

(59) Sabatino, F.; Mehta, M.; Grimm, A.; Gazzani, M.; Gallucci, F.; Kramer, G. J.; van Sint Annaland, M. Evaluation of a Direct Air Capture Process Combining Wet Scrubbing and Bipolar Membrane Electrodialysis. *Ind Eng Chem Res* **2020**, *59* (15), 7007–7020. https://doi.org/10.1021/acs.iecr.9b05641.

(60) Stolaroff, J. K.; Keith, D. W.; Lowry, G. v. Carbon Dioxide Capture from Atmospheric Air Using Sodium Hydroxide Spray. *Environ Sci Technol* **2008**, *42* (8), 2728–2735. https://doi.org/10.1021/es702607w.

(61) Eisaman, M. D.; Alvarado, L.; Larner, D.; Wang, P.; Littau, K. A. CO2 Desorption Using High-Pressure Bipolar Membrane Electrodialysis. *Energy Environ Sci* **2011**, *4* (10), 4031–4037.

(62) Legrand, L. J. P.; Buisman, C. J. N. P. dr; Hamelers, H. V. M. D.; Tedesco, M. D.; Legrand, L. J. P.; Buisman, C. J. N. P. dr; Hamelers, H. V. M. D.; Tedesco, M. D. Capacitive Processes for Carbon Capture and Energy Recovery from CO2 Emissions : Shaping a New Technology Going from Water to Gas Applications, Wageningen, 2020.

(63) Rahimi, M.; Catalini, G.; Puccini, M.; Hatton, T. A. Bench-Scale Demonstration of CO2 Capture with an Electrochemically Driven Proton Concentration Process. *RSC Adv* **2020**, *10* (29), 16832–16843. https://doi.org/10.1039/D0RA02450C.

(64) Wang, M.; Rahimi, M.; Kumar, A.; Hariharan, S.; Choi, W.; Hatton, T. A. Flue Gas CO2 Capture via Electrochemically Mediated Amine Regeneration: System Design and Performance. *Appl Energy* **2019**, *255*, 113879. https://doi.org/https://doi.org/10.1016/j.apenergy.2019.113879.

(65) Mehta, V.; Cooper, J. S. Review and Analysis of PEM Fuel Cell Design and Manufacturing. *J Power Sources* **2003**, *114* (1), 32–53. https://doi.org/10.1016/S0378-7753(02)00542-6.

(66) Wang, Y.; Ruiz Diaz, D. F.; Chen, K. S.; Wang, Z.; Adroher, X. C. Materials, Technological Status, and Fundamentals of PEM Fuel Cells – A Review. *Materials Today* **2020**, *32*, 178–203. https://doi.org/10.1016/J.MATTOD.2019.06.005.

(67) Sharaf, O. Z.; Orhan, M. F. An Overview of Fuel Cell Technology: Fundamentals and Applications. *Renewable and Sustainable Energy Reviews* **2014**, *32*, 810–853. https://doi.org/10.1016/J.RSER.2014.01.012.

(68) Shiva Kumar, S.; Himabindu, V. Hydrogen Production by PEM Water Electrolysis – A Review. *Mater Sci Energy Technol* **2019**, *2* (3), 442–454. https://doi.org/10.1016/J.MSET.2019.03.002.

(69) Zhang, K.; Liang, X.; Wang, L.; Sun, K.; Wang, Y.; Xie, Z.; Wu, Q.; Bai, X.; Hamdy, M. S.; Chen, H.; Zou, X. Status and Perspectives of Key Materials for PEM Electrolyzer. *Nano Research Energy* **2022**, *1* (3), e9120032. https://doi.org/10.26599/NRE.2022.9120032.

(70) Bodner, M.; Hofer, A.; Hacker, V. H2 Generation from Alkaline Electrolyzer. *Wiley Interdiscip Rev Energy Environ* **2015**, *4* (4), 365–381. https://doi.org/10.1002/WENE.150.

(71) Friedlingstein, P.; Houghton, R. A.; Marland, G.; Hackler, J.; Boden, T. A.; Conway, T. J.; Canadell, J. G.; Raupach, M. R.; Ciais, P.; le Quere, C. Update on CO2 Emissions. *Nat Geosci* **2010**, *3* (12), 811.

(72) Shakun, J. D.; Clark, P. U.; He, F.; Marcott, S. A.; Mix, A. C.; Liu, Z.; Otto-Bliesner, B.; Schmittner, A.; Bard, E. Global Warming Preceded by Increasing Carbon Dioxide Concentrations during the Last Deglaciation. *Nature* **2012**, *484* (7392), 49.

(73) Cox, P. M.; Betts, R. A.; Jones, C. D.; Spall, S. A.; Totterdell, I. J. Acceleration of Global Warming Due to Carbon-Cycle Feedbacks in a Coupled Climate Model. *Nature* **2000**, *408* (6809), 184–187.

(74) Lashof, D. A.; Ahuja, D. R. Relative Contributions of Greenhouse Gas Emissions to Global Warming. *Nature* **1990**, *344* (6266), 529–531.

(75) le Quéré, C.; Andrew, R. M.; Canadell, J. G.; Sitch, S.; Korsbakken, J. I.; Peters, G. P.; Manning, A. C.; Boden, T. A.; Tans, P. P.; Houghton, R. A.; Keeling, R. F.; Alin, S.; Andrews, O. D.; Anthoni, P.; Barbero, L.; Bopp, L.; Chevallier, F.; Chini, L. P.; Ciais, P.; Currie, K.; Delire, C.; Doney, S. C.; Friedlingstein, P.; Gkritzalis, T.; Harris, I.; Hauck, J.; Haverd, V.; Hoppema, M.; Klein Goldewijk, K.; Jain, A. K.; Kato, E.; Körtzinger, A.; Landschützer, P.; Lefèvre, N.; Lenton, A.; Lienert, S.; Lombardozzi, D.; Melton, J. R.; Metzl, N.; Millero, F.; Monteiro, P. M. S.; Munro, D. R.; Nabel, J. E. M. S.; Nakaoka, S. I.; O'Brien, K.; Olsen, A.; Omar, A. M.; Ono, T.; Pierrot, D.; Poulter, B.; Rödenbeck, C.; Salisbury, J.; Schuster, U.; Schwinger, J.; Séférian, R.; Skjelvan, I.; Stocker, B. D.; Sutton, A. J.; Takahashi, T.; Tian, H.; Tilbrook, B.; van der Laan-Luijkx, I. T.; van der Werf, G. R.; Viovy, N.; Walker, A. P.; Wiltshire, A. J.; Zaehle, S. Global Carbon Budget 2016. *Earth Syst. Sci. Data* **2016**, *8* (2), 605–649. https://doi.org/10.5194/essd-8-605-2016.

(76) Stocker, T. *Climate Change 2013: The Physical Science Basis: Working Group I Contribution to the Fifth Assessment Report of the Intergovernmental Panel on Climate Change*; Cambridge University Press, 2014.

(77) Gattuso, J.-P.; Hansson, L. *Ocean Acidification*; Oxford University Press, 2011.

(78) Orr, J. C.; Fabry, V. J.; Aumont, O.; Bopp, L.; Doney, S. C.; Feely, R. A.; Gnanadesikan, A.; Gruber, N.; Ishida, A.; Joos, F.; Key, R. M.; Lindsay, K.; Maier-Reimer, E.; Matear, R.; Monfray, P.; Mouchet, A.; Najjar, R. G.; Plattner, G.-K.; Rodgers, K. B.; Sabine, C. L.; Sarmiento, J. L.; Schlitzer, R.; Slater, R. D.; Totterdell, I. J.; Weirig, M.-F.; Yamanaka, Y.; Yool, A. Anthropogenic Ocean Acidification over the Twenty-First Century and Its Impact on Calcifying Organisms. *Nature* **2005**, *437* (7059), 681–686. https://doi.org/http://www.nature.com/nature/journal/v437/n7059/suppinfo/nature04095_S1.html.

(79) Caldeira, K.; Wickett, M. E. Oceanography: Anthropogenic Carbon and Ocean PH. *Nature* **2003**, *425* (6956), 365.

(80) Edenhofer, O. *Climate Change 2014: Mitigation of Climate Change*; Cambridge University Press, 2015; Vol. 3.

(81) Keith, D. W. Why Capture CO_2 from the Atmosphere? *Science (1979)* **2009**, *325* (5948), 1654–1655. https://doi.org/10.1126/science.1175680.

(82) Lackner, K. S. Capture of Carbon Dioxide from Ambient Air. *European Physical Journal: Special Topics* **2009**, *176* (1), 93–106. https://doi.org/10.1140/epjst/e2009-01150-3.

(83) Lackner, K. S. The Thermodynamics of Direct Air Capture of Carbon Dioxide. *Energy* **2013**, *50*, 38–46. https://doi.org/https://doi.org/10.1016/j.energy.2012.09.012.

(84) Brethomé, F. M.; Williams, N. J.; Seipp, C. A.; Kidder, M. K.; Custelcean, R. Direct Air Capture of CO2 via Aqueous-Phase Absorption and Crystalline-Phase Release Using Concentrated Solar Power. *Nat Energy* **2018**, *3* (7), 553–559. https://doi.org/10.1038/s41560-018-0150-z.

(85) Mahmoudkhani, M.; Keith, D. W. Low-Energy Sodium Hydroxide Recovery for CO2 Capture from Atmospheric Air—Thermodynamic Analysis. *International Journal of Greenhouse Gas Control* **2009**, *3* (4), 376–384. https://doi.org/https://doi.org/10.1016/j.ijggc.2009.02.003.

(86) Lide, D. R. *CRC Handbook of Chemistry and Physics*; CRC press, 2004; Vol. 85.

(87) Kim, S.; Choi, M.; Kang, J. S.; Joo, H.; Park, B. H.; Sung, Y. E.; Yoon, J. Electrochemical Recovery of LiOH from Used CO2 Adsorbents. *Catal Today* **2021**, *359*, 83–89. https://doi.org/10.1016/J.CATTOD.2019.06.056.

(88) Rheinhardt, J. H.; Singh, P.; Tarakeshwar, P.; Buttry, D. A. Electrochemical Capture and Release of Carbon Dioxide. *ACS Energy Lett* **2017**, *2* (2), 454–461. https://doi.org/10.1021/acsenergylett.6b00608.

(89) Stucki, S.; Schuler, A.; Constantinescu, M. Coupled CO2 Recovery from the Atmosphere and Water Electrolysis: Feasibility of a New Process for Hydrogen Storage. *Int J Hydrogen Energy* **1995**, *20* (8), 653–663. https://doi.org/https://doi.org/10.1016/0360-3199(95)00007-Z.

(90) Rahimi, M.; Catalini, G.; Hariharan, S.; Wang, M.; Puccini, M.; Hatton, T. A. Carbon Dioxide Capture Using an Electrochemically Driven Proton Concentration Process. *Cell Rep Phys Sci* **2020**, 100033. https://doi.org/https://doi.org/10.1016/j.xcrp.2020.100033.

(91) Kuntke, P.; Rodríguez Arredondo, M.; Widyakristi, L.; ter Heijne, A.; Sleutels, T. H. J. A.; Hamelers, H. V. M.; Buisman, C. J. N. Hydrogen Gas Recycling for Energy Efficient Ammonia Recovery in Electrochemical Systems. *Environ Sci Technol* **2017**, *51* (5), 3110–3116. https://doi.org/10.1021/acs.est.6b06097.

(92) Kuntke, P.; Rodrigues, M.; Sleutels, T.; Saakes, M.; Hamelers, H. V. M.; Buisman, C. J. N. Energy-Efficient Ammonia Recovery in an Up-Scaled Hydrogen Gas Recycling Electrochemical System. *ACS Sustain Chem Eng* **2018**, *6* (6), 7638–7644. https://doi.org/10.1021/acssuschemeng.8b00457.

(93) Sander, R. Compilation of Henry's Law Constants (Version 4.0) for Water as Solvent. *Atmos. Chem. Phys* **2015**, *15* (8), 4399–4981.

(94) Wang, X.; Conway, W.; Burns, R.; McCann, N.; Maeder, M. Comprehensive Study of the Hydration and Dehydration Reactions of Carbon Dioxide in Aqueous Solution. *J Phys Chem A* **2010**, *114* (4), 1734–1740. https://doi.org/10.1021/jp909019u.

(95) Rodríguez Arredondo, M.; Kuntke, P.; ter Heijne, A.; Hamelers, H. V. M.; Buisman, C. J. N. Load Ratio Determines the Ammonia Recovery and Energy Input of an Electrochemical System. *Water Res* **2017**, *111*, 330–337. https://doi.org/https://doi.org/10.1016/j.watres.2016.12.051.

(96) Paz-Garcia, J. M.; Schaetzle, O.; Biesheuvel, P. M.; Hamelers, H. V. M. Energy from CO2 Using Capacitive Electrodes – Theoretical Outline and Calculation of Open Circuit Voltage. *J Colloid Interface Sci* **2014**, *418*, 200–207. https://doi.org/https://doi.org/10.1016/j.jcis.2013.11.081.

(97) Fasihi, M.; Efimova, O.; Breyer, C. Techno-Economic Assessment of CO2 Direct Air Capture Plants. *J Clean Prod* **2019**, *224*, 957–980. https://doi.org/https://doi.org/10.1016/j.jclepro.2019.03.086.

(98) Herrera, O. E.; Wilkinson, D. P.; Mérida, W. Anode and Cathode Overpotentials and Temperature Profiles in a PEMFC. *J Power Sources* **2012**, *198*, 132–142. https://doi.org/https://doi.org/10.1016/j.jpowsour.2011.09.042.

(99) *NASA Global Climate Change: Vital Signs*. https://climate.nasa.gov/vital-signs/carbon-dioxide/.

(100) Mora, C.; Spirandelli, D.; Franklin, E. C.; Lynham, J.; Kantar, M. B.; Miles, W.; Smith, C. Z.; Freel, K.; Moy, J.; Louis, L. v; Barba, E. W.; Bettinger, K.; Frazier, A. G.; Colburn Ix, J. F.; Hanasaki, N.; Hawkins, E.; Hirabayashi, Y.; Knorr, W.; Little, C. M.; Emanuel, K.; Sheffield, J.; Patz, J. A.; Hunter, C. L. Broad Threat to Humanity from Cumulative Climate Hazards Intensified by Greenhouse Gas Emissions. *Nat Clim Chang* **2018**, *8* (12), 1062–1071. https://doi.org/10.1038/s41558-018-0315-6.

(101) IPCC; Press, C. U. *Climate Change 2013: The Physical Science Basis. Contribution of Working Group I to the Fifth Assessment Report of the Intergovernmental Panel on Climate Change*; Stocker D. Qin G.-K.

Plattner M. Tignor S.K. Allen J. Boschung A. Nauels Y. Xia V. Bex and P.M. Midgley, T. F., Ed.; Cambridge University Press: Cambridge, United Kingdom and New York, NY, USA, 2013.

(102) MacDowell, N.; Florin, N.; Buchard, A.; Hallett, J.; Galindo, A.; Jackson, G.; Adjiman, C. S.; Williams, C. K.; Shah, N.; Fennell, P. An Overview of CO2 Capture Technologies. *Energy Environ Sci* **2010**, *3* (11), 1645–1669. https://doi.org/10.1039/C004106H.

(103) Minx, J. C.; Lamb, W. F.; Callaghan, M. W.; Fuss, S.; Hilaire, J.; Creutzig, F.; Amann, T.; Beringer, T.; de Oliveira Garcia, W.; Hartmann, J.; Khanna, T.; Lenzi, D.; Luderer, G.; Nemet, G. F.; Rogelj, J.; Smith, P.; Vicente Vicente, J. L.; Wilcox, J.; del Mar Zamora Dominguez, M. Negative Emissions—Part 1: Research Landscape and Synthesis. *Environmental Research Letters* **2018**, *13* (6), 63001. https://doi.org/10.1088/1748-9326/aabf9b.

(104) Fuss, S.; Lamb, W. F.; Callaghan, M. W.; Hilaire, J.; Creutzig, F.; Amann, T.; Beringer, T.; de Oliveira Garcia, W.; Hartmann, J.; Khanna, T.; Luderer, G.; Nemet, G. F.; Rogelj, J.; Smith, P.; Vicente, J. L. V.; Wilcox, J.; del Mar Zamora Dominguez, M.; Minx, J. C. Negative Emissions—Part 2: Costs, Potentials and Side Effects. *Environmental Research Letters* **2018**, *13* (6), 63002. https://doi.org/10.1088/1748-9326/aabf9f.

(105) Nemet, G. F.; Callaghan, M. W.; Creutzig, F.; Fuss, S.; Hartmann, J.; Hilaire, J.; Lamb, W. F.; Minx, J. C.; Rogers, S.; Smith, P. Negative Emissions—Part 3: Innovation and Upscaling. *Environmental Research Letters* **2018**, *13* (6), 63003. https://doi.org/10.1088/1748-9326/aabff4.

(106) Hanna, R.; Abdulla, A.; Xu, Y.; Victor, D. G. Emergency Deployment of Direct Air Capture as a Response to the Climate Crisis. *Nat Commun* **2021**, *12* (1). https://doi.org/10.1038/s41467-020-20437-0.

(107) Shi, X.; Xiao, H.; Azarabadi, H.; Song, J.; Wu, X.; Chen, X.; Lackner, K. S. Sorbents for the Direct Capture of CO2 from Ambient Air. *Angewandte Chemie International Edition* **2020**, *59* (18), 6984–7006. https://doi.org/https://doi.org/10.1002/anie.201906756.

(108) Goeppert, A.; Czaun, M.; May, R. B.; Prakash, G. K. S.; Olah, G. A.; Narayanan, S. R. Carbon Dioxide Capture from the Air Using a Polyamine Based Regenerable Solid Adsorbent. *J Am Chem Soc* **2011**, *133* (50), 20164–20167. https://doi.org/10.1021/ja2100005.

(109) Goeppert, A.; Zhang, H.; Czaun, M.; May, R. B.; Prakash, G. K. S.; Olah, G. A.; Narayanan, S. R. Easily Regenerable Solid Adsorbents Based on Polyamines for Carbon Dioxide Capture from the Air. *ChemSusChem* **2014**, *7* (5), 1386–1397. https://doi.org/https://doi.org/10.1002/cssc.201301114.

(110) Wang, J.; Huang, L.; Yang, R.; Zhang, Z.; Wu, J.; Gao, Y.; Wang, Q.; O'Hare, D.; Zhong, Z. Recent Advances in Solid Sorbents for CO2 Capture and New Development Trends. *Energy Environ Sci* **2014**, *7* (11), 3478–3518. https://doi.org/10.1039/C4EE01647E.

(111) Alesi Jr, W. R.; Kitchin, J. R. Evaluation of a Primary Amine-Functionalized Ion-Exchange Resin for CO2 Capture. *Ind Eng Chem Res* **2012**, *51* (19), 6907–6915.

(112) Parvazinia, M.; Garcia, S.; Maroto-Valer, M. CO2 Capture by Ion Exchange Resins as Amine Functionalised Adsorbents. *Chemical Engineering Journal* **2018**, *331*, 335–342.

(113) Buijs, W.; de Flart, S. Direct Air Capture of CO2 with an Amine Resin: A Molecular Modeling Study of the CO2 Capturing Process. *Ind Eng Chem Res* **2017**, *56* (43), 12297–12304.

(114) Wang, T.; Lackner, K. S.; Wright, A. Moisture Swing Sorbent for Carbon Dioxide Capture from Ambient Air. *Environ Sci Technol* **2011**, *45* (15), 6670–6675. https://doi.org/10.1021/es201180v.

(115) Yu, Q.; Delgado, J. de la P.; Veneman, R.; Brilman, D. W. F. Stability of a Benzyl Amine Based CO2 Capture Adsorbent in View of Regeneration Strategies. *Ind Eng Chem Res* **2017**, *56* (12), 3259–3269. https://doi.org/10.1021/acs.iecr.6b04645.

(116) Wang, T.; Lackner, K. S.; Wright, A. B. Moisture-Swing Sorption for Carbon Dioxide Capture from Ambient Air: A Thermodynamic Analysis. *Physical Chemistry Chemical Physics* **2013**, *15* (2), 504–514. https://doi.org/10.1039/C2CP43124F.

(117) Shu, Q.; Legrand, L.; Kuntke, P.; Tedesco, M.; Hamelers, H. V. M. Electrochemical Regeneration of Spent Alkaline Absorbent from Direct Air Capture. *Environ Sci Technol* **2020**, *54* (14), 8990–8998. https://doi.org/10.1021/acs.est.0c01977.

(118) Baumann, E. W. Thermal Decomposition of Amberlite IRA-400. *J Chem Eng Data* **1960**, *5* (3), 376–382. https://doi.org/10.1021/je60007a040.

(119) Hatch, M. J.; Lloyd, W. D. Preparation and Properties of a Neophyl Type Anion Exchange Resin. *J Appl Polym Sci* **1964**, *8* (4), 1659–1666. https://doi.org/https://doi.org/10.1002/app.1964.070080416.

(120) Butler, G. B.; Bunch, R. L.; Ingley, F. L. Preparation and Polymerization of Unsaturated Quaternary Ammonium Compounds. IV. Some Properties of the Polymers1. *J Am Chem Soc* **1952**, *74* (10), 2543–2547. https://doi.org/10.1021/ja01130a025.

(121) Tomoi, M.; Yamaguchi, K.; Ando, R.; Kantake, Y.; Aosaki, Y.; Kubota, H. Synthesis and Thermal Stability of Novel Anion Exchange Resins with Spacer Chains. *J Appl Polym Sci* **1997**, *64* (6), 1161–1167. https://doi.org/https://doi.org/10.1002/(SICI)1097-4628(19970509)64:6<1161::AID-APP16>3.0.CO;2-Z.

(122) Mamo, M.; Ginting, D.; Renken, R.; Eghball, B. Stability of Ion Exchange Resin Under Freeze–Thaw or Dry–Wet Environment. *Soil Science Society of America Journal* **2004**, *68* (2), 677–681. https://doi.org/https://doi.org/10.2136/sssaj2004.6770.

(123) Yu, Q.; Brilman, D. W. F. Design Strategy for CO2 Adsorption from Ambient Air Using a Supported Amine Based Sorbent in a Fixed Bed Reactor. *Energy Procedia* **2017**, *114*, 6102–6114. https://doi.org/https://doi.org/10.1016/j.egypro.2017.03.1747.

(124) Board, O. S.; National Academies of Sciences and Medicine, E. Negative Emissions Technologies and Reliable Sequestration: A Research Agenda. **2019**.

(125) Eigenberger, G.; Ruppel, W. Catalytic Fixed-Bed Reactors. In *Ullmann's Encyclopedia of Industrial Chemistry*. https://doi.org/https://doi.org/10.1002/14356007.b04_199.pub2.

(126) Yu, Q.; Brilman, W. A Radial Flow Contactor for Ambient Air CO2 Capture. *Applied Sciences* **2020**, *10* (3), 1080.

(127) Azarabadi, H.; Lackner, K. S. A Sorbent-Focused Techno-Economic Analysis of Direct Air Capture. *Appl Energy* **2019**, *250*, 959–975. https://doi.org/https://doi.org/10.1016/j.apenergy.2019.04.012.

(128) Deutz, S.; Bardow, A. Life-Cycle Assessment of an Industrial Direct Air Capture Process Based on Temperature–Vacuum Swing Adsorption. *Nat Energy* **2021**, *6* (2), 203–213. https://doi.org/10.1038/s41560-020-00771-9.

(129) IPCC. *Climate Change 2022: Mitigation of Climate Change. Contribution of Working Group III to the Sixth Assessment Report of the Intergovernmental Panel on Climate Change*; 2022. https://doi.org/10.1017/9781009157926.

(130) *Carbon Dioxide | Vital Signs – Climate Change: Vital Signs of the Planet*. https://climate.nasa.gov/vital-signs/carbon-dioxide/ (accessed 2022-10-04).

(131) Mercer, J. H. West Antarctic Ice Sheet and CO2 Greenhouse Effect: A Threat of Disaster. *Nature* **1978**, *271* (5643), 321–325. https://doi.org/10.1038/271321a0.

(132) Foster, G. L.; Rohling, E. J. Relationship between Sea Level and Climate Forcing by CO2 on Geological Timescales. *Proceedings of the National Academy of Sciences* **2013**, *110* (4), 1209–1214. https://doi.org/10.1073/pnas.1216073110.

(133) Urban, M. C. Accelerating Extinction Risk from Climate Change. *Science (1979)* **2015**, *348* (6234), 571–573. https://doi.org/10.1126/science.aaa4984.

(134) Galán-Martín, Á.; Vázquez, D.; Cobo, S.; mac Dowell, N.; Caballero, J. A.; Guillén-Gosálbez, G. Delaying Carbon Dioxide Removal in the European Union Puts Climate Targets at Risk. *Nat Commun* **2021**, *12* (1), 6490. https://doi.org/10.1038/s41467-021-26680-3.

(135) Gasser, T.; Guivarch, C.; Tachiiri, K.; Jones, C. D.; Ciais, P. Negative Emissions Physically Needed to Keep Global Warming below 2 °C. *Nat Commun* **2015**, *6* (1), 7958. https://doi.org/10.1038/ncomms8958.

(136) van Vuuren, D. P.; Deetman, S.; van Vliet, J.; van den Berg, M.; van Ruijven, B. J.; Koelbl, B. The Role of Negative CO2 Emissions for Reaching 2 °C—Insights from Integrated Assessment Modelling. *Clim Change* **2013**, *118* (1), 15–27. https://doi.org/10.1007/s10584-012-0680-5.

(137) S. Sanz-Pérez, E.; R. Murdock, C.; A. Didas, S.; W. Jones, C. Direct Capture of CO2 from Ambient Air. *Chem Rev* **2016**, *116* (19), 11840–11876. https://doi.org/10.1021/acs.chemrev.6b00173.

(138) Erans, M.; Sanz-Pérez, E. S.; Hanak, D. P.; Clulow, Z.; Reiner, D. M.; Mutch, G. A. Direct Air Capture: Process Technology, Techno-Economic and Socio-Political Challenges. *Energy Environ Sci* **2022**, *15* (4), 1360–1405. https://doi.org/10.1039/D1EE03523A.

(139) Elfving, J.; Kauppinen, J.; Jegoroff, M.; Ruuskanen, V.; Järvinen, L.; Sainio, T. Experimental Comparison of Regeneration Methods for CO2 Concentration from Air Using Amine-Based Adsorbent. *Chemical Engineering Journal* **2021**, *404*, 126337. https://doi.org/10.1016/J.CEJ.2020.126337.

(140) Hanna, R.; Abdulla, A.; Xu, Y.; Victor, D. G. Emergency Deployment of Direct Air Capture as a Response to the Climate Crisis. *Nat Commun* **2021**, *12* (1), 368. https://doi.org/10.1038/s41467-020-20437-0.

(141) Breyer, C.; Fasihi, M.; Bajamundi, C.; Creutzig, F. Direct Air Capture of CO2: A Key Technology for Ambitious Climate Change Mitigation. *Joule* **2019**, *3* (9), 2053–2057. https://doi.org/10.1016/J.JOULE.2019.08.010.

(142) Keith, D. W.; Holmes, G.; st. Angelo, D.; Heidel, K. A Process for Capturing CO2 from the Atmosphere. *Joule* **2018**, *2* (8), 1573–1594. https://doi.org/10.1016/J.JOULE.2018.05.006.

(143) Sharifian, R.; Wagterveld, R. M.; Digdaya, I. A.; Xiang, C.; Vermaas, D. A. Electrochemical Carbon Dioxide Capture to Close the Carbon Cycle. *Energy Environ Sci* **2021**, *14* (2), 781–814. https://doi.org/10.1039/D0EE03382K.

(144) Gilliam, R. J.; Boggs, B. K.; Decker, V.; Kostowskyj, M. A.; Gorer, S.; Albrecht, T. A.; Way, J. D.; Kirk, D. W.; Bard, A. J. Low Voltage Electrochemical Process for Direct Carbon Dioxide Sequestration. *J Electrochem Soc* **2012**, *159* (5), B627–B628. https://doi.org/10.1149/2.033206jes.

(145) Jiang, C.; Li, S.; Zhang, D.; Yang, Z.; Yu, D.; Chen, X.; Wang, Y.; Xu, T. Mathematical Modelling and Experimental Investigation of CO2 Absorber Recovery Using an Electro-Acidification Method. *Chemical Engineering Journal* **2019**, *360*, 654–664. https://doi.org/10.1016/J.CEJ.2018.12.006.

(146) Jin, S.; Wu, M.; Jing, Y.; Gordon, R. G.; Aziz, M. J. Low Energy Carbon Capture via Electrochemically Induced PH Swing with Electrochemical Rebalancing. *Nature Communications 2022 13:1* **2022**, *13* (1), 1–11. https://doi.org/10.1038/s41467-022-29791-7.

(147) Eisaman, M. D.; Alvarado, L.; Larner, D.; Wang, P.; Garg, B.; Littau, K. A. CO2 Separation Using Bipolar Membrane Electrodialysis. *Energy Environ Sci* **2011**, *4* (4), 1319–1328. https://doi.org/10.1039/C0EE00303D.

(148) Iizuka, A.; Hashimoto, K.; Nagasawa, H.; Kumagai, K.; Yanagisawa, Y.; Yamasaki, A. Carbon Dioxide Recovery from Carbonate Solutions Using Bipolar Membrane Electrodialysis. *Sep Purif Technol* **2012**, *101*, 49–59. https://doi.org/10.1016/J.SEPPUR.2012.09.016.

(149) Ye, W.; Huang, J.; Lin, J.; Zhang, X.; Shen, J.; Luis, P.; van der Bruggen, B. Environmental Evaluation of Bipolar Membrane Electrodialysis for NaOH Production from Wastewater: Conditioning NaOH as a CO2 Absorbent. *Sep Purif Technol* **2015**, *144*, 206–214. https://doi.org/10.1016/J.SEPPUR.2015.02.031.

(150) Valluri, S.; Kawatra, S. K. Reduced Reagent Regeneration Energy for CO2 Capture with Bipolar Membrane Electrodialysis. *Fuel Processing Technology* **2021**, *213*, 106691. https://doi.org/10.1016/J.FUPROC.2020.106691.

(151) Shu, Q.; Legrand, L.; Kuntke, P.; Tedesco, M.; v. M. Hamelers, H. Electrochemical Regeneration of Spent Alkaline Absorbent from Direct Air Capture. *Environ Sci Technol* **2020**, *54* (14), 8990–8998. https://doi.org/10.1021/acs.est.0c01977.

(152) Shu, Q.; Haug, M.; Tedesco, M.; Kuntke, P.; v. M. Hamelers, H. Direct Air Capture Using Electrochemically Regenerated Anion Exchange Resins. *Environ Sci Technol* **2022**, *56* (16), 11559–11566. https://doi.org/10.1021/acs.est.2c01944.

(153) Sabatino, F.; Mehta, M.; Grimm, A.; Gazzani, M.; Gallucci, F.; Jan Kramer, G.; van Sint Annaland, M. Evaluation of a Direct Air Capture Process Combining Wet Scrubbing and Bipolar Membrane Electrodialysis. *Ind Eng Chem Res* **2020**, *59* (15), 7007–7020. https://doi.org/10.1021/acs.iecr.9b05641.

(154) Fang, M.; Wang, Z.; Yan, S.; Cen, Q.; Luo, Z. CO2 Desorption from Rich Alkanolamine Solution by Using Membrane Vacuum Regeneration Technology. *International Journal of Greenhouse Gas Control* **2012**, *9*, 507–521. https://doi.org/10.1016/J.IJGGC.2012.05.013.

(155) Wang, Z.; Fang, M.; Ma, Q.; Zhao, Z.; Wang, T.; Luo, Z. Membrane Stripping Technology for CO2 Desorption from CO2-Rich Absorbents with Low Energy Consumption. *Energy Procedia* **2014**, *63*, 765–772. https://doi.org/10.1016/J.EGYPRO.2014.11.085.

(156) Sabatino, F.; Gazzani, M.; Gallucci, F.; van Sint Annaland, M. Modeling, Optimization, and Techno-Economic Analysis of Bipolar Membrane Electrodialysis for Direct Air Capture Processes. *Ind Eng Chem Res* **2022**, *0* (0). https://doi.org/10.1021/acs.iecr.2c00889.

(157) W. Jeremiasse, A.; v. M. Hamelers, H.; Mieke Kleijn, J.; J. N. Buisman, C. Use of Biocompatible Buffers to Reduce the Concentration Overpotential for Hydrogen Evolution. *Environ Sci Technol* **2009**, *43* (17), 6882–6887. https://doi.org/10.1021/es9008823.

(158) Peng, Z. G.; Lee, S. H.; Zhou, T.; Shieh, J. J.; Chung, T. S. A Study on Pilot-Scale Degassing by Polypropylene (PP) Hollow Fiber Membrane Contactors. *Desalination* **2008**, *234* (1–3), 316–322. https://doi.org/10.1016/J.DESAL.2007.09.100.

(159) Angulo, A.; van der Linde, P.; Gardeniers, H.; Modestino, M.; Fernández Rivas, D. Influence of Bubbles on the Energy Conversion Efficiency of Electrochemical Reactors. *Joule* **2020**, *4* (3), 555–579. https://doi.org/10.1016/J.JOULE.2020.01.005.

(160) Zhao, X.; Ren, H.; Luo, L. Gas Bubbles in Electrochemical Gas Evolution Reactions. *Langmuir* **2019**, *35* (16), 5392–5408. https://doi.org/10.1021/acs.langmuir.9b00119.

(161) Taqieddin, A.; Nazari, R.; Rajic, L.; Alshawabkeh, A. Review—Physicochemical Hydrodynamics of Gas Bubbles in Two Phase Electrochemical Systems. *J Electrochem Soc* **2017**, *164* (13), E448–E459. https://doi.org/10.1149/2.1161713jes.

(162) Onyebuchi, V. E.; Kolios, A.; Hanak, D. P.; Biliyok, C.; Manovic, V. A Systematic Review of Key Challenges of CO2 Transport via Pipelines. *Renewable and Sustainable Energy Reviews* **2018**, *81*, 2563–2583. https://doi.org/10.1016/J.RSER.2017.06.064.

(163) Aminu, M. D.; Nabavi, S. A.; Rochelle, C. A.; Manovic, V. A Review of Developments in Carbon Dioxide Storage. *Appl Energy* **2017**, *208*, 1389–1419. https://doi.org/10.1016/J.APENERGY.2017.09.015.

(164) van de Ven, J. D.; Li, P. Y. Liquid Piston Gas Compression. *Appl Energy* **2009**, *86* (10), 2183–2191. https://doi.org/10.1016/J.APENERGY.2008.12.001.

(165) Krol, J. J.; Wessling, M.; Strathmann, H. Concentration Polarization with Monopolar Ion Exchange Membranes: Current–Voltage Curves and Water Dissociation. *J Memb Sci* **1999**, *162* (1–2), 145–154. https://doi.org/10.1016/S0376-7388(99)00133-7.

(166) Luo, T.; Abdu, S.; Wessling, M. Selectivity of Ion Exchange Membranes: A Review. *J Memb Sci* **2018**, *555*, 429–454. https://doi.org/10.1016/J.MEMSCI.2018.03.051.

(167) Gouedard, C.; Picq, D.; Launay, F.; Carrette, P. L. Amine Degradation in CO2 Capture. I. A Review. *International Journal of Greenhouse Gas Control* **2012**, *10*, 244–270. https://doi.org/10.1016/J.IJGGC.2012.06.015.

(168) Rey, A.; Gouedard, C.; Ledirac, N.; Cohen, M.; Dugay, J.; Vial, J.; Pichon, V.; Bertomeu, L.; Picq, D.; Bontemps, D.; Chopin, F.; Carrette, P. L. Amine Degradation in CO2 Capture. 2. New Degradation Products of MEA. Pyrazine and Alkylpyrazines: Analysis, Mechanism of Formation and Toxicity. *International Journal of Greenhouse Gas Control* **2013**, *19*, 576–583. https://doi.org/10.1016/J.IJGGC.2013.10.018.

(169) Gouedard, C.; Rey, A.; Cuzuel, V.; Brunet, J.; Delfort, B.; Picq, D.; Dugay, J.; Vial, J.; Pichon, V.; Launay, F.; Assam, L.; Ponthus, J.; Carrette, P. L. Amine Degradation in CO2 Capture. 3. New Degradation Products of MEA in Liquid Phase: Amides and Nitrogenous Heterocycles. *International Journal of Greenhouse Gas Control* **2014**, *29*, 61–69. https://doi.org/10.1016/J.IJGGC.2014.07.013.

(170) Lepaumier, H.; Picq, D.; Carrette, P.-L. New Amines for CO2 Capture. II. Oxidative Degradation Mechanisms. *Industrial & Engineering Chemistry Research* **2009**, *48* (20), 9068–9075. https://doi.org/10.1021/ie9004749.

(171) Shi, L.; Zhao, Y.; Matz, S.; Gottesfeld, S.; Setzler, B. P.; Yan, Y. A Shorted Membrane Electrochemical Cell Powered by Hydrogen to Remove CO2 from the Air Feed of Hydroxide Exchange Membrane Fuel Cells. *Nature Energy 2022 7:3* **2022**, *7* (3), 238–247. https://doi.org/10.1038/s41560-021-00969-5.

(172) Liu, J.; Xiong, H.; Tong, S.; Tang, Y.; Chen, Y.; Sun, Y.; Yang, X.; Wan, P.; Khan, Z. U. H. Hydrogen-Motivated Electrolysis of Sodium Carbonate with Extremely Low Cell Voltage. *Chemical Communications* **2018**, *54* (29), 3582–3585. https://doi.org/10.1039/C8CC00812D.

(173) P. Muroyama, A.; Gubler, L. Carbonate Regeneration Using a Membrane Electrochemical Cell for Efficient CO2 Capture. *ACS Sustainable Chemistry & Engineering* **2022**, *10* (49), 16113–16117. https://doi.org/10.1021/acssuschemeng.2c04175.

(174) Shu, Q.; Haug, M.; Tedesco, M.; Kuntke, P.; v. M. Hamelers, H. Direct Air Capture Using Electrochemically Regenerated Anion Exchange Resins. *Environ Sci Technol* **2022**, *56* (16), 11559–11566. https://doi.org/10.1021/acs.est.2c01944.

(175) Sigrist, L.; Dossenbach, O.; Ibl, N. *On the Conductivity and Void Fraction of Gas Dispersions in Electrolyte Solutions*; 1980; Vol. 10.

(176) Angulo, A.; van der Linde, P.; Gardeniers, H.; Modestino, M.; Fernández Rivas, D. Influence of Bubbles on the Energy Conversion Efficiency of Electrochemical Reactors. *Joule* **2020**, *4* (3), 555–579. https://doi.org/10.1016/J.JOULE.2020.01.005.

(177) Zhao, X.; Ren, H.; Luo, L. Gas Bubbles in Electrochemical Gas Evolution Reactions. *Langmuir* **2019**, *35* (16), 5392–5408. https://doi.org/10.1021/acs.langmuir.9b00119.

(178) Taqieddin, A.; Allshouse, M. R.; Alshawabkeh, A. N. Mathematical Formulations of Electrochemically Gas-Evolving Systems. *J Electrochem Soc* **2018**, *165* (13), E694–E711. https://doi.org/10.1149/2.0791813jes.

(179) Pawlowski, S.; Crespo, J. G.; Velizarov, S. Pressure Drop in Reverse Electrodialysis: Experimental and Modeling Studies for Stacks with Variable Number of Cell Pairs. *J Memb Sci* **2014**, *462*, 96–111. https://doi.org/10.1016/J.MEMSCI.2014.03.020.

(180) Yan, L.; Bao, J.; Shao, Y.; Wang, W. An Electrochemical Hydrogen-Looping System for Low-Cost CO2Capture from Seawater. *ACS Energy Lett* **2022**, *7* (6), 1947–1952. https://doi.org/10.1021/acsenergylett.2c00396.

(181) Shimpalee, S.; Beuscher, U.; van Zee, J. W. Analysis of GDL Flooding Effects on PEMFC Performance. *Electrochim Acta* **2007**, *52* (24), 6748–6754. https://doi.org/10.1016/J.ELECTACTA.2007.04.115.

(182) Lasia, A. Hydrogen Evolution Reaction. *Handbook of fuel cells* **2010**, *2*, 416–440.

(183) Harrison, J. A.; Kuhn, A. T. The Role of Gas Bubble Formation in the Electro-Catalysis of the Hydrogen Evolution Reaction. *Surface Technology* **1983**, *19* (3), 249–259. https://doi.org/10.1016/0376-4583(83)90029-8.

(184) *Trees help tackle climate change — European Environment Agency*. https://www.eea.europa.eu/articles/forests-health-and-climate-change/key-facts/trees-help-tackle-climate-change (accessed 2023-02-17).

(185) *Orca is Climeworks' new large-scale carbon dioxide removal plant*. https://climeworks.com/roadmap/orca (accessed 2023-02-17).

(186) Wang, T.; Liu, J.; Fang, M.; Luo, Z. A Moisture Swing Sorbent for Direct Air Capture of Carbon Dioxide: Thermodynamic and Kinetic Analysis. *Energy Procedia* **2013**, *37*, 6096–6104. https://doi.org/10.1016/J.EGYPRO.2013.06.538.

(187) Li, H.; Tang, Y.; Wang, Z.; Shi, Z.; Wu, S.; Song, D.; Zhang, J.; Fatih, K.; Zhang, J.; Wang, H.; Liu, Z.; Abouatallah, R.; Mazza, A. A Review of Water Flooding Issues in the Proton Exchange Membrane Fuel Cell. *J Power Sources* **2008**, *178* (1), 103–117. https://doi.org/10.1016/J.JPOWSOUR.2007.12.068.

(188) Rabiee, H.; Ge, L.; Zhang, X.; Hu, S.; Li, M.; Yuan, Z. Gas Diffusion Electrodes (GDEs) for Electrochemical Reduction of Carbon Dioxide, Carbon Monoxide, and Dinitrogen to Value-Added Products: A Review. *Energy Environ Sci* **2021**, *14* (4), 1959–2008.

(189) Clifford, D.; Weber, W. J. The Determinants of Divalent/Monovalent Selectivity in Anion Exchangers. *Reactive Polymers, Ion Exchangers, Sorbents* **1983**, *1* (2), 77–89. https://doi.org/10.1016/0167-6989(83)90040-5.

(190) Bauska, T. K.; Marcott, S. A.; Brook, E. J. Abrupt Changes in the Global Carbon Cycle during the Last Glacial Period. *Nat Geosci* **2021**, *14* (2), 91–96. https://doi.org/10.1038/s41561-020-00680-2.

(191) Din, I. U.; Shaharun, M. S.; Alotaibi, M. A.; Alharthi, A. I.; Naeem, A. Recent Developments on Heterogeneous Catalytic CO2 Reduction to Methanol. *Journal of CO2 Utilization* **2019**, *34*, 20–33. https://doi.org/10.1016/J.JCOU.2019.05.036.

(192) Küngas, R. Review—Electrochemical CO2 Reduction for CO Production: Comparison of Low- and High-Temperature Electrolysis Technologies. *J Electrochem Soc* **2020**, *167* (4), 044508. https://doi.org/10.1149/1945-7111/ab7099.

(193) Kibria, M. G.; Edwards, J. P.; Gabardo, C. M.; Dinh, C.-T.; Seifitokaldani, A.; Sinton, D.; Sargent, E. H. Electrochemical CO2 Reduction into Chemical Feedstocks: From Mechanistic Electrocatalysis Models to System Design. *Advanced Materials* **2019**, *31* (31), 1807166. https://doi.org/https://doi.org/10.1002/adma.201807166.

(194) Han, N.; Ding, P.; He, L.; Li, Y.; Li, Y. Promises of Main Group Metal–Based Nanostructured Materials for Electrochemical CO2 Reduction to Formate. *Adv Energy Mater* **2020**, *10* (11), 1902338. https://doi.org/https://doi.org/10.1002/aenm.201902338.

(195) Sleutels, T.; Sebastião Bernardo, R.; Kuntke, P.; Janssen, M.; J. N. Buisman, C.; v. M. Hamelers, H. Enhanced Phototrophic Biomass Productivity through Supply of Hydrogen Gas. *Environmental Science & Technology Letters* **2020**, *7* (11), 861–865. https://doi.org/10.1021/acs.estlett.0c00718.

(196) Daneshvar, E.; Wicker, R. J.; Show, P. L.; Bhatnagar, A. Biologically-Mediated Carbon Capture and Utilization by Microalgae towards Sustainable CO2 Biofixation and Biomass Valorization – A Review. *Chemical Engineering Journal* **2022**, *427*, 130884. https://doi.org/10.1016/J.CEJ.2021.130884.

Acknowledgement

On the 3rd of July 2018, I received the offer email for this PhD position while playing ping pong with Louis. Over the next four and a half years, just like the ball was pushed forward by the bat and carried by air to reach the other side of the table, I was pushed and carried by people around me to finish my PhD.

First and foremost, I would like to express my deepest appreciation to my supervision team. My promotor **Bert**, thank you for your trust and giving me the opportunity to do this PhD. I admire your research sensitivity and enthusiasm in your work which always motivates me to work harder. I was always holding back and stuck in my own thoughts, but you encouraged me to express myself and speak up for my opinions. You also taught me how to deal with my thoughts by walking or cycling. I will always remember the saying you told me, "Like other people are walking their dogs, I am walking my soul". My copromotor **Philipp**, thank you for always being available whenever I need help. The initial setup would not have been finished so fast without you, and I also learned a lot from your experience in the lab. Outside work, thank you for inviting me to dinners with your family and constantly motivating me during the Elfstedentocht. My supervisor **Michele**, thank you for pushing things forward and making my work more structured. Thank you for involving me in all the research-related activities, like giving a presentation to a company or reviewing a manuscript. I am inspired and motivated by your enterprising spirit and continuous improvement, which I believe would benefit me significantly. This appreciation also extends to **Cees** and **Johannes** for founding a great place as Wetsus.

I am also grateful to the theme members of the Sustainable Carbon Cycle theme. **Louis**, probably one of the best decisions I have made during my master's was working with you for my master's thesis. Thank you for leading me into the field of electrochemistry and carbon capture, bringing me to the meeting with Bert, and listening to my frustrations on the phone. I will always remember those days when we worked in the lab until 7 pm, played ping pong until Wetsus was closed, and then talked about work and life for another hour outside Wetsus. **Slawomir**, thank you for all the suggestions you have given me since my master's thesis. Your enthusiasm for working in the lab has motivated me a lot. **Sara Vallejo**, thank you for giving me the space to finish my thesis first while you had to handle all kinds of business on ConsenCUS by yourself. **Michel**, thank you for always asking challenging questions and helping me with some technical issues in the lab. **Robert de Kler**, thank you for connecting me to others when I felt lost at my first-ever international conference. And other theme members, thank you for the fruitful discussions during the theme meetings.

This dissertation would not be possible without the efforts of my lovely students, **Francesco**, **Ivo**, **Jeroen**, **Jinlin**, **Marina**, and **Philip**. Thank you for all your hard work and company at different stages of my PhD. Because of you, I knew I was not alone whenever I had a problem in the lab. I am grateful to work with you and learn from you.

I am also thankful to the technical team (**Wim**, **John**, **Jan Tuinstra**, **Ernst**, **Jan Jurjen**, **Harm**, **Wiebe**, and **Johan**) and the analytical team (**Jelmer**, **Mieke**, **Marianne**, **Jan Willem**, and **Lisette**). Especially John, thanks for all your help on my setup, you are always very fast to achieve what I want at the setup. And Wim, thank you for checking all the solutions for me to run experiments using outdoor air. Thanks should also go to the other departments at Wetsus (**Jeanette**, **Jannie**, **Roely**, **Marnejaeike**, **Danique**, **Hester**, **Rienk**, **Anke**, **Nynke**, **Alexander**, **Jan de Groot,** and **Gerrit**), thank you for your help and support during the past few years. Then the people from the Canteen, **Gerben**, **Catharina**, and **Karin**, thank you for all the sandwiches you prepared and the wonderful time we had in the PV. I want to extend my gratitude to **Liesbeth** and other colleagues from **ETE Office**, thank you for your time and effort to take care of all my business from the university side.

Then I would like to thank my officemates. The generation before me, **Caspar**, **Raquel**, **Gijs**, **Sandra**, and **Hakan**, thank you all for the fun we had, the poems we wrote for Sinterklaas, the champions we got, and the foam darts we shot around the office. And the new generation, **Evelyn**, I am grateful to share with you this PhD journey from day zero. **Sara Pinela**, thank you for being the considerate one and the one always taking care. **Sebastian**, thank you for the sane and insane talks, the joy you brought, and the sweaty Just Dance nights. Although saying a lot "I don't want to work" yourself, you motivated me when I didn't feel like working and pushed me when I had tasks to finish. I also miss hearing your rankings during our breaks. **Ha**, thank you for never being really mad at me even though you always got scared by me, and all the treats you brought from Italy or Vietnam seemed to be never finished. **Sam**, thank you for always being willing to help. One day, I will go climbing with you. **Asala**, thank you for the active vibe you bring to the office. **Elfy**, thank you for remaining calm when I speak my broken Dutch to you in a weird accent, sharing cookies all the time, and inviting me to play Jenga in the old office. And my new officemates on the second floor, **Sarah**, I appreciate all the "Bert information" we could share when he was extremely busy. **Lucía**, thank you for sharing my stressful and happy moments. The joy that you bring to the office always gives me energy. **Alex**, thank you for being so considerate when I was busy finishing my thesis. I really enjoyed the talks we had in the office.

My "North goes South" group, **Mariana**, **João**, **Margo**, **Sanne**. From A1 course to Bath winter school, from Leeuwarden to Wageningen, from Zandvoort to Azores, we cycled, cooked, played, and talked. We welcomed New Year standing on chairs and eating raisins, we climbed Pico and walked cows on the island, we celebrated my birthday outside Utrecht Centraal. I am extremely grateful to have you and for all the moments we shared. My dearest paranymphs, Mariana, thank you for involving me in all kinds of activities and always taking care of me. Although our communication styles are so different, we have many values in common, and probably that's why we are friends. I am deeply thankful for the extra phone calls you tried to check on me. João, thank you for listening to my complaints and supporting

me during many of my difficult times during the PhD. All the guitar practices and cycling days/weekends with you are my precious memory.

Chris and **Ragne**, thank you for all the talks we had, all the games we played, and all the excitement or disappointment we shared. We walked at the lakes during lockdown time when I had to keep 1.5 m from you, we went to group lessons in the gym where "down dog" became a routine, and we cleared "It Takes Two" within a weekend with lots of marveling and screaming. It was an absolute pleasure to have you together on this PhD journey. Chris, you have grown from the boy who wanted to take his beer mug back to someone who can represent Wetsus. But you have always been the man I look up to, I have learned so much from you, and I believe there is still more to learn. Ragne, we share many things in common, from talents to communication style, from theme to supervision team, so we have so many things to share. I cannot appreciate more having you there whenever I am confused about work or life.

To my other colleagues and friends, **Catarina**, thank you for all the talks, all the barbecue invites, and all the time being the sane one. **Paulina**, thank you for the hugs and all the sweet talks. **Carlo**, thank you for being considerate and playing those beautiful piano pieces. **Barbara**, thank you for the company in Bath and all the catch-up talks over the years. **Geert Jan**, thank you for your company to play squash. And many others, **Thomas**, **Amanda**, **Nandini**, **Antony**, **Shuyana**, **Kestral**, **Daniele**, **Olga B.**, **Olga S.**, **Vania**, **Sophie**, **Marta**, **Pieter**, **Dhyana**, **Edward**, **Nouran**, **Ruben**, **Maarten**, **Jolanda**, **Wokke**, **Paraschos**, **Nelleke**, **Diego**, thank you for all the time we spent together and the joy you brought.

感谢莱瓦顿车友会的各位师傅们。**叶师傅**和**雷师傅**，谢谢你们给了我在荷兰的第一个家，帮助我融入这边的生活。在我懒得做饭时，你们会和我分享你们做的美味大餐（叶师傅厨艺全荷第一！）；在我面临选择时，你们会给我真诚且实用的建议。**冰囡**，感谢你那些年剥过的蒜，洗过的碗，以及每次我去瓦村时的收留。你给我的印象总是从容而自若，这也让我卸下了很多的包袱。**妍玥**，谢谢你的信任，愿意将你的烦心事和我分享，也谢谢你每一次旅途的陪伴。**高风**，谢谢你向我展示了你充满活力的生活方式。**泽馨**，感谢你包过的饺子，蒸过的包子，以及每一次节日团聚时带给我如家般的温暖；也谢谢 **Mia** 每次见面时带给我的快乐。

还有那些在这座遥远的城市里或短暂或长久的相遇。感谢**梦艺**，**晓鲁**，**浅姐**，**婉蓉**，**大祺哥**，**陈阳**，和**老张**在硕士期间的陪伴和帮助，两年时间的一起学习和成长让我有了留在这里读博的底气。**琬笛，**谢谢你在 Wetsus 时陪我打过的乒乓球。**张力**，谢谢你让我看到的成熟和智慧。**晓夏**，感谢你让我看到你对于你喜欢的工作的热情。**时濛**，谢谢你和我一起吐槽我们的项目，以及你在 Wetsus 时带来的欢乐。**炽昌**，谢谢你的信任和你带给我的成长。**亮忻**，我在实验室的"邻居"，每次你富有热情的分享你的实验进展都会鼓舞我更努力的工作。**科岑**，时而稚气，时而老成，感谢你带来的每一个欢笑时光，也感谢你总是很乐意帮忙。**士轩**，你的独立，成熟，热心让我钦佩。不论是在骑车时，还是工作场合，有你在的时候我总觉

得很安心。**林牧**，你对工作的投入也激励着我不断前行，也谢谢你给我的空间和信任。**张潇**和**艺洲**，我的资深麻友和火锅专家，谢谢你们让我每一次的局都玩得很开心；潇的热情，艺洲的积极乐观，让我毫无压力，放松惬意。**烁光**，工作上，你认真负责，一丝不苟。生活中，你不急不躁，才华横溢。每次和你的接触都能带给我新的思考，感谢你，让我在一次又一次的自我反馈中成长。**怡程**，感谢你超强的执行力，我原以为春晖杯只是你随口一提的玩笑，在你的推动下，我们成功入围并依然在积极讨论未来的可能性。感谢你的成熟和果敢，让我也学着慢慢地成长。**裴**，既然我爸都能认错，那我俩一定兄弟了。谢谢你让我有机会从另一个角度认识我自己，不断反思，不断成长。谢谢你的陪伴，在去瓦村的火车上，在布拉格的酒馆里，在无数的店铺中，在骑行时路过的田间地头。**玉佳**，那时你住在北边很远的地方，那晚你没骑车，我送你回家。路很远，我们走了差不多一个小时。后来你搬家了，离 Wetsus 近了，送你回家的路又走了几年。荷兰很平，这条路却不是一直都好走，有争吵，有冷战，有泪水。但每一次的崎岖，都让我们变得更加坚强，更加紧密。谢谢你的不离不弃，谢谢你的真诚坦然，谢谢你的大度包容。因为有你，在这异国他乡，我便不再彷徨。

以及那些在远方的朋友们。**李成林**，谢谢你每次在上海的招待，给了我归心和离愁的缓冲带。我们见证了彼此从大学以来一路的成长，也共同憧憬着更加美好的未来。感谢你给的包容，让我觉得我的梦想有了容身之所。**沛哥**，虽然见面不多，但从小一起长大的情谊却没有改变。每次见你，总是可以毫无顾忌的侃侃过去，期望未来。以及人在美国，数不清有多少年没见过的**柳哥**，虽然距离很远，时间很长，但每次和你打电话时就像从来没分开过，谈谈工作，聊聊家常，我劝你来欧洲，你劝我去美国，好不和谐。还有永远约不到，却时常关心我情况的**胡来**，那些一起长大的玩伴，**浩宇**，**雨佳**，**安琪**，谢谢你们让我在国内的时光多了一些色彩。

最后我想感谢我的家人们。谢谢**爸爸**，那个无时无刻不在支持着我的人，那个为我自豪为我骄傲的人，也是那个爱我至深却不知如何表达的人。每次只有我俩的通话，你总是绞尽脑汁寻找话题；每次察觉到我的不开心，你总是会发来信息慰问；每次遇到人生的难题，你也给予了我充分的信任和尊重。谢谢**妈妈**，冷静地接收着我那些好的不好的情绪，耐心地倾听着我稀松琐碎的日常。谢谢你每周在电话那端陪我做家务，陪我逛超市，陪我散步。谢谢爸爸妈妈，是你们给了我独自在外闯荡的勇气和面对纷纷扰扰坚持自我的决心。谢谢**奶奶**，视我如珍宝，给了我无条件的爱。谢谢**外公外婆**对我的偏爱，外婆总是让我早点回国，身边的外公却连忙制止，提醒我工作最重要。谢谢家里的兄弟姐妹们，**大哥**，**二哥**，**蓉姐**，**艳子**，**龙哥**，**纪元**，**胡婷**，**胡馨**，**丁勇**，有你们在，回家的时候总是不会无聊；也因为有你们在，让我远在他国时少了几分忧虑。

Qingdian 束

Leeuwarden, May 2023

Publications and patent

In relation to this thesis:

Shu, Q., Legrand, L., Kuntke, P., Tedesco, M., & Hamelers, H. V. M. (2020). Electrochemical Regeneration of Spent Alkaline Absorbent from Direct Air Capture. *Environmental Science and Technology*, *54*(14). https://doi.org/10.1021/acs.est.0c01977

Shu, Q., Haug, M., Tedesco, M., Kuntke, P., & Hamelers, H. V. M. (2022). Direct Air Capture Using Electrochemically Regenerated Anion Exchange Resins. *Environmental Science and Technology*, *56*(16). https://doi.org/10.1021/acs.est.2c01944

Shu, Q., Sin C. S., Tedesco, M., Hamelers, H. V. M., & Kuntke, P. (2023). Optimization of an electrochemical direct air capture process with decreased CO2 desorption pressure and addition of background electrolyte. *Under review*.

Shu, Q., Tedesco, M., Kuntke, P., & Hamelers, H. V. M. (2023). Process layouts and parameters impacting electrochemical direct air capture process. *In preparation for submission*.

Hamelers, H. V. M., Tedesco, M., & **Shu, Q.** "Electrochemical device, system and method for electrochemical recovery and/or regeneration of carbon dioxide from a stream", NL patent NL2025044.

Other publication:

Legrand, L., **Shu, Q.**, Tedesco, M., Dykstra, J. E., & Hamelers, H. V. M. (2020). Role of ion exchange membranes and capacitive electrodes in membrane capacitive deionization (MCDI) for CO2 capture. *Journal of Colloid and Interface Science*, *564*, 478–490. https://doi.org/https://doi.org/10.1016/j.jcis.2019.12.039

About the author

Qingdian Shu was born in Anhui, China on 5 April 1994. In 2009, he started his bachelor's study in Anhui University of Technology, specialized in Water Supply and Sewage Engineering. After graduation, he took a gap year and then worked at Shucheng Urban and Rural Planning and Design Institute as an assistant designer. In 2016, he continued to study Water Technology at Wetsus Academy in the Netherlands (joined master's degree of Wageningen University, University of Groningen, and University of Twente). He wrote a master thesis on the optimization of a Membrane Capacitive Deionization (MCDI) system for CO_2 capture. Inspired by applying electrochemical methods in carbon capture, in September 2018, he started his Ph.D. project in Sustainable Carbon Cycle theme at Wetsus as a Ph.D. candidate from Wageningen University. During his Ph.D., he designed and developed an electrochemical Direct Air Capture (DAC) process, and the results obtained are presented in this dissertation.

Netherlands Research School for the
Socio-Economic and Natural Sciences of the Environment

D I P L O M A

for specialised PhD training

The Netherlands research school for the
Socio-Economic and Natural Sciences of the Environment
(SENSE) declares that

Qingdian Shu

born on 5 April 1994, in Anhui, China

has successfully fulfilled all requirements of the
educational PhD programme of SENSE.

Wageningen, 2 June 2023

Chair of the SENSE board

Prof. dr. Martin Wassen

The SENSE Director

Prof. Philipp Pattberg

The SENSE Research School has been accredited by the Royal Netherlands Academy of Arts and Sciences (KNAW)

KONINKLIJKE NEDERLANDSE
AKADEMIE VAN WETENSCHAPPEN

The SENSE Research School declares that **Qingdian Shu** has successfully fulfilled all requirements of the educational PhD programme of SENSE with a workload of 37.6 EC, including the following activities:

SENSE PhD Courses

- Environmental research in context (2018)
- Research in context activity: 'Organization of the 12th European Symposium on Electrochemical Engineering' (2021)

Other PhD and Advanced MSc Courses

- Bridging across cultural differences, Wageningen Graduate Schools (2018)
- Illustration for scientific publications, Wetsus/Somersault (2018)
- Bath Electrochemical Winter School, University of Bath (2019)
- Scientific Writing, Wageningen Graduate Schools (2020)
- ITB-IEAGHG International Virtual Course on Carbon Capture, Utilization and Storage (CCUS), ITB/IEAGHG (2021)

Management and Didactic Skills Training

- Supervising two MSc students with thesis and three MSc students with internship (2019 – 2022)
- Supervising one BSc student with internship (2021)

Oral Presentations

- *Electricity-driven Direct air capture (DAC) based on anion exchange resins*. Wetsus workshop on DAC and electrochemical conversion of CO_2, 22 April 2021, Leeuwarden, The Netherlands
- *Combined electrochemical desorption of CO_2 and recovery of alkaline sorbent for direct air capture*. 12th European Symposium on Electrochemical Engineering, 14 – 17 June 2021, Leeuwarden, The Netherlands
- *Electrochemical regeneration of spent alkaline absorbent from direct air capture*. 242nd ECS Meeting, 10 – 12 October 2022, Atlanta, USA

SENSE coordinator PhD education

Dr. ir. Peter Vermeulen

This work was performed in the cooperation framework of Wetsus, European Centre of Excellence for Sustainable Water Technology (www.wetsus.eu). Wetsus is co-funded by the Dutch Ministry of Economic Affairs and Climate Policy, the European Union Regional Development Fund, the City of Leeuwarden, the Province of Fryslân, the Northern Netherlands Provinces, and the Netherlands Organisation for Scientific Research. The author would finally like to thank the participants of the research theme "Sustainable Carbon Cycle" for their fruitful discussions and financial support.

Financial support from Wetsus and Environmental Technology Group (Wageningen University) for printing this thesis is gratefully acknowledged.

The cover is designed and drawn by Yujia Luo.